Modeling of Transport Phenomena in Two-Dimensional Semiconductors

A DISSERTATION
SUBMITTED TO THE FACULTY OF
UNIVERSITY OF MINNESOTA
BY

Yue Liu

IN PARTIAL FULFILLMENT OF THE REQUIREMENTS
FOR THE DEGREE OF
DOCTOR OF PHILOSOPHY

Dr. P. Paul Ruden, Advisor

December 2016

© Yue Liu 2016

Acknowledgements

In 2010, just one year before I entered graduate school, work on graphene was recognized by the award of the Nobel Prize in Physics. That somewhat predestinated that my entire Ph.D. career would be related to two-dimensional (2D) materials. Over the past fours years, I have been witnessing the development of several emerging 2D semiconductors in many applications and research fields. I am fascinated by their unique structure and properties, and always feel excited when I can simulate and understand the physics of 2D materials on a computer through numerical modeling, which makes up my wonderful journey at the University of Minnesota and finally leads to this dissertation.

Upon completing my Ph.D., I feel gratitude and fortunate for being able to work with a great advisor, Prof. P. Paul Ruden. He is not only very knowledgeable in the broad aspects of semiconductor physics, but also very flexible and patient in his research advising allowing me to touch on various topics and to try different directions. I benefit a lot from working in his group, and gain experience from spintronics to ionic liquid transistor, from numerical calculation to physical modeling. His attitude and personality, both inside and outside academia, has impressed and influenced me deeply.

I appreciate the opportunity to work with Dr. Darry L. Smith from Los Alamos National Laboratory. He offered many helpful insights and research experience on graphene spin transport. By the end of the school semesters, he always shared inspiring stories during our coffee time. I am thankful for the collaboration with Prof. Tony Low on black phosphorus. He is very generous to spend time on creative discussion with me and being my reference, despite being busy with his own research projects and proposals. I also would like to express special appreciation to Dr. Feilong Liu. As we both come from the same province in China, I learned quite a lot of useful and practical skills from him, such as debugging calculation scripts and manuscript submission. Moreover, I receive help from my labmates and colleagues in the ECE department: Dr. Brijesh Kumar, Dr. Chaitanya Kshirsagar, Dr. Yulong Li, Dr. Huan Li, Aditi Goswami, Jennifer Krohn, Tianbai Cui, Yang Su, Sha Shi, Nazila Haratipur and Jiaxi Hu.

In addition to research work, I would like to thank Prof. Stephen Campbell, Prof. Ted Higman and Prof. Steven Koester from the ECE department for their lectures first and

working with them as a teaching assistant later. Those experiences provide me a comprehensive understanding of semiconductor technology on levels of material fabrication, device design and circuit simulation. I would like to acknowledge Prof. Martin Greven, Prof. Yuichi Kubota and Prof. Alex Kamenev from the Physics department. During the first two years of graduate school study, the physics building is where I spend most of my time after Keller Hall. The training I received there gives me a solid background in condensed matter field, and brings up my general interests in other physics problems, too. I also want to express my appreciation to Seagate Technology at Shakopee MN, especially my manager Antoine Khoueir and my mentor Dr. Young Pil Kim, for the internship and industrial experience.

I would like to mention Dr. Ran Dai and Dr. Lin Niu, for their kind assistance during my first year in the United States. I deeply appreciate the University of Minnesota for everything that supports my journey pursuing the Ph.D., as well as to enable meeting my wife Yi Zhan here. I would like to thank Yi for her love and so many unforgettable moments we spend together. Finally, I want to thank my parents, I would not be here without their continuous support over both smooth and hard times.

Dedication

To my parents

Dejuan Zhang & Daming Liu

my wife

Yi Zhan

and my daughter

Norah Liu

Abstract

Two-dimensional (2D) materials have been attracting a lot of research interests from both academia and industry since graphene was isolated in 2004. Recently, transition metal dichalcogenides and black phosphorus (BP) emerged as new 2D semiconductors due to the advantages of moderate energy band gap, high carrier mobility, ultra thin film and high anisotropy. Together with graphene, 2D materials have been utilized in the development of biomedical devices, touch screen and display technologies, and flexible applications such as wearable electronics and IoT (Internet of Things) devices. They also open up new opportunities in research fields including spintronics, valleytronics, material anisotropy, optoelectronics and fabrication of high speed low power post silicon transistors for next generation scaling.

In this dissertation, we present theoretical modeling for several topics related to 2D materials. The physical based models aim at better understanding of electronic transport in 2D materials, as well as offering guidance for future novel device design applications. Starting with the fundamental tight-binding theory of graphene, we review special electronic properties for graphene including massless 2x2 Dirac Hamiltonian, pseudo-spin wave functions and quantum capacitance. Followed by a brief discussion of ballistic transport, we provide a detailed analysis on graphene diffusive transport. Ionized impurity scattering within back-gated device structure as well as carrier screening effect is considered in the model. As an isotropic material, the momentum relaxation time and mobility for graphene is modeled. Due to the rapidly varying of the density of states near the Dirac point, a non-linear Thomas Fermi screening is introduced later to improve the simulation accuracy.

Taking the real spin into account, the new graphene Hamiltonian is a 4x4 matrix. An externally applied electric field perpendicular to the graphene plane breaks the reflection symmetry and introduces a Rashba spin-orbit interaction, which couples pseudo-spin and real spin in graphene. The relevant charge carrier states are no longer spin eigenstates. Considering the nonlinear screening model, scattering cross-section for both ionized impurity scattering and Rashba spin scattering are calculated. Forward and back scattering patterns are different for the two mechanism depending on different selection

rules. Rashba interaction is found to be quite small compared to Coulomb impurity scattering, indicating other spin-orbit coupling mechanisms may have dominating contribution to the spin relaxation time in graphene. To characterize the spin-polarized electrons tunneling from electrodes and transport in graphene, a spin valve device modeling and magnetoresistance calculation is developed.

As an emerging 2D semiconductor beyond graphene, black phosphorus possesses excellent properties like other 2D van der Waals materials for high performance nanoelectronic and photonic applications. Moreover, there is a uniquely high in-plane anisotropy in black phosphorus due to its puckered crystal structure. To model the anisotropic momentum relaxation time and carrier mobility, a model based on the Boltzmann transport equation is developed, taking the full anisotropic electronic structure of black phosphorus into consideration. For zero temperature calculation with ionized impurity limited scattering, anisotropy ratio 3-4 can be obtained from the model. Though it is somewhat larger than experimental data, the results explain the mobility anisotropy ratio being much smaller than the effective mass ratio. The model is extended to finite temperature. Due to the dominating effect of screening, mobility is found to decrease weakly with increasing temperature. For $T < 100K$, a smaller anisotropy ratio of 1.8-3.5 matching experimental measurements indicates that impurity scattering is an important mechanism for black phosphorus. The models developed in this work can be applied to electron-phonon scattering as well as other emerging 2D anisotropic materials.

Table of Contents

Acknowledgements……………………..………………..……………………………i

Dedication…………………………………………………………………………iii

Abstract……………………………………………………………………………iv

Table of Contents……………………………………………………………………vi

List of Tables……………………………………………………………………viii

List of Figures……………………………………………………………………ix

Chapter 1 Introduction of Graphene and 2D Materials………………………………1

1.1 Overview…………………………………………………………………………1

1.2 Objective of the work and organization of the thesis…………………………5

Chapter 2 Graphene Electronic Transport Properties………………………………8

2.1 Graphene fundamentals………………………………………………………..8

2.2 Ballistic transport in graphene………………………………………………..19

2.3 Diffusive transport in graphene, a linear Thomas Fermi approach…………..22

2.4 Non-linear Thomas Fermi screening for graphene…………………………31

Chapter 3 Graphene Spintronics……………………………………………………..39

3.1 Introduction to spintronics……………………………………………………39

3.2 Rashba spin interaction in graphene…………………………………………42

3.3 Spin valve device, local model………………………………………………55

3.4 Spin valve device, nonlocal structure and magnetoresistance………………62

Chapter 4 Modeling of Anisotropic Transport in Black Phosphorus ………………71

4.1 Introduction of 2D materials beyond graphene………………………………71

4.2 Method and approach to evaluate 2D anisotropic Boltzmann transport………73

4.3 Zero temperature relaxation time and mobility calculation……………………..78

4.4 Finite temperature relaxation time and mobility calculation ………………86

Chapter 5 Summary and Suggestions for Future Work…………………………103

5.1 Summary………………………………………………………………103

5.2 Suggestions for future work……………………………………………105

Bibliography…………………………………………………………………107

Appendix……………………………………………………………………116

A Isotropic and anisotropic relaxation time derivation ………………………116

B Potential and Rashba scattering cross-sections ……………………………117

C Consideration of the optical theorem …..……………………………………..121

List of Tables

Table 3.1 Power consumption for electronic and spintronic switch 40

Table C.1 $Im[f(0)]/f_B(0)$ for intra-band potential scattering 121

Table C.2 $Im[f(0)]/f_B(0)$ for intra-band Rashba scattering 121

List of Figures

Fig. 1.1	Graphene applications: display, thin film and flexible transistor	2
Fig. 1.2	2D ultra thin body devices from Berkeley	4
Fig. 1.3	Devices utilizing black phosphorus anisotropic properties	5
Fig. 2.1	Graphene lattice structure	8
Fig. 2.2	Occupation states of electrons and spin in carbon	9
Fig. 2.3	Energy dispersion from tight binding and *ab initio* calculation	11
Fig. 2.4	Diagram of graphene energy dispersion near Dirac point	13
Fig. 2.5	Typical back-gated graphene structure	15
Fig. 2.6	Quantum capacitance in graphene	18
Fig. 2.7	Graphene ballistic transport	20
Fig. 2.8	Graphene universal conductivity	21
Fig. 2.9	Schematic of back-gated graphene with out-of-plane impurity	23
Fig. 2.10	Schematic of transfer vector $\vec{q} = \vec{k}' - \vec{k}$	26
Fig. 2.11	Potential energy in Fourier space as a function of k and θ	30
Fig. 2.12	Momentum relaxation time as a function of E for different z_0	31
Fig. 2.13	Electron-hole puddle effect near Dirac point	32
Fig. 2.14	Potential energy using non-linear Thomas Fermi screening	36
Fig. 2.15	Potential energy using linear Thomas Fermi screening	37
Fig. 3.1	Schematic of all spin logic (ASL) device	40
Fig. 3.2	Spin-transfer torque random-access memory (STT-RAM) cell	41
Fig. 3.3	Energy gap closes/opens without/with intrinsic spin-orbit coupling	43
Fig. 3.4	Perpendicular electric field caused by electron sheet in graphene	44
Fig. 3.5	Intrinsic and Rashba spin-orbit coupling for different electric field	45
Fig. 3.6	Band splits (spin degeneracies are lifted) due to Rashba effect	46
Fig. 3.7	Scattering process for intra-band scattering and inter-band scattering	47
Fig. 3.8	Different scattering cross-section for ionized impurity scattering	49
Fig. 3.9	Total scattering cross-section for ionized impurity scattering	51
Fig. 3.10	Different scattering cross-section for Rashba spin scattering	53
Fig. 3.11	Several different spin relaxation mechanisms in graphene	54

Fig. 3.12 Schematic of graphene spin valve device 56

Fig. 3.13 ES potential and current density profile for local configuration 61

Fig. 3.14 EC potential for P and AP configuration 64

Fig. 3.15 V_{43}, ΔE_F and spin current as a function of gate bias 65

Fig. 3.16 Current density and MR for local/ nonlocal structure with small V_{DS} 66

Fig. 3.17 ΔE_F and MR for nonlocal structure with large gate bias 67

Fig. 3.18 Current density and MR for local/ nonlocal structure with large V_{DS} 68

Fig. 3.19 V_{GS} and V_{DS} dependent MR for different spin relaxation time 69

Fig. 3.20 V_{DS}^{OC} and nonlocal resistance R_{NL} as a function of V_{GS} and current 70

Fig. 4.1 Wave spectrum, band gaps, mobility and on/off ratios of 2D materials 72

Fig. 4.2 BP model schematic structure 75

Fig. 4.3 Relaxation time for electric field along x and y directions 80

Fig. 4.4 Relaxation time as a function of incoming angle and carrier density 81

Fig. 4.5 Mobility and anisotropy ratio as a function of carrier density 84

Fig. 4.6 Schematic for finite temperature scattering 88

Fig. 4.7 Finite temperature effect on E_F and $f(E) \cdot [1 - f(E)]$ distribution 89

Fig. 4.8 $\Pi(q_x, T)$ and $\Pi(q_y, T)$ for different temperature 91

Fig. 4.9 Effective screening q_s as a function of q_x and q_y 92

Fig. 4.10 Momentum relaxation time for T, n and electric field direction 94

Fig. 4.11 Angle averaged $\bar{\tau}_m$ for different parameters 95

Fig. 4.12 Mobility μ_{xx} and μ_{yy} as a function of T for different n 98

Fig. 4.13 Anisotropy ratio $\frac{\mu_{xx}}{\mu_{yy}}$ decrease as temperature increases 101

Chapter 1 Introduction of Graphene and 2D Materials

1.1 Overview

Semiconductor research on two-dimensional materials (more exactly, two-dimensional electron gas, or 2DEG) can be traced back to 70'-80', when the silicon inversion layer in MOSFET began to be treated as a 2DEG for accurate modeling.[1][2][3] However, pure and freestanding 2D materials are considered non-existing due to thermal instability until monolayer graphene was first isolated in 2004 by Novoselov and Geim at the University of Manchester using mechanical exfoliation.[4][5][6][7][8] The importance of this achievement was recognized by the 2010 Noble Prize in physics. Ever since 2004, there has been extensive research work related to graphene, and more recently other emerging 2D materials.

The applications of 2D materials can be found in almost every nanotechnology field. For example, graphene exhibits great electronic and optical properties as well as good adhesion to organic materials for organic light-emitting diodes (OLEDs) and display applications as shown in Fig. 1.1 (a). Graphene also exhibits excellent mechanical characteristic including near transparency, high stretchability, and it is remarkably strong for its low weight, making it a promising candidate for flexible electronic applications as shown in Fig. 1.1 (b).[9][10] After 2010, wearable electronics, biomedical devices and Internet of Things (IoT) develops fast, 2D materials make contributions to that quick growth. The special Dirac electronic structure in graphene enables massless high speed carrier, ballistic transport and fast switching transistors. Fig. 1.1 (c) demonstrates graphene field-effect transistor (FET) fabricated on a flexible plastic PET substrate, featuring high-mobility $300 cm^2 V^{-1} s^{-1}$ and low-voltage below $3V$.[11]

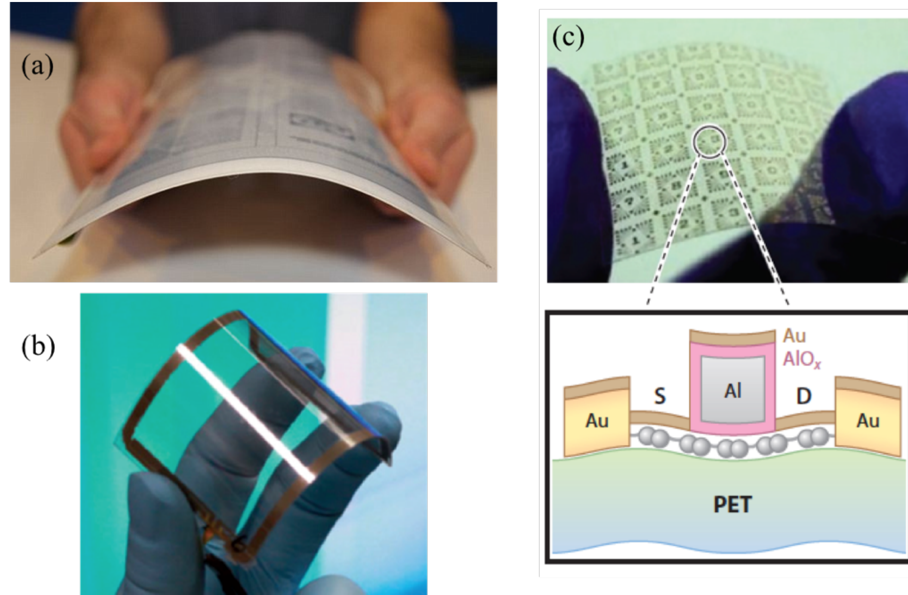

Fig. 1.1. (a) Flexible graphene display developed by Plastic Logic and Cambridge Graphene Centre.[12] (b) High quality graphene transparent conductive film.[9] (c) Array of self-aligned graphene FET on polyethylene terephthalate (PET).[11]

While the unique electronic structure makes graphene a promising candidate for many novel material applications, spin transport in graphene is also a growing topic for development of spintronic devices.[13][14][15] Intrinsic spin-orbit interaction is a weak effect in graphene, lead to long spin life time and spin diffusion length,[16][17] which is not limited by charged impurity scattering[18] and has been demonstrated by long distance spin communication in CVD graphene[19].

Graphene is one example of van der Waals solids, whose crystal structure features neutral, single-atom thick layer of atoms with covalent or ionic bonding along two dimensions and Van der Waals bonding along the third. Other emerging van der Waals materials includes Transition Metal Dichalcogenides[20][21][22] (TMD, stoichiometry MX_2, with M=Mo, W, Nb, Ti and X=S, Se, Te) and Black Phosphorus[23][24][25] (BP). In TMD community, due to the similar structure to graphene, there is much intensive research on the widening band gap with decreasing number of layers due to quantum confinement effect, indicating transition to direct band gap in monolayer crystal[26], as well as extra valley degree of freedom and valley Hall effect[27][28]. In addition to the flexible applications analogous to graphene discussed above, two-dimensional TMD and BP have

moderate intrinsic energy gaps, making them ideal ultra thin channel materials for high performance sub-10nm scaled transistors.[29][30] The ultra thin body (UTB) devices, initially proposed by the Berkeley Device Group, offer new scaling paths to further shrink transistors.[31] Rather than reducing the oxide thickness to improve the gate control, UTB devices apply thin substrate to cut leakage path and overcome the short channel effects (threshold voltage roll-off, DIBL, subthreshold leakage, GIDL). Two technologies of UTB devices, FinFET and FD-SOI (fully depleted silicon on insulator), have already been adopted by leading semiconductor fabs Intel, Samsung, Global Foundries and TSMC in their 14nm technology nodes since 2012-2013.[32][33] UTB devices are the biggest breakthrough of transistor technology after strained silicon (90 nm node) and high-*k* metal gate (45nm node).

To further scale the transistor size and to continue Moore's law, the ultimate ideal thin body would be 2D monolayer semiconductors. Si or Ge surfaces have many broken/dangling bonds, while 2D materials provide perfect surfaces by nature. Moreover, 2D semiconductors can be CVD grown on dielectric/substrate through self-assembly rather than epitaxy, which may possibly reduce manufacturing cost. For instances, a MoS_2 on insulator device in Fig. 1.2 (a)[29] and FinFET with MoS_2 channel materials in Fig. 1.2 (b)[34] have been reported in recent years. While writing this thesis in October 2016, a 1nm gate length MoS_2 transistor using CNT as gate electrode has been published in *Science*.[35]

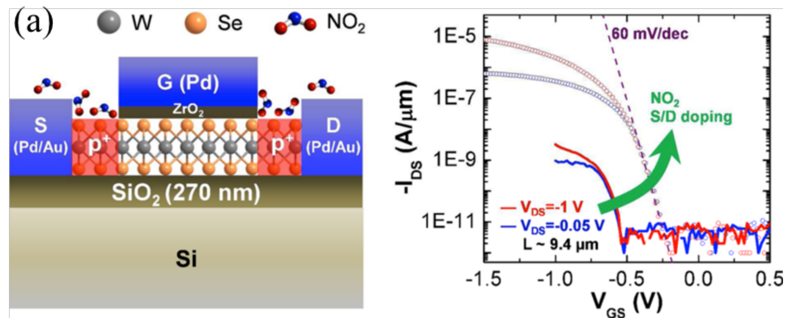

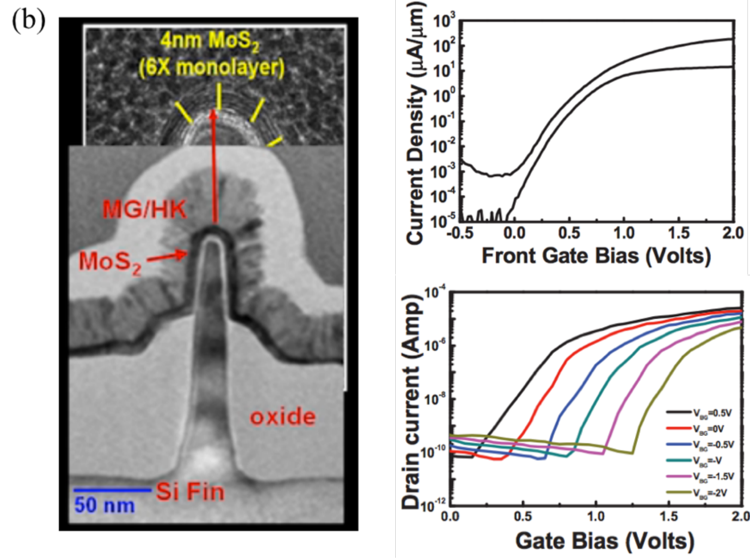

Fig. 1.2. (a) 2D Materials on Insulator structure P-FET with WSe_2 channel material, high mobility $\sim 250 cm^2 V^{-1} s^{-1}$, 60mV/dec SS, $I_{ON}/I_{OFF} > 10^6$.[29] (b) Few layers MoS_2 FinFET with fin-shaped back-gate control $I_{ON} \sim 0.2 mA/\mu m$, V_{th} adjustable for high performance/ low power applications.[34]

Around 2014, another 2D semiconductor, layered black phosphorus emerged as a promising 2D semiconductor for high performance nanoelectronic and infrared optoelectronics applications.[23][24][25][36] In addition to the 2D structure, high mobility and ON/OFF ratio bridging graphene and TMD, the most important and novel applications of BP may arise from its unique properties, the high in-plane anisotropy.[25][37] For example (1) plasmonic devices with intrinsic anisotropy in their resonance properties[38] in Fig. 1.3 (a), (2) high-efficiency thermoelectrics using the orthogonality in the heat and electron transport directions[39][40] in Fig. 1.3 (b), (3) auxetic material with negative Poisson's ratio demonstrated using BP.[41][42] The strongly anisotropic properties of BP and other 2D materials can be employed to design innovative devices and open new application opportunities.

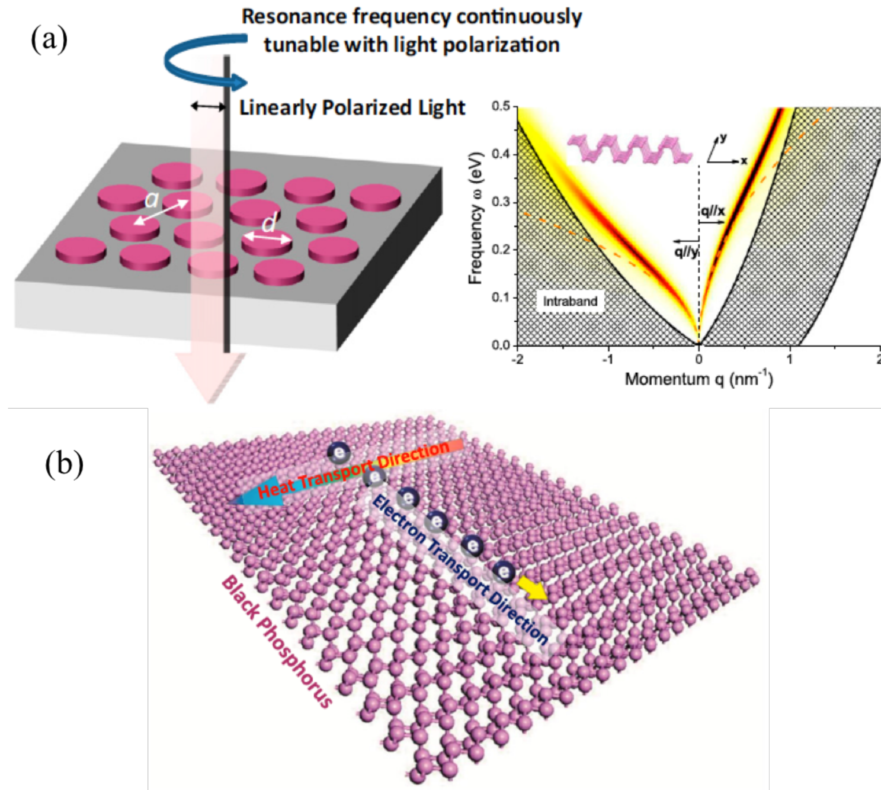

Fig. 1.3. (a) Schematics of BP plasmonic devices with intrinsic anisotropy in their resonance frequency. The calculated plasmonic dispersions along both the x and y directions are shown on right.[38] (b) Schematics showing the orthogonality between the dominant heat and electron transport directions in monolayer BP.[39]

1.2 Objective of the work and organization of the thesis

This thesis contributes to several theoretical modeling efforts related to 2D semiconductor materials. Using these physically based models, researchers in the community could have a better understanding on several aspects, ranging from graphene transport, Thomas Fermi screening, Rashba spin interaction, graphene spin valve models and anisotropic transport in black phosphorus. Following the approaches in this thesis, various key electronic parameters can be calculated, which provides physical insight and

explanation of 2D materials transport properties, as well as potentially gives helpful prediction for future device design.

In Chapter 2, transport properties due to the special Dirac structure in graphene are discussed. Though much work has been done in modeling of graphene electronics, we start from tight binding theory and show the origin of massless 2x2 Dirac Hamiltonian and pseudo-spin wave functions. Energy dispersion, carrier density and quantum capacitance can be found as a result of the special monolayer graphene. These discussions also serve as fundamental for more complicated topics in later parts of the thesis. Linear and nonlinear Thomas Fermi screening for ionized impurity scattering are discussed within graphene diffusive transport. Isotropic relaxation time can be derived either directly from Boltzmann transport equation or differential scattering cross-section. Potential energy limited by ionized impurity scattering in real and Fourier space are compared for different screening models.

Chapter 3 deals with spin interaction in graphene. Introducing the real spin, the Dirac Hamiltonian becomes a 4x4 matrix. Intrinsic spin-orbit coupling is a week effect and thus we focus on extrinsic Rashba spin-orbit coupling. Since Rashba interaction is caused by external perpendicular electric field, the space symmetry is broken and spin degeneracy is lifted. Charge carrier states are not spin-eigenstates in graphene. Using the nonlinear Thomas Fermi screening, ionized impurity scattering and Rashba spin scattering are calculated and compared for intra/inter-band scattering processes. While back scattering is generally considered as forbidden for ionized impurity scattering in graphene, it is allowed for Rashba spin scattering. Later sessions in Chpater 3 focus on on spin injection into graphene, spin valve device modeling and magnetoresistance (MR). Spin-polarized electrons are injected from electrode, transported across the graphene, and detected by the another electrode. The difference in the resistance between the parallel and antiparallel magnetization alignments are calculated as MR from spin transport.

In Chapter 4, we focus on the novel anisotropic 2D semiconductor black phosphorus. Starting with zero temperature calculation, a transport equation in relaxation time approximation is developed, fully taking account of the BP anisotropic structure. For feasible carrier density in experiments and considering ionized impurity scattering, a

mobility anisotropy ratio 3~4 is obtained, which is quite small compared to the effective mass ratio, but larger than measured data obtained at finite temperature. For the finite temperature calculation of BP anisotropic transport, several variables such as Fermi level, energy regions and screening effect now become temperature dependent and thus make the calculation more complicated. As a results of screening effect dominating, mobility slowly decreases as temperature increases. The weak mobility dependence on temperature as well as the smaller mobility anisotropy ratio, 1.8-3.5, matching accurately with experimental results, indicate ionized impurity scattering and screening effect could be a more significant mechanism than electron-phonon scattering in black phosphorus. The difference between isotropic and anisotropic transport phenomena can be understood by comparing Chapter 2 and Chapter 4.

We summarize the thesis in Chapter 5 and provide several directions for future work. Bibliography and Appendices are listed subsequently after Chapter 5.

Chapter 2 Graphene Electronic Transport Properties

2.1 Graphene fundamentals

The basic lattice structure for graphene is plotted in Fig. 2.1 for both real and reciprocal space. Lattice vectors $\vec{a}_1 = \left(\frac{\sqrt{3}}{2}, \frac{1}{2}\right) a$ and $\vec{a}_2 = \left(\frac{\sqrt{3}}{2}, -\frac{1}{2}\right) a$, with lattice constant $a = |\vec{a}_1| = |\vec{a}_2| = \sqrt{3}l \approx 2.46A$. l is the nearest-neighbor atom distance. Three nearest-neighbor vectors $\vec{\delta}_1 = \left(\frac{1}{2}, \frac{\sqrt{3}}{2}\right) l$, $\vec{\delta}_2 = \left(\frac{1}{2}, -\frac{\sqrt{3}}{2}\right) l$ and $\vec{\delta}_1 = (-1,0)l$. Reciprocal space vectors $\vec{b}_1 = \frac{2\pi}{a}\left(\frac{1}{\sqrt{3}}, 1\right)$, $\vec{b}_2 = \frac{2\pi}{a}\left(\frac{1}{\sqrt{3}}, -1\right)$. A and B are two basis atoms on inequivalent sites in one primitive unit cell. At Brillouin zone corners are K and K' points, where electronic energy of graphene reaches minimum. $K = \frac{2\pi}{a}\left(\frac{1}{\sqrt{3}}, \frac{1}{3}\right)$ and $K' = \frac{2\pi}{a}\left(\frac{1}{\sqrt{3}}, -\frac{1}{3}\right)$ are also called Dirac points.[43][44]

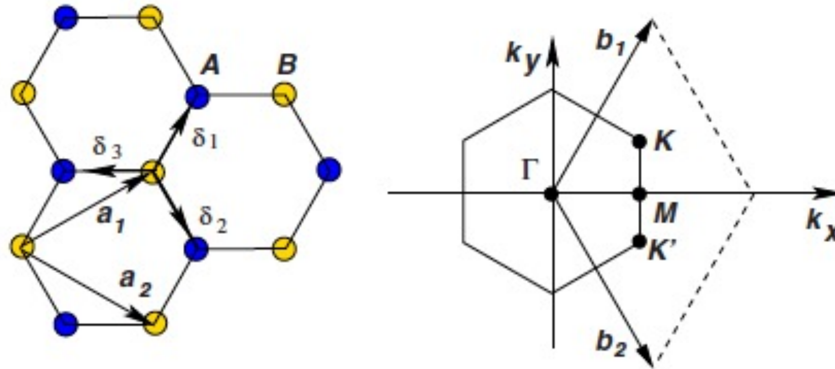

Fig. 2.1. Lattice structure of graphene in real space (left) and reciprocal space (right).[7]

In general, as a Group IV element, carbon has 4 valence electrons and forms various types of allotropes. For elemental carbon, the valence electrons occupy $2s$ and $2p$ orbitals (Fig. 2.2 (a)). When carbon crystal structures are formed, $2s$ electrons are excited to $2p_z$

orbitals in order to lower the overall system energy. The carbon allotrope exists in various dimensions: C_{60} (0D), carbon nanotubes (1D), graphene (2D), graphite and diamond (3D).

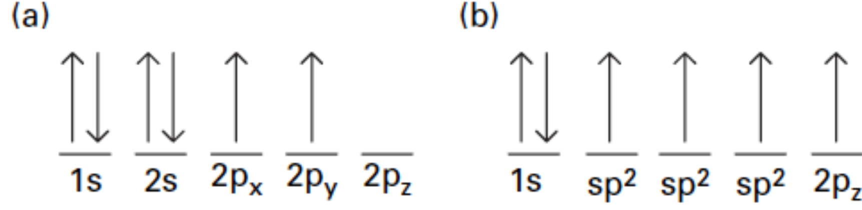

Fig. 2.2. Occupation states of electrons and spin.[45] (a) Elemental carbon. (b) Graphene. $2s$ and $2p$ electrons interact covalently to form sp^2 hybridation.

Graphene has a planar structure such that all carbon atoms are confined to a monolayer plane by covalent bonds. Carbon atoms in graphene form sp^2 hybridization: one $2p_z$ orbital and three hybridized $2sp^2$ orbitals, for the total four valence electrons (Fig. 2.2 (b)). As a result, one π-bond (due to $2p_z$) and three σ-bonds (due to $2sp^2$) are produced. We are interested in the energy dispersion due to the π-bond since the $2p_z$ electrons are weakly bound to the nuclei and are relatively delocalized.[46] There are 2 basis atomic orbitals in a primitive unit cell, φ_A and φ_B, each corresponds to one $2p_z$ orbital.

From tight binding or LCAO (linear combination of atomic orbitals) theory, We can write two Bloch functions $|\phi_A\rangle$ and $|\phi_B\rangle$ as a linear combination of atomic orbital wave functions.

$$|\phi_A\rangle = \frac{1}{\sqrt{N}}\sum_{\vec{R}} e^{i\vec{k}\cdot\vec{R}}\varphi_A(\vec{r}-\vec{R}) \qquad (2.1a)$$

$$|\phi_B\rangle = \frac{1}{\sqrt{N}}\sum_{\vec{R}} e^{i\vec{k}\cdot\vec{R}}\varphi_B(\vec{r}-\vec{R}) \qquad (2.1b)$$

where $\vec{k}$ is wave vector in reciprocal space and $\vec{R}$ is Bravais lattice vector. The tight binding Hamiltonian $\langle\phi_A|H|\phi_A\rangle$ and $\langle\phi_A|H|\phi_B\rangle$ can be calculated as follows, H stands for the interacting mechanism or energy transfer integral.

$$\langle\phi_A|H|\phi_A\rangle = \frac{1}{N}\left[\sum_{\vec{R}\prime=\vec{R}}\langle\varphi_A(\vec{r}-\vec{R}')|H|\varphi_A(\vec{r}-\vec{R})\rangle\right.$$

$$+\sum_{\vec{R}'=\vec{R}+\vec{a}_1} e^{-i\vec{k}\cdot\vec{a}_1}\left\langle\varphi_A(\vec{r}-\vec{R}')\middle|H\middle|\varphi_A(\vec{r}-\vec{R})\right\rangle$$

$$+\sum_{\vec{R}'=\vec{R}+\vec{a}_2} e^{-i\vec{k}\cdot\vec{a}_2}\left\langle\varphi_A(\vec{r}-\vec{R}')\middle|H\middle|\varphi_A(\vec{r}-\vec{R})\right\rangle+\cdots\Bigg] \quad (2.2)$$

Let $\left\langle\varphi_A(\vec{r}-\vec{R}')\middle|H\middle|\varphi_A(\vec{r}-\vec{R})\right\rangle = E_{2p}$, we arrive with $\langle\phi_A|H|\phi_A\rangle = \frac{1}{N}\sum_{\vec{R}'=\vec{R}} E_{2p} = E_{2p}$ in the nearest neighbor approximation. Similarly, for $\langle\phi_A|H|\phi_B\rangle$,

$$\langle\phi_A|H|\phi_B\rangle = \frac{1}{N}\Bigg[\sum_{\vec{R}'=\vec{R}+\vec{\delta}_1} e^{-i\vec{k}\cdot\vec{\delta}_2}\left\langle\varphi_A(\vec{r}-\vec{R}')\middle|H\middle|\varphi_B(\vec{r}-\vec{R})\right\rangle$$

$$+\sum_{\vec{R}'=\vec{R}+\vec{\delta}_2} e^{-i\vec{k}\cdot\vec{\delta}_2}\left\langle\varphi_A(\vec{r}-\vec{R}')\middle|H\middle|\varphi_B(\vec{r}-\vec{R})\right\rangle$$

$$+\sum_{\vec{R}'=\vec{R}+\vec{\delta}_3} e^{-i\vec{k}\cdot\vec{\delta}_3}\left\langle\varphi_A(\vec{r}-\vec{R}')\middle|H\middle|\varphi_B(\vec{r}-\vec{R})\right\rangle+\cdots\Bigg] \quad (2.3)$$

Let $\left\langle\varphi_A(\vec{r}-\vec{R}')\middle|H\middle|\varphi_B(\vec{r}-\vec{R})\right\rangle = t$, then $\langle\phi_A|H|\phi_B\rangle = t\left(e^{-i\vec{k}\cdot\vec{\delta}_1}+e^{-i\vec{k}\cdot\vec{\delta}_2}+e^{-i\vec{k}\cdot\vec{\delta}_3}\right)$. $t \approx 2.8eV$ has many names such as nearest neighbor overlapping energy, hopping energy or carbon-carbon interaction energy.[43] Define the hopping function $f(\vec{k}) = e^{-i\vec{k}\cdot\vec{\delta}_1} + e^{-i\vec{k}\cdot\vec{\delta}_2} + e^{-i\vec{k}\cdot\vec{\delta}_3}$. It can be also written as $f(\vec{k}) = \left[e^{\frac{ik_xa}{\sqrt{3}}} + 2e^{-\frac{ik_xa}{\sqrt{3}}}cos\frac{k_ya}{2}\right]e^{-\frac{ik_xa}{\sqrt{3}}}$. The modulus $\left|f(\vec{k})\right| = \sqrt{1+4cos\frac{\sqrt{3}k_xa}{2}cos\frac{k_ya}{2}+4cos^2\frac{k_ya}{2}}$ can be derived. [7]

The tight binding Hamiltonian for graphene can be thus written as

$$H = \begin{bmatrix} E_{2p} & tf(\vec{k}) \\ tf(\vec{k})^* & E_{2p} \end{bmatrix} \quad (2.4)$$

As a result, the energy dispersion can be presented in Eq. 2.5 and Fig. 2.3

$$E = E_{2p} \pm t\left|f(\vec{k})\right| = E_{2p} \pm t\sqrt{1+4cos\frac{\sqrt{3}k_xa}{2}cos\frac{k_ya}{2}+4cos^2\frac{k_ya}{2}} \quad (2.5)$$

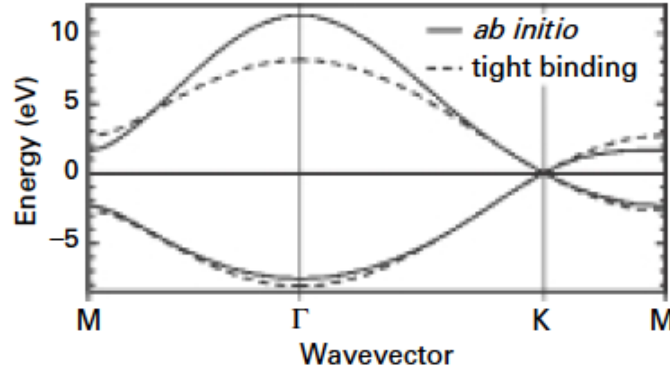

Fig. 2.3. The graphene energy dispersion from tight binding method with nearest neighbor approximation agrees well with the *ab initio* calculation, especially near K point.[45]

To make further simplification, considering $f(\vec{k})$ in the vicinity of K point, we can write $\vec{k} = \vec{K} + \vec{q}$ ($\vec{K}$ is the wave vector between Γ and K, $\vec{q}$ is small) and $f(\vec{q})$ near Dirac points can be expressed as

$$f(\vec{k}) = f(\vec{K}) + \vec{q} \cdot \nabla_{\vec{k}} f\big|_{\vec{K}} \tag{2.6}$$

$f(\vec{K})$ can be found by calculating

$$\vec{K} \cdot \vec{\delta}_1 = \frac{2\pi}{a}\left(\frac{1}{\sqrt{3}}, \frac{1}{3}\right) \cdot \left(\frac{1}{2}, \frac{\sqrt{3}}{2}\right) \frac{a}{\sqrt{3}} = \frac{2\pi}{3} \tag{2.7a}$$

$$\vec{K} \cdot \vec{\delta}_2 = \frac{2\pi}{a}\left(\frac{1}{\sqrt{3}}, \frac{1}{3}\right) \cdot \left(\frac{1}{2}, -\frac{\sqrt{3}}{2}\right) \frac{a}{\sqrt{3}} = 0 \tag{2.7b}$$

$$\vec{K} \cdot \vec{\delta}_3 = \frac{2\pi}{a}\left(\frac{1}{\sqrt{3}}, \frac{1}{3}\right) \cdot (-1,0) \frac{a}{\sqrt{3}} = -\frac{2\pi}{3} \tag{2.7c}$$

Subsequently,

$$f(\vec{K}) = e^{-i\vec{K}\cdot\vec{\delta}_1} + e^{-i\vec{K}\cdot\vec{\delta}_2} + e^{-i\vec{K}\cdot\vec{\delta}_3} = \left(-\frac{1}{2} - \frac{\sqrt{3}}{2}i\right) + 1 + \left(-\frac{1}{2} + \frac{\sqrt{3}}{2}i\right) = 0 \tag{2.8}$$

Then the simplified $f(\vec{k})$ becomes a function of $\vec{q}$, i.e. (q_x, q_y) using Eq. 2.6

$$f(\vec{k}) = \vec{q} \cdot \nabla_{\vec{k}} f\big|_{\vec{K}} = \vec{q} \cdot \left(-\vec{\delta}_1 e^{-i\vec{K}\cdot\vec{\delta}_1} - \vec{\delta}_2 e^{-i\vec{K}\cdot\vec{\delta}_2} - \vec{\delta}_3 e^{-i\vec{K}\cdot\vec{\delta}_3}\right)$$

$$= (q_x,\ q_y)\left[l \begin{pmatrix} -\frac{1}{2} \\ -\frac{\sqrt{3}}{2} \end{pmatrix} \left(-\frac{1}{2} - \frac{\sqrt{3}}{2}i\right) + l \begin{pmatrix} -\frac{1}{2} \\ \frac{\sqrt{3}}{2} \end{pmatrix} + l \begin{pmatrix} 1 \\ 0 \end{pmatrix} \left(-\frac{1}{2} + \frac{\sqrt{3}}{2}i\right) \right]$$

$$= \frac{3l}{2}(q_x - iq_y)e^{i\theta} \tag{2.9}$$

Plugging Eq. 2.9 into Eq. 2.4, the Hamiltonian in the vicinity of K can be expressed as

$$H = \begin{bmatrix} E_{2p} & \frac{3tl}{2}(q_x - iq_y)e^{i\theta} \\ \frac{3tl}{2}(q_x + iq_y)e^{-i\theta} & E_{2p} \end{bmatrix} \tag{2.10}$$

Since graphene hopping energy t and nearest-neighbor distance l are known, one can define a fitting parameter $v_F = \frac{3tl}{2\hbar} \approx 10^8 cms^{-1}$ and apply a unitary transformation $U^\dagger HU$ with $U = \begin{bmatrix} 0 & e^{-i\frac{\theta}{2}} \\ e^{i\frac{\theta}{2}} & 0 \end{bmatrix}$. The new Hamiltonian can be simplified as

$$H = \begin{bmatrix} E_{2p} & \hbar v_F(q_x - iq_y) \\ \hbar v_F(q_x + iq_y) & E_{2p} \end{bmatrix} \tag{2.11}$$

From now on, our discussion is focused on the low energy near K point, therefore we set the origin at K instead of Γ, for convenience. The notation (q_x, q_y) then come back to (k_x, k_y)

$$H = \begin{bmatrix} E_{2p} & \hbar v_F(k_x - ik_y) \\ \hbar v_F(k_x + ik_y) & E_{2p} \end{bmatrix} \tag{2.12}$$

Finally, setting $E_{2p} = 0$ and introducing the Pauli spin matrix $\sigma_x = \begin{bmatrix} 0 & 1 \\ 1 & 0 \end{bmatrix}$, $\sigma_y = \begin{bmatrix} 0 & -i \\ i & 0 \end{bmatrix}$, $\sigma_z = \begin{bmatrix} 1 & 0 \\ 0 & 1 \end{bmatrix}$,

$$H = \begin{bmatrix} 0 & \hbar v_F(k_x - ik_y) \\ \hbar v_F(k_x + ik_y) & 0 \end{bmatrix} = \hbar v_F(\sigma_x k_x + \sigma_y k_y) \tag{2.13a}$$

$$H = \hbar v_F \vec{\sigma} \cdot \vec{k} = -i\hbar v_F \vec{\sigma} \cdot \nabla \tag{2.13b}$$

Hamiltonian in Eq. 2.13 shares the same form as that for a massless Dirac fermion. The fitting parameter v_F has the physical meaning of Fermi velocity, corresponding to the speed of light c in the Dirac equation. Diagonalizing the 2x2 Hamiltonian, we can find two eigenvalues

$$E_\pm(k) = \pm\hbar v_F k \tag{2.14}$$

with $k = |\vec{k}| = \sqrt{{k_x}^2 + {k_y}^2}$, i.e. the energy dispersion in graphene has a linear dependence on $|\vec{k}|$, as shown in Fig. 2.4(a). Following the conventional terminology in semiconductor physics, E_+ and E_- are called conduction and valence band (Fig. 2.4(b)), respectively.

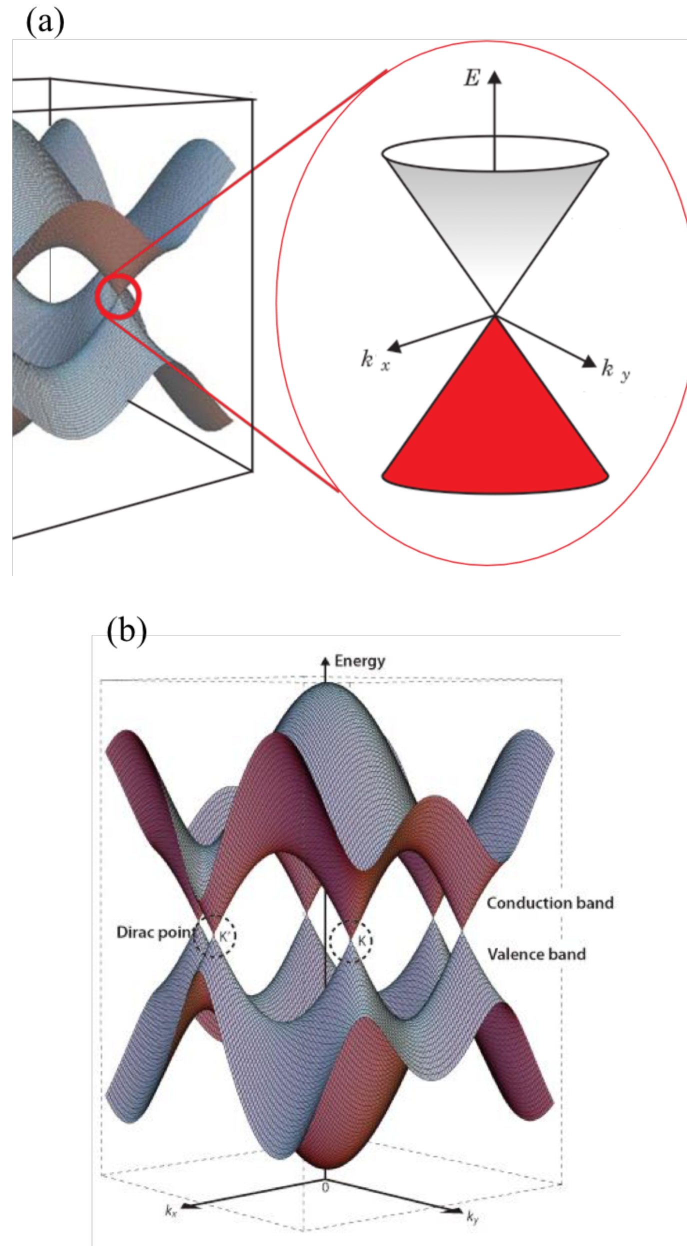

Fig. 2.4. Graphene energy dispersion near Dirac point. (a) Linear dependence on wave vector.[43] (b) Conduction band and valence band.[47]

For the K' valley, following similar steps, we can find the 2x2 Hamiltonian $H = \hbar v_F(\sigma_x k_x - \sigma_y k_y)$. Two normalized eigenstates corresponding to $E_\pm(k)$ can be written as

$$\Phi_+(\vec{k}) = \frac{1}{\sqrt{2}}\begin{pmatrix} e^{-i\frac{\theta_{\vec{k}}}{2}} \\ e^{i\frac{\theta_{\vec{k}}}{2}} \end{pmatrix} e^{i\vec{k}\cdot\vec{r}}, \quad \Phi_-(\vec{k}) = \frac{1}{\sqrt{2}}\begin{pmatrix} e^{-i\frac{\theta_{\vec{k}}}{2}} \\ -e^{i\frac{\theta_{\vec{k}}}{2}} \end{pmatrix} e^{i\vec{k}\cdot\vec{r}} \tag{2.15}$$

with $\theta_{\vec{k}} = tan^{-1}\frac{k_y}{k_x}$. Φ_+ and Φ_- are called the "pseudo-spin" wave function because they are solved in the spin format from massless Dirac equation. Please note that the "real spin" has not been introduced yet. The origin of such massless Dirac Hamiltonian and pseudo-spin degree of freedom in graphene is due to the presence of A and B sublattices. The Hamiltonian considering real spin is discussed in Chapter 3.

With the energy dispersion given in Eq. 2.14, the density of states (DOS) is given by

$$g(E) = \frac{g_s g_v}{(2\pi)^2}\int d^2k\,\delta(E - \hbar v_F k) = \frac{2}{\pi}\int_0^\infty dk\,k\;\delta(E - \hbar v_F k) = \frac{2}{\pi(\hbar v_F)^2}E \tag{2.16}$$

$g_s = g_v = 2$ stands for spin and valley degeneracy. The DOS depends linearly on energy E. We define $a = \frac{2}{\pi(\hbar v_F)^2} \approx 1.469\times10^{14} cm^{-2}eV^{-2}$. $g(E)$ vanishes at $E = 0$ i.e. the Dirac point. We will revisit this part as we discuss the screened potential in Section 2.4. The DOS linear dependence on energy distinguishes graphene from other conventional 2D materials or 2DEG with parabolic band, whose DOS is a constant. The graphene Fermi wave vector can be expressed as[7]

$$k_F = \sqrt{\frac{4\pi n}{g_s g_v}} = \sqrt{\pi n} \tag{2.17}$$

which is also different from 2DEG, where $k_F = \sqrt{2\pi n}$. n is electron density. With DOS known in Eq. 2.16, the electron density in graphene can be calculated with

$$n = \int dE\; g(E)f(E) \tag{2.18}$$

$f(E)$ is the Fermi-Dirac distribution, which is a step function at zero temperature, i.e. $u(E_F - E)$

$$n = \int dE(aE)u(E_F - E) = \int_0^{E_F} aEdE = \frac{1}{2}aE_F{}^2 \tag{2.19}$$

For finite temperature $f(E) = \frac{1}{1+exp\left(\frac{E-E_F}{k_BT}\right)}$, the electron density can then be written as

$$n = a\int_0^{\infty} dE \frac{E}{1 + exp\left(\frac{E - E_F}{k_BT}\right)} \tag{2.20}$$

If E_F is much greater than the thermal energy k_BT, we have following approximation

$$n \approx a\left[\frac{1}{2}E_F{}^2 + \frac{1}{6}(\pi k_BT)^2\right] \tag{2.21}$$

which will be used in Chapter 3. Similarly, for the hole density

$$p = \int_{-\infty}^{0} dE\, g(E)[1 - f(E)] = a\int_0^{\infty} dE \frac{E}{1 + exp\left(\frac{E + E_F}{k_BT}\right)} \tag{2.22}$$

Once we know how to calculate the carrier density in graphene, we can explore many marvelous electronic properties in graphene due to its unique Dirac cone band structure. We introduce the quantum capacitance as an example here since it is relevant to topics in this dissertation work. Many other unique properties in graphene, such as Klein tunneling[48][49][50][51][52][53][54], electron-hole puddles[55][56][57][58] and room temperature QHE (Quantum Hall Effect)[59][60][61][62][63][64] can be found in the literature and have been well reviewed.[7][43][65][66][67]

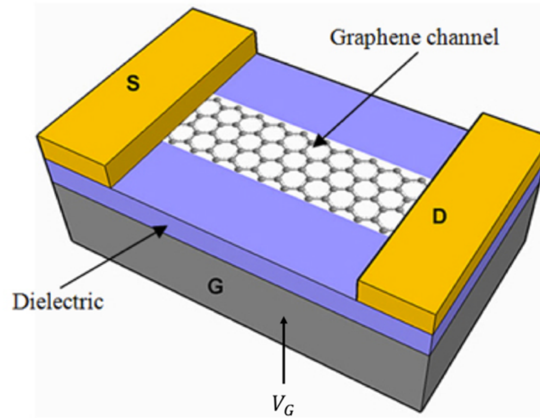

Fig. 2.5. Graphene in back-gated FET structure.[68] (Strictly speaking, this is not a transistor since graphene is a semimetal without band gap, i.e. the device can not be turned off. However, this is structure is very useful in discussion of graphene as well as other layered 2D materials)

The graphene sample in back-gated structure Fig. 2.5 satisfies the following expression

$$C_{ox}\left(V_G - \frac{E_F}{e}\right) = en \tag{2.23}$$

C_{ox} is the dielectric oxide capacitance, V_G is the applied gate voltage. $\frac{E_F}{e}$ is the potential drop in the graphene. In metal, we generally ignore this potential drop, but this term can be important in semiconductor or semimetal like graphene. This term also appears in graphene spin valve device modeling in Chapter 3.

Differentiating Eq. 2.23 with respect to n,

$$\frac{dV_G}{d(en)} - \frac{1}{e^2}\frac{dE_F}{dn} = \frac{1}{C_{ox}} \tag{2.24}$$

which is equivalent to

$$\frac{1}{C_{tot}} - \frac{1}{e^2}\frac{1}{g(E_F)} = \frac{1}{C_{ox}} \tag{2.25}$$

Define $\frac{1}{C_{tot}} = \frac{dV_G}{d(en)}$ and $C_q = e^2 g(E_F)$, then we find equation for quantum capacitance

$$\frac{1}{C_{tot}} = \frac{1}{C_q} + \frac{1}{C_{ox}} \tag{2.26}$$

The total capacitance can be viewed as C_q in series with C_{ox}.

Considering both electron and hole,

$$C_{ox}\left(V_G - \frac{E_F}{e}\right) = e(n-p) \tag{2.27}$$

Following similar procedures as Eq. 2.24, we find that

$$\frac{dV_G}{de(n-p)} - \frac{1}{e^2}\frac{dE_F}{d(n-p)} = \frac{1}{C_{ox}} \tag{2.28}$$

For zero temperature condition,

$$C_q = e^2\frac{d(n-p)}{dE_F} = e^2\frac{d}{dE_F}\left(\frac{1}{2}aE_F{}^2\right) = ae^2E_F \tag{2.29}$$

For finite temperature, the electron density can be calculated from Eq. 2.20. Moreover, for Ferimi-Dirac integral F_j,

$$F_j = \frac{1}{\Gamma(j+1)}\int dE\,\frac{E^j}{1 + exp\left(\frac{E-E_F}{k_BT}\right)} \tag{2.30}$$

The differentiation F_{j-1} satisfy,

$$\frac{dF_j}{dE_F} = F_{j-1} = \frac{1}{\Gamma(j)} \int dE \frac{E^{j-1}}{1 + exp\left(\frac{E - E_F}{k_B T}\right)} \tag{2.31}$$

$\Gamma(j) = (j-1)!$ is the gamma function. Apply this property to Eq. 2.20,

$$\frac{dn}{dE_F} = a\frac{\Gamma(2)}{\Gamma(1)} \int dE \frac{1}{1 + exp\left(\frac{E - E_F}{k_B T}\right)}$$

$$= a\frac{\Gamma(2)}{\Gamma(1)} \left\{E_F + k_B T ln\left[1 + exp\left(-\frac{E_F}{k_B T}\right)\right]\right\} \tag{2.32}$$

The integral done in Eq. 2.32 is also utilized in the carrier density calculation for 2DEG later in Chapter. 4. Similarly, for holes

$$\frac{dp}{dE_F} = a\frac{\Gamma(2)}{\Gamma(1)} \left\{E_F - k_B T ln\left[1 + exp\left(\frac{E_F}{k_B T}\right)\right]\right\} \tag{2.33}$$

Therefore, for finite temperature

$$\frac{d(n-p)}{dE_F} = a k_B T \left\{ln\left[1 + exp\left(-\frac{E_F}{k_B T}\right)\right] + ln\left[1 + exp\left(\frac{E_F}{k_B T}\right)\right]\right\}$$

$$= a k_B T ln\left[2 + 2cosh\left(\frac{E_F}{k_B T}\right)\right] \tag{2.34}$$

Finally, the quantum capacitance for finite temperature can be written as

$$C_q = e^2 a k_B T ln\left[2 + 2cosh\left(\frac{E_F}{k_B T}\right)\right] \tag{2.35}$$

For Fermi energy align with Dirac point, i.e. $E_F = 0$,

$$C_q = e^2 a k_B T ln4 \tag{2.36}$$

Eq. 2.36 indicates the quantum capacitance has a non-zero minimum at Dirac point.[69][70][71] For $E_F \gg k_B T$, finite temperature C_q has the following approximation, which is the same as Eq. 2.29

$$C_q \approx e^2 a E_F \tag{2.37}$$

In this approximation, the quantum capacitance increases linearly with E_F, or the potential drop in

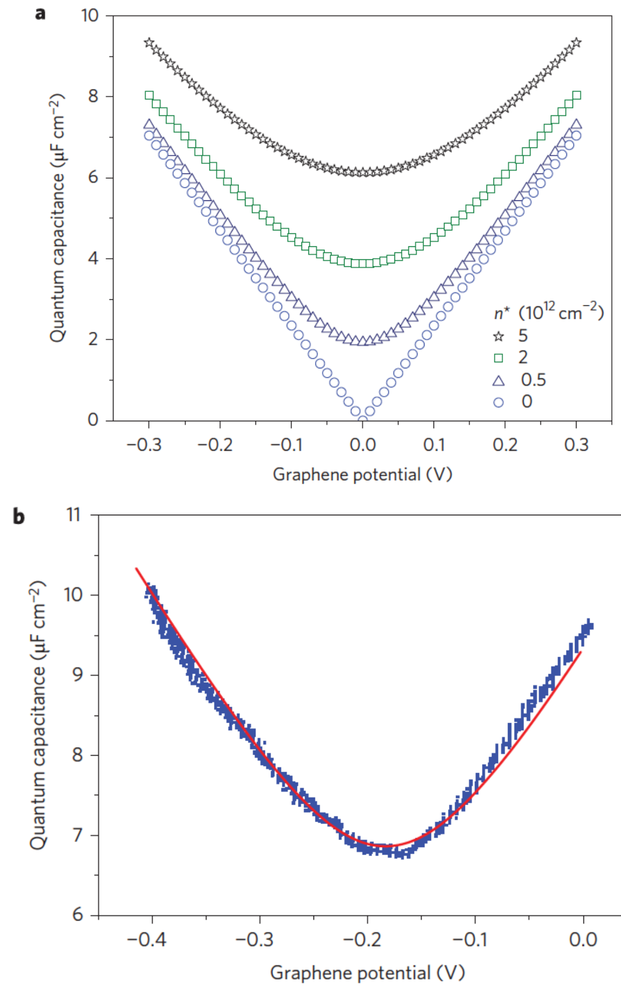

Fig. 2.6. Quantum capacitance in graphene.[70] (a) Calculations for different impurity density. (b) Experimental measurements with curve fitting.

graphene $V = \frac{E_F}{e}$. The calculation and experimental measurements of the quantum capacitance in graphene can be found in Fig. 2.6. The measured minimum is round since $V = \frac{E_F}{e}$ is small and thermal smearing is strong for room temperature measurements. For thick oxide $> 300nm$, the quantum capacitance effect can be usually neglected.[43]

Now we have reviewed basis electronic properties for graphene and we can proceed to discuss graphene transport behavior in the rest of Chapter 2.

2.2 Ballistic transport in graphene

In transport theory, if the carrier mean free path, λ_{MFP}, is much longer than the dimensions of the medium (e.g. device length), resistivity caused by scattering is negligible and ballistic transport is observed. Otherwise, the process is limited by different scattering mechanisms and it is called diffusive transport. As graphene has very high mobility, we start the transport study with a brief discussion of ballistic transport. In ballistic transport region, there will be a universal minimum conductivity for graphene.[52][54][72][73][74][75][76] (considering no disorder or electron-electron interaction).

Another interesting phenomenon related to ballistic transport is Klein tunneling[48][49][50][51][52][53][54], where Dirac electrons could transmute into holes and tunnel through a high potential barrier with nearly unity transmission probability. For graphene, it can be found that the transmission is perfect at angles normal to the barrier and there are reflections at other angles. At normal incidence, the incoming and reflected electron states are of opposite chirality, leading to vanishing reflection probability.

Once again we consider a back-gated device structure. For $\lambda_{MFP} \gg L$ in Fig. 2.7 (a), the device satisfies ballistic transport, a Landauer transport equation can be applied.[43][77][78]

$$I = -\frac{g_s e}{h} \int dE [f_R(E) - f_L(E)]\, T(E) \tag{2.38}$$

$T(E)$ is the transmission probability. f_L and f_R are Fermi-Dirac distributions in left and right with $f_L(E) = \frac{1}{1+exp\left(\frac{E-E_{FL}}{k_B T}\right)}$, $f_R(E) = \frac{1}{1+exp\left(\frac{E-E_{FR}+eV}{k_B T}\right)}$. Then $f_L(E) - f_R(E) \approx \frac{\partial f}{\partial E}(-eV)$. Applying a relatively small drain voltage bias, $E_{FL} \approx E_{FR}$, the Landauer conductance can be written as

$$G = \frac{dI}{dV} = \frac{2e^2}{h} \int dE \left(-\frac{\partial f}{\partial E}\right) T(E) \tag{2.39}$$

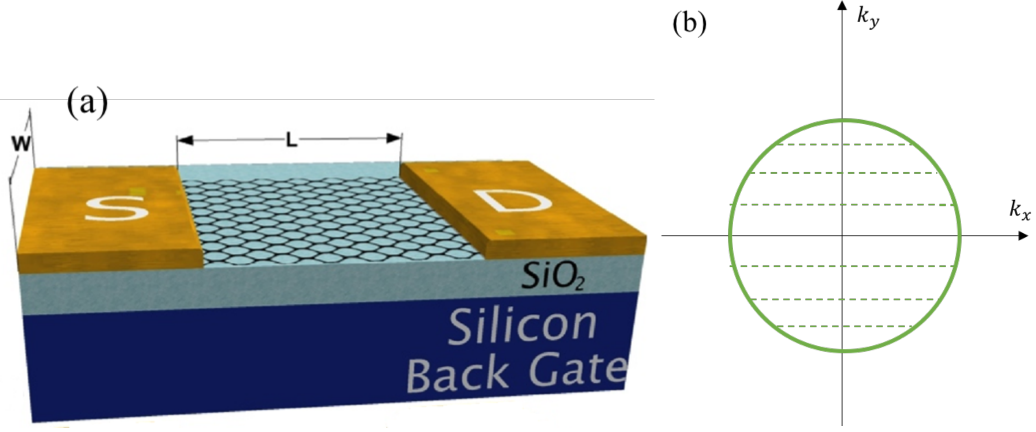

Fig. 2.7. Graphene ballistic transport. (a) $\lambda_{MFP} \gg L$.[79] (b) Counting number of modes.

At zero temperature, $-\frac{\partial f}{\partial E} = \delta(E - E_F)$, subsequently,

$$G = \frac{2e^2}{h}\int dE\delta(E - E_F)T(E) = \frac{2e^2}{h}T(E_F) \tag{2.40}$$

Generally, $G = G_0 \sum_n^M T_n(E_F)$, M is the number of propagating modes, T_n is the transmission probability for mode n. Please note that n is not the usual carrier density here. Assuming $T_n \sim 1$ and $G_0 = \frac{2e^2}{h}$ is the quantum conductance first found in QHE. For the graphene device in Fig. 2.7 (a) with a width of W, applying the period boundary condition, $k_{yn} = \frac{2n\pi}{W}$ could be found from Fig. 2.7 (b) and thus $n_{max} = \frac{Wk_F}{2\pi}$. Total modes number $M = g_I \cdot g_v \cdot n_{max} = \frac{2Wk_F}{\pi}$, with $g_I = g_v = 2$. The Landauer conductance can be found

$$G = \frac{2e^2}{h}\frac{2Wk_F}{\pi} \tag{2.41}$$

The minimum conductivity is given by $\sigma = G\frac{L}{W} = \frac{2e^2}{h}\frac{2k_F L}{\pi}$. More precisely, considering the exact transmission coefficient T_n across the Dirac point[43][72],

$$T_n = \frac{1}{cosh^2(\pi n\frac{L}{W})} \approx \frac{1}{cosh^2(k_n L)} \tag{2.42}$$

Then the minimum conductance for graphene can be written as

$$G_{min} = \frac{g_s g_v e^2}{h}\sum_{n}^{M} T_n$$

$$= \frac{g_s g_v e^2}{h}\sum_{n}^{M} \frac{1}{cosh^2(\,k_n L)}$$

$$= \frac{g_s g_v e^2}{h}\left(\frac{W}{2\pi}\right)\int_{-k_F}^{k_F} dk_y \frac{1}{cosh^2(k_y L)} = \frac{2e^2}{\pi h}\left(\frac{W}{L}\right)\left[\frac{sinh(k_y L)}{cosh(k_y L)}\right]_{-k_F}^{k_F}$$

$$= \frac{4e^2}{\pi h}\left(\frac{W}{L}\right)\frac{e^{k_F L} - e^{-k_F L}}{e^{k_F L} + e^{-k_F L}} \tag{2.43}$$

Since $k_F L \gg 1$ and $W \gg L$, $G_{min} \approx \frac{4e^2}{\pi h}\left(\frac{W}{L}\right)$. Then we find the ballistic minimum conductivity

$$\sigma_{min} = G_{min}\frac{L}{W} = \frac{2e^2}{h}\frac{2}{\pi} \tag{2.44}$$

$\sigma_{min} = \frac{4e^2}{h\pi}$ is a finite and universal value. Some comparison of theoretical calculation and experimental data can be found in following Fig. 2.8.[43]

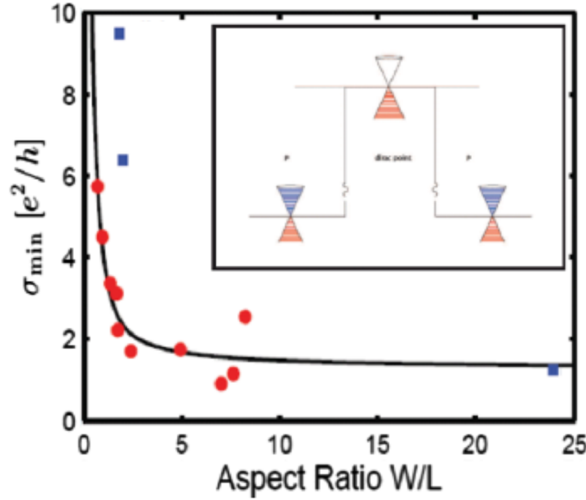

Fig. 2.8. Solid line is calculated Dirac point ballistic conductivity.[72] For $W \gg L$ the theory approaches the universal value $\frac{4e^2}{h\pi}$. Circles show experimental data taken from Miao et al.[80], and squares show the data from Danneau et al.[81].

We conclude our brief discussion on graphene ballistic transport with the universal minimum conductivity $\sigma_{min} = \frac{4e^2}{\pi h}$. For real graphene or 2D materials electronic devices for semiconductor applications, diffusive transport (semi-classical Boltzmann transport theory) is more important. More detailed topics on ballistic and quantum mechanical transport effects in graphene can be found in the literature.[72][73][74][75][76][77][80][81]

2.3 Diffusive transport in graphene, a linear Thomas Fermi approach

Compared to the ballistic transport covered in last session, diffusive transport occurs when $L \gg \lambda_{MFP}$. The Boltzmann transport equation (BTE) is used as a standard way to study diffusive transport.[82]

$$\frac{\partial f}{\partial t} + \vec{v} \cdot \nabla_{\vec{r}} f - \frac{e\vec{\xi}}{\hbar} \cdot \nabla_{\vec{k}} f = \left(\frac{\partial f}{\partial t}\right)_{scatter} \tag{2.45}$$

$\vec{v}$ is the carrier velocity , $\vec{\xi}$ is the applied electric field. In steady state without $\vec{r}$ dependence, Eq. 2.45 can be simplified into a reduced Boltzmann equation. Applying the relaxation time approximation and considering a low field $|\vec{\xi}|$ for linear response, we arrive at

$$-\frac{e\vec{\xi}}{\hbar} \cdot \nabla_{\vec{k}} f = \left(\frac{\partial f}{\partial t}\right)_{scatter} = -\frac{f(\vec{k}) - f_0(\vec{k})}{\tau(\vec{k})} \tag{2.46}$$

$$f(\vec{k}) = f_0(\vec{k}) + \frac{e}{\hbar}\left[\vec{\xi} \cdot \nabla_{\vec{k}} f_0(\vec{k})\right]\tau(\vec{k}) \tag{2.47}$$

The transition rate from state $|\vec{k}\rangle$ to state $|\vec{k}'\rangle$ is denoted as $P_{\vec{k},\vec{k}'}$ and can be written down by Fermi's golden rule

$$P_{\vec{k},\vec{k}'} = \frac{2\pi}{\hbar} \left|\langle\vec{k}'|H|\vec{k}\rangle\right|^2 n_{imp} \delta\left[E(\vec{k}') - E(\vec{k})\right] \tag{2.48}$$

n_{imp} is the impurity concentration, H is once again the interactive Hamiltonian. For elastic scattering mechanisms such as ionized impurity scattering, energy is conserved and

$P_{\vec{k},\vec{k}\prime} = P_{\vec{k}\prime,\vec{k}}$ can be satisfied. Applying the famous detailed balanced equation[82], we arrive with

$$\left(\frac{\partial f}{\partial t}\right)_{scatter} = \sum_{\vec{k}\prime} P_{\vec{k},\vec{k}\prime}\left[f\left(\vec{k}'\right) - f\left(\vec{k}\right)\right] \tag{2.49}$$

Substitute Eq. 2.49 into Eq. 2.46, after some mathematical rearrangement, the momentum relaxation time for isotropic material can be written down as

$$\frac{1}{\tau_m\left(\vec{k}\right)} = \frac{1}{(2\pi)^2} \int_{all\,\vec{k}'} d^2k'\, P_{\vec{k},\vec{k}\prime}(1 - cos\theta) \tag{2.50}$$

scattering angle $\theta = \theta_{\vec{k}\prime} - \theta_{\vec{k}}$, and $\theta_{\vec{k}}$ is the angle for incoming state wave vector $|\vec{k}\rangle$. Since graphene is an isotropic material, $\tau_m = \tau_m\left(\left|\vec{k}\right|\right)$. In other words, τ_m is independent of the direction of $|\vec{k}\rangle$ for the isotropic system. We will discuss cases of anisotropic materials such as black phosphorus in later chapters. More information on BTE and relaxation time derivation can be found in the Appendix. A.

We start with schematic model in Fig. 2.9 to study diffusive transport. To be specific, we consider an atomically thin, infinite sheet of graphene on a SiO_2 insulator with a non-magnetic, ionized impurity that is located a distance z_0 below the graphene- SiO_2 interface. The modeled geometry is cylindrically symmetric. We focus on electrons in this section and thus graphene is *n*-type doped.

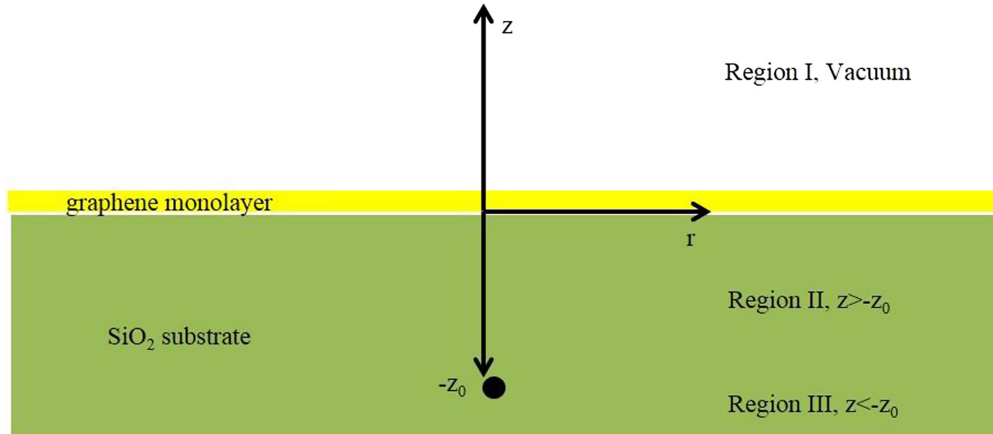

Fig. 2.9. Schematic modeling of a back-gated graphene device (e.g. Fig. 2.5) with out-of-plane impurity. The graphene is located at the $z = 0$ plane and the impurity charge is located at $-z_0$ ($z_0 > 0$).

Among all the scattering mechanisms, we mainly consider ionized impurity scattering (in some literature also called charged impurity interaction or Coulomb impurity interaction) because (1) ionized impurity scattering is the dominating mechanism in low temperature transport (e.g. $T < 100K$); (2) ionized impurity scattering is relatively straightforward. Once we get familiar with the calculation procedures, we can extend our theory to other scattering mechanisms by switching the interaction Hamiltonian.

For ionized impurity interaction, the scattering potential energy at $(\vec{r}, z)$ can be written as[1][3]

$$U(\vec{r}, z) = \frac{e^2}{\kappa_1}\left(\frac{1}{R_1} - \frac{\kappa_2 - \kappa_1}{\kappa_2 + \kappa_1}\frac{1}{R_2}\right) \quad (2.51)$$

$R_1 = \sqrt{r^2 + (z_0 + z)^2}$ and $R_2 = \sqrt{r^2 + (z_0 - z)^2}$, the factor $\frac{\kappa_2 - \kappa_1}{\kappa_2 + \kappa_1}$ is due to image charge effect. For the graphene monolayer at $z = 0$, plugging $z = 0$ into R_1 and R_2, Eq. 2.51 reduces to

$$U(\vec{r}) = U(r) = \frac{e^2}{\kappa\sqrt{r^2 + {z_0}^2}} \quad (2.52)$$

The effective $\kappa = \frac{\kappa_1 + \kappa_2}{2} = \frac{1}{2}(3.9 + 1) \approx 2.5$, with κ_1 and κ_2 are dielectric constants of SiO_2 and vacuum, respectively. For ionized impurity scattering limited graphene, Hamiltionian H is the Coulomb potential energy $U(r)$.

From Eq. 2.15 in Section 2.1, we have

$$|\vec{k}\rangle = \frac{1}{\sqrt{2}}\begin{pmatrix} e^{-i\frac{\theta_{\vec{k}}}{2}} \\ e^{i\frac{\theta_{\vec{k}}}{2}} \end{pmatrix} e^{i\vec{k}\cdot\vec{r}} \quad (2.53)$$

The scattering matrix $\langle\vec{k}'|H|\vec{k}\rangle$ be written as

$$\langle\vec{k}'|H|\vec{k}\rangle = \frac{1}{2}\begin{pmatrix} e^{i\frac{\theta_{\vec{k}\prime}}{2}} & e^{-i\frac{\theta_{\vec{k}\prime}}{2}} \end{pmatrix}\begin{pmatrix} e^{-i\frac{\theta_{\vec{k}}}{2}} \\ e^{i\frac{\theta_{\vec{k}}}{2}} \end{pmatrix}\int d^2r e^{i(\vec{k}\prime - \vec{k})\cdot\vec{r}}\frac{e^2}{\kappa\sqrt{r^2 + {z_0}^2}} \quad (2.54)$$

We define the transfer wave vector $\vec{q} = \vec{k}' - \vec{k}$, and the scattering matrix becomes

$$\langle\vec{k}'|H|\vec{k}\rangle = \frac{e^2}{\kappa}cos\frac{\theta}{2}\int_0^\infty dr\, \frac{r}{\sqrt{r^2 + {z_0}^2}}\int_0^{2\pi} d\theta e^{iqrcos\theta} \quad (2.55)$$

The integrals in Eq. 2.55 can be done analytically with following two integral identities. It is worth mentioning that Eq. 2.56a and 2.56b are very commonly used in 2D materials transport theory.

$$\int_0^{2\pi} d\theta e^{iqrcos\theta} = 2\pi J_0(qr) \quad (2.56a)$$

$$\int_0^{\infty} dr \frac{r}{\sqrt{r^2 + {z_0}^2}} J_0(qr) = \frac{e^{-qz_0}}{q} \quad (2.56b)$$

J_0 is the Bessel function of order zero. The potential energy in reciprocal space, $\widehat{U}(\vec{q})$, can be solved using Fourier transform as shown in Eq. 2.57a. (a hat notation is used to distinguish real space and Fourier space). Subsequently, the scattering matrix $\langle \vec{k}' | H | \vec{k} \rangle$ can be written as Eq. 2.57b.

$$\widehat{U}(\vec{q}) = \widehat{U}(q) = \int d^2 r \, e^{i\vec{q}\cdot\vec{r}} U(r) = \frac{2\pi e^2}{\kappa} \frac{e^{-qz_0}}{q} \quad (2.57a)$$

$$\langle \vec{k}' | H | \vec{k} \rangle = \widehat{U}(q) cos \frac{\theta}{2} \quad (2.57b)$$

It is worth noticing that calculating the scattering matrix in Eq. 2.54-2.55 includes the same approach as doing the Fourier transform. Moreover, we find that both $U(r)$ and $\widehat{U}(q)$ only depends on the magnitude of $r = |\vec{r}|$ or $q = |\vec{q}|$, which is true for graphene since it is an isotropic material. For anisotropic material, such as black phosphorus, $U(\vec{r})$ or $\widehat{U}(\vec{q})$ with full vector dependence may be needed, as discussed in Chapter 4.

Before we proceed to evaluate the diffusive transport in graphene due to ionized impurity scattering, we also need to consider the effect of electron screening. We start with a simple linear Thomas-Fermi screening. Considering the screening effect, the $\widehat{U}(q)$ in Eq. 2.57a is modified to be

$$\widehat{U}(q) = \frac{2\pi e^2}{\kappa} \frac{e^{-qz_0}}{q + q_s} = \frac{2\pi e^2 e^{-qz_0}}{q\kappa + 2\pi e^2 a E_F} \quad (2.58)$$

Within the linear Thomas-Fermi screening, q_s is given by $q_s = \frac{2\pi e^2}{\kappa} g(E_F)$.[3] Finally, we arrive with the following scattering matrix

$$\langle \vec{k}' | H | \vec{k} \rangle = \frac{2\pi e^2}{\kappa} \frac{e^{-qz_0}}{q + \frac{2\pi e^2}{\kappa} g(E_F)} \cos\frac{\theta}{2} = \frac{2\pi e^2 e^{-qz_0}}{q\kappa + 2\pi e^2 a E_F} \cos\frac{\theta}{2} \quad (2.59)$$

Substituting Eq. 2.59 into the transition rate Eq. 2.48,

$$P_{\vec{k},\vec{k}'} = \frac{2\pi}{\hbar} \left| \widehat{U}(q) \right|^2 \left(\frac{1 + \cos\theta}{2} \right) n_{imp} \delta\left[E(\vec{k}') - E(\vec{k}) \right] \quad (2.60)$$

Using Eq. 2.50, the momentum relaxation time τ_m can be written as

$$\frac{1}{\tau_m} = \frac{1}{(2\pi)^2} \frac{\pi n_{imp}}{\hbar} \int_{all\ \vec{k}'} d^2k' \left| \widehat{U}(q) \right|^2 (1 + \cos\theta)(1 - \cos\theta) \delta\left[E(\vec{k}') - E(\vec{k}) \right] \quad (2.61)$$

Since $E(\vec{k}) = \hbar v_F k$, $\delta\left[E(\vec{k}') - E(\vec{k}) \right] = \frac{\delta(k'-k)}{\hbar v_F}$, and $q = 2k\sin\frac{\theta}{2} = \frac{2E}{\hbar v_F}\sin\frac{\theta}{2}$ can be found in Fig. 2.10 for isotropic elastic scattering process, the momentum relaxation time calculated by Eq. 2.61 can be simplified to

$$\frac{1}{\tau_m} = \frac{n_{imp}}{4\pi\hbar} \int dk' k' \frac{\delta(k'-k)}{\hbar v_F} \int_0^{2\pi} d\theta \left| \widehat{U}(q) \sin\theta \right|^2$$

$$= \frac{n_{imp} E}{4\pi\hbar^3 {v_F}^2} \int_0^{2\pi} d\theta \left| \widehat{U}(q) \sin\theta \right|^2 \quad (2.62)$$

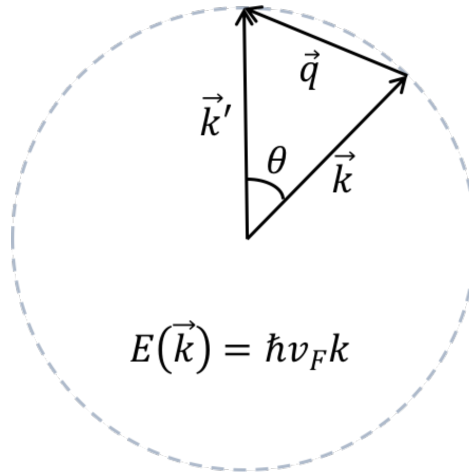

Fig. 2.10. Schematic for transfer vector $\vec{q} = \vec{k}' - \vec{k}$.

The second term $\int_0^{2\pi} d\theta \left|\hat{U}(q)sin\theta\right|^2$ in Eq. 2.62 is an integral which is solely determined by E. We assert that for isotropic material such as graphene, τ_m is indeed determined by carrier energy only, i.e. independent of incoming state direction.

Another prospective to evaluate the ionized impurity scattering in graphene is to look at the differential scattering cross-section $\left.\frac{d\sigma}{d\theta}\right|_{k\to k\prime}$ and scattering amplitude $f_B(\theta)$.[83][84] In the lowest order Born approximation, the scattering amplitude for graphene can be found in Novikov[85]

$$f_B(\theta) = -\frac{1}{\hbar v_F}\sqrt{\frac{k}{8\pi}}\hat{U}(q)\left(1+e^{-i\theta}\right) \tag{2.63}$$

Considering $\left(1+e^{-i\theta}\right)^2 = 4cos^2\frac{\theta}{2}e^{-i\theta}$, differential scattering cross-section become

$$\left.\frac{d\sigma}{d\theta}\right|_{k\to k\prime} = |f_B(\theta)|^2 = \frac{E}{2\pi(\hbar v_F)^3}\left|\hat{U}(q)\right|^2 cos^2\frac{\theta}{2} \tag{2.64}$$

Alternatively, $\left.\frac{d\sigma}{d\theta}\right|_{k\to k\prime}$ can also be related with the scattering matrix $\langle\vec{k}'|H|\vec{k}\rangle$[86]

$$\left.\frac{d\sigma}{d\theta}\right|_{k\to k\prime} = \frac{g_{E(\vec{k}\prime)}}{4\hbar v_F}\left|\langle\vec{k}'|H|\vec{k}\rangle\right|^2 \tag{2.65}$$

$g_{E(\vec{k}\prime)}$ is the DOS for final state $|\vec{k}'\rangle$, i.e. $g_{E(\vec{k}\prime)} = \frac{2}{\pi(\hbar v_F)^2}E$. Plugging the scattering matrix (Eq. 2.57b) in Eq. 2.65 and we obtain same expression as Eq. 2.64

$$\left.\frac{d\sigma}{d\theta}\right|_{k\to k\prime} = \frac{E}{2\pi(\hbar v_F)^3}\left|\hat{U}(q)\right|^2 cos^2\frac{\theta}{2} \tag{2.66}$$

The momentum relaxation time can be written as[87]

$$\frac{1}{\tau_m} = n_{imp}v_F\sigma(E) \tag{2.67}$$

$\sigma(E)$ is the total scattering cross-section, which can be calculated by integrating $\left.\frac{d\sigma}{d\theta}\right|_{k\to k\prime}$,

$$\begin{aligned}\sigma(E) &= \int d\theta \left.\frac{d\sigma}{d\theta}\right|_{k\to k\prime}(1-cos\theta) \\ &= \frac{E}{2\pi(\hbar v_F)^3}\int d\theta\left|\hat{U}(q)\right|^2 cos^2\frac{\theta}{2}(1-cos\theta)\end{aligned} \tag{2.68}$$

The $(1 - cos\theta)$ term in Eq. 2.68 corresponds to the isotropic momentum (or potential) relaxation process in graphene. This term appears in Eq. 2.50, too. Subsequently the relaxation time τ_m can be recovered,

$$\frac{1}{\tau_m} = n_{imp} v_F \sigma(E) = \frac{n_{imp} E}{4\pi\hbar^3 {v_F}^2} \int_0^{2\pi} d\theta \left|\widehat{U}(q) sin\theta\right|^2 \tag{2.69}$$

which is identical to Eq. 2.62. Thus we have demonstrated how to calculate momentum relaxation either directly from BTE, or using the differential scattering cross-section approach.

At this point, we can numerically compute τ_m from Eq. 2.62 with physical parameters for our model. Considering the monolayer *n*-type graphene has an electron density $n = 10^{12} cm^{-2}$, the corresponding Fermi energy $E_F = 0.12 eV$ can be calculated using Eq. 2.19. Assuming zero temperature for convenience in estimation, scattering only occurs at Fermi energy, i.e. $E = E_F$. We use impurity density $n_{imp} = 10^{11} cm^{-2}$, impurity distance $z_0 = 10 nm$, numerical integral can be evaluated that $\int_0^{2\pi} d\theta \left|\widehat{U}(q) sin\theta\right|^2 \approx 1.83\times10^{-28} eV^2 cm^4$ and thus relaxation time $\tau_m \approx 1.7\times10^{-11} s$, or $17 ps$ can be calculated using Eq. 2.62.

With τ_m known, we can continue to calculate other important electrical parameters such as the carrier mobility and conductivity/resistivity. It is worth mentioning that while conventional semiconductor mobility μ can be estimated from the Drude model $\mu = \frac{e\tau_m}{m^*}$, where m^* is the effective mass, this expression needs to be modified for massless Dirac electron in graphene. Analogous to the famous $E = mc^2$ relation in relativistic mechanic, we set $m^* = \frac{E_F}{{v_F}^2}$ and mobility in graphene can be written as

$$\mu = \frac{e {v_F}^2 \tau_m}{E_F} \tag{2.70}$$

Plugging $\tau_m = 17 ps$ into Eq. 2.69, a mobility $\mu \approx 1.43\times10^6 cm^2 V^{-1} s^{-1}$ can be calculated, which reveals why graphene has very high carrier mobility, taking account of ionized impurity scattering.

More generally, the energy E in Eq. 2.62 does not have to be the Fermi energy E_F. Using same parameters mentioned above, the potential energy $\widehat{U}$ in Fourier space as a function of wave vector k and scattering angle θ are plotted in Fig. 2.11a and Fig. 2.11b.

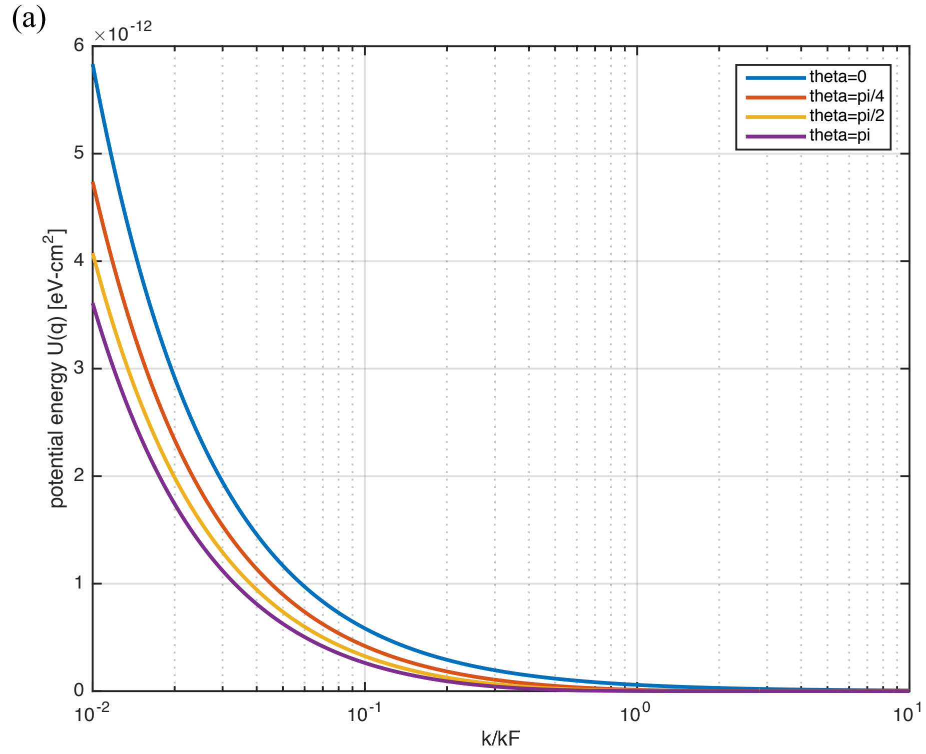

(b)

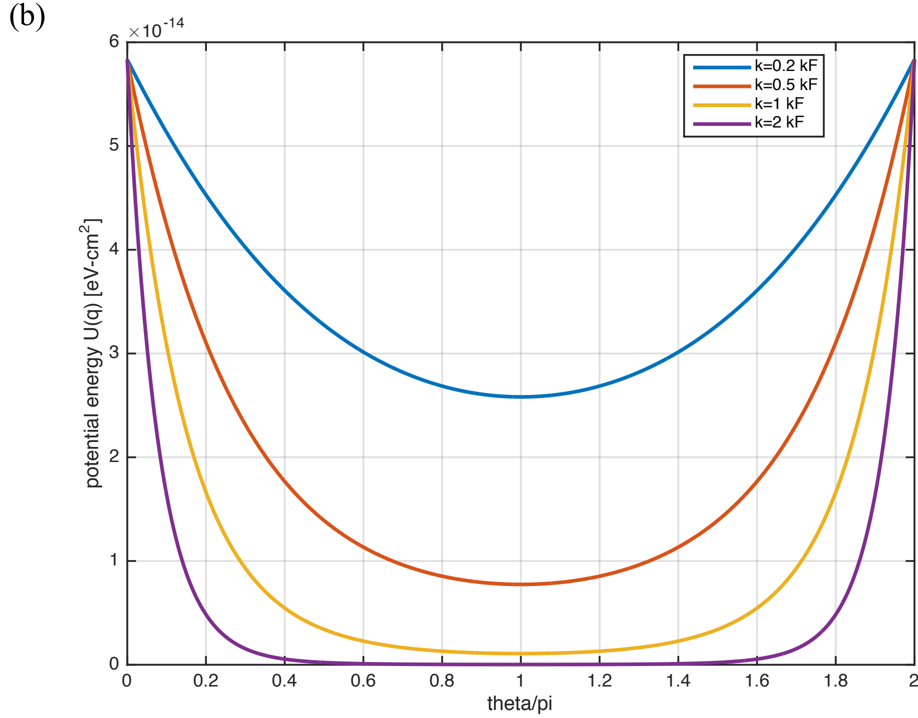

Fig. 2.11. Potential energy $\widehat{U}(q) = \frac{2\pi e^2}{\kappa}\frac{e^{-qz_0}}{q+q_s}$, $q = 2ksin\frac{\theta}{2}$, $z_0 = 10nm$. (a) $\widehat{U}$ as a function of k (normalized to k_F) for different scattering angle θ. (b) $\widehat{U}$ as a function of θ (normalized to π) for different wave vector k.

We find that as k increasing, $\widehat{U}$ decreases for a constant θ. For larger θ, $\widehat{U}$ decreases faster in Fig. 2.11a due to the exponential term in Eq. 2.58. For $\theta = 0$ (forward scattering), $\widehat{U}$ inversely varies with k since in this case $q = 0$. For wave vector $k \to 0$, potential energy $\widehat{U} \to \infty$.

Calculating the angle integral in Eq. 2.62 for every E, we can plot τ_m as a function of E in Fig. 2.12. $\tau_m = 17ps$ can be once again found for $E = E_F$, $z_0 = 10nm$ in the plot. As E increases, q increases, $\widehat{U}(q)$ decreases, and τ_m first decreases then increases due to Eq. 2.62. For low temperature, most scattering events occurs around Fermi energy, therefore it is reasonable to set $E = E_F$ when estimating relaxation time and mobility. (The scattering follows a distribution as $\left(-\frac{\partial f}{\partial E}\right) = \frac{1}{k_BT}f(E)\cdot[1 - f(E)]$, which reduces to delta function for $T = 0K$. We will revisit finite temperature ionized impurity scattering in Chapter 4.)

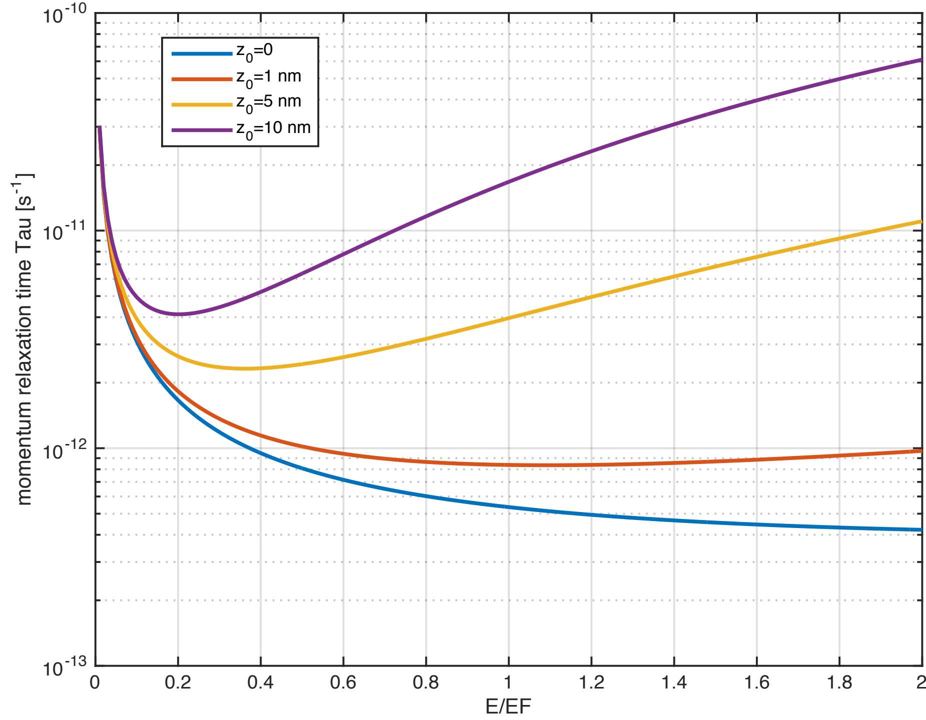

Fig. 2.12. Momentum relaxation time τ_m as a function of carrier energy E (normalized to E_F) for different impurity distance z_0.

Diffusive transport in graphene with linear Thomas Fermi screening (Eq. 2.58) is studied in Section 2.3. Ionized impurity scattering is used to illustrate the calculation procedures. Momentum relaxation time in graphene can be derived from BTE or using differential cross-section. As graphene is an isotropic material, τ_m is solely determined by E (i.e. τ_m depends on magnitude of incoming $\vec{k}$, rather than the angle). Numerically calculated $\widehat{U}(q)$ and τ_m are plotted and discussed in the end. We will explore non-linear Thomas Fermi screening in next session.

2.4 Non-linear Thomas Fermi screening for graphene

In last section, we derived the ionized impurity scattering limited relaxation time under linear Thomas Fermi screening. As the graphene DOS varies rapidly with energy

near the Dirac point (from zero to finite value), many interesting phenomena raise. For instance, the graphene DOS vanishes at Dirac point, but due to the inevitable presence of disorder, Dirac point can be locally shifted and cause non-zero local density.[43] As a result, electron-rich and hole-rich puddles will arise (see Fig. 2.13).[58] These puddles contribute to graphene's non-zero minimal conductivity at zero average carrier density that discussed in Section 2.2.

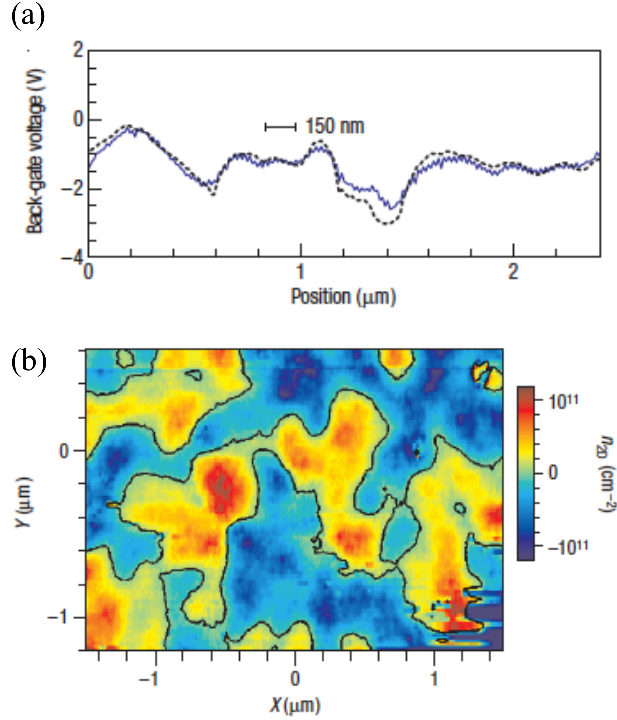

Fig. 2.13. Dirac point and carrier density measured as a function of position[58] (a) Spatial variation of the Dirac point using two methods: the inverse compressibility (black dashed line) and through subtracting surface potential scans at high and zero average carrier density (blue line) (b) Color map of the spatial density variations in the graphene flake extracted from surface potential measurements at high density and when the average carrier density is zero. The blue regions correspond to holes and the red regions to electrons.

Due to the rapid variation of DOS near the Dirac point, more accurate modeling becomes necessary to study graphene diffusive transport. For example, the screening term $q_s = \frac{2\pi e^2}{\kappa} g(E)$ as well as the potential energy $\widehat{U}(q)$ in Eq. 2.58 need to be improved. This section introduces a self-consistent non-linear Thomas Fermi approach to evaluate the screening effect.

According to Eq. 2.19, the induced monolayer electron density n (due to potential energy) can be expressed by the following equation for zero temperature,

$$n(r) = \int_{E_F}^{E_F+U(r)} g(E)\, dE = \frac{1}{2}a\big(E_F + U(r)\big)^2 - \frac{1}{2}aE_F{}^2 = aE_F U(r) + \frac{1}{2}aU^2 \quad (2.71)$$

Taking the 2D Fourier transform of $n(r)$, we get $\hat{n}(q)$, i.e. the electron density in reciprocal space

$$\hat{n}(q) = aE_F\hat{U}(q) + \frac{1}{2}a\left[\iint d^2r\, e^{i\vec{q}\cdot\vec{r}}U^2(r)\right] \quad (2.72)$$

The three dimensional Poisson's equation in real space for a point charge in the same monolayer graphene model in Fig. 2.9 can be written as,

$$\frac{\partial^2 U}{\partial x^2} + \frac{\partial^2 U}{\partial y^2} + \frac{\partial^2 U}{\partial z^2} = -\frac{4\pi e^2}{\kappa}[\delta(x,y,z+z_0) - n(x,y)\delta(z)] \quad (2.73)$$

Again $\kappa \approx 2.5$ is the effective dielectric constant between vacuum and SiO_2. Applying 2D Fourier transform to Eq. 2.73 in the xy plane and leaving the vertical z direction in real space,

$$-q^2\hat{U}(q,z) + \frac{d}{dz^2}\hat{U}(q,z) = -\frac{4\pi e^2}{\kappa}[\delta(z+z_0) - \hat{n}(q)\delta(z)] \quad (2.74)$$

The partial differential equation (PDE) in Eq. 2.73 has been simplified to an ordinary second order differential equation (ODE) with respect to z, which can be solved in forms of

$$\hat{U}(q,z) = \begin{cases} Ae^{-qz} + Be^{-q(z+z_0)}, & \text{(Region I)} \\ Ae^{qz} + Be^{-q(z+z_0)}, & \text{(Region II)} \\ Ae^{qz} + Be^{q(z+z_0)}, & \text{(Region III)} \end{cases} \quad (2.75)$$

Coefficients A and B can be found using the following boundary conditions,

$$\frac{d}{dz}\hat{U}\Big|_{-z_0{}^+} - \frac{d}{dz}\hat{U}\Big|_{-z_0{}^-} = -\frac{4\pi e^2}{\kappa}\hat{n}(q) \quad (2.76a)$$

$$\frac{d}{dz}\hat{U}\Big|_{-z_0{}^+} - \frac{d}{dz}\hat{U}\Big|_{-z_0{}^-} = -\frac{4\pi e^2}{\kappa} \quad (2.76b)$$

Subsequently, $A = -\frac{2\pi e^2}{\kappa q}\hat{n}(q)$ and $B = \frac{2\pi e^2}{\kappa q}$ can be solved. Once again by setting the vertical direction $z = 0$, we focus on the monolayer graphene plane only. Then the potential energy in Fourier space for $z = 0$ plane can be expressed as

$$\hat{U}(q) = -\frac{2\pi e^2}{\kappa q}\left[\hat{n}(q) - e^{-qz_0}\right] \tag{2.77}$$

Defining $\hat{T}(q) = \frac{\hat{n}(q)}{\hat{U}(q)}$ and using Eq. 2.72,

$$\hat{T}(q) = \frac{aE_F\hat{U}(q) + \frac{1}{2}a\left[\int d^2r\, e^{i\vec{q}\cdot\vec{r}}U^2(r)\right]}{\hat{U}(q)} \tag{2.78}$$

Recalling the following two inverse Fourier transforms,

$$U(r) = \frac{1}{(2\pi)^2}\int d^2q\, e^{-i\vec{q}\cdot\vec{r}}\,\hat{U}(q) \tag{2.79a}$$

$$U^2(r) = \frac{1}{(2\pi)^4}\int d^2q \int d^2q'\, e^{-i\vec{q}\cdot\vec{r}}\, e^{-i\vec{q}\prime\cdot\vec{r}}\,\hat{U}(q)\hat{U}(q') \tag{2.79b}$$

We define $FT\{U^2(r)\} = \int d^2r\, e^{i\vec{q}\prime\cdot\vec{r}}U^2(r)$ in Eq. 2.78, thus the Fourier transform of $U^2(r)$ can be expressed as

$$FT\{U^2(r)\} = \int d^2r\, U^2(r)\, e^{-i\vec{q}'\cdot\vec{r}}$$

$$= \frac{1}{(2\pi)^4}\int d^2q \int d^2q''\,\hat{U}(q)\hat{U}(q'')\left[\int d^2r\, e^{-i(\vec{q}\prime-\vec{q}-\vec{q}\prime\prime)\cdot\vec{r}}\right] \tag{2.80}$$

Applying the following delta function property,

$$\delta(\vec{q}' - \vec{q} - \vec{q}'') = \frac{1}{(2\pi)^2}\int d^2r\, e^{-i(\vec{q}\prime-\vec{q}-\vec{q}\prime\prime)\cdot\vec{r}} \tag{2.81}$$

Therefore, $FT\{U^2(r)\}$ can be further simplified to,

$$FT\{U^2(r)\} = \frac{1}{(2\pi)^4}\int d^2q \int d^2q''\,\hat{U}(q)\hat{U}(q'')[(2\pi)^2\delta(\vec{q}' - \vec{q} - \vec{q}'')]$$

$$= \frac{1}{(2\pi)^2}\int d^2q\,\hat{U}(q)\int d^2q''\,\delta[\vec{q}'' - (\vec{q}' - \vec{q})]\hat{U}(q'')$$

$$= \frac{1}{(2\pi)^2}\int d^2q\;\hat{U}(q)\hat{U}(|\vec{q}' - \vec{q}|) \tag{2.82}$$

Substituting results in Eq. 2.82 into Eq. 2.78, we find $\hat{T}(q)$ which is responsible for the non-linear screening

$$\hat{T}(q) = aE_F + \frac{1}{2}a\frac{\frac{1}{(2\pi)^2}\int d^2q'\;\hat{U}(q')\hat{U}(|\vec{q} - \vec{q}'|)}{\hat{U}(q)} \tag{2.83}$$

Plugging $\hat{n}(q) = \hat{T}(q)\hat{U}(q)$ into Eq. 2.77, the potential energy including non-linear screening become

$$\hat{U}(q) = \frac{2\pi e^2 e^{-qz_0}}{\kappa q + 2\pi e^2 \hat{T}(q)} \tag{2.84}$$

Comparing Eq. 2.58 and 2.84, we find both $\hat{U}(q)$ share a same form, except now $q_s = \frac{2\pi e^2}{\kappa}\hat{T}(q)$, which is a non-linear screening due to the complication in Eq. 2.83. However, if we ignore the second term in Eq. 2.83, then there is only $\hat{T}(q) = aE_F$ left. Potential energy expression is reduced to Eq. 2.58, i.e. the linear screening again. Therefore, the second term, $\frac{1}{2}a\frac{\frac{1}{(2\pi)^2}\int d^2q'\,\hat{U}(q')\hat{U}(|\vec{q}-\vec{q}'|)}{\hat{U}(q)}$, can be viewed as a correction term. Due to the rapid change of the density of states near the Dirac point, this correction may take up to 30% of screening effect.[88]

With Eq. 2.83 and Eq. 2.84, $\hat{U}(q)$ and $\hat{T}(q)$ can be calculated self-consistently in the following iteration approach using supercomputers or high performance computing machines[89]

$$\hat{T}^0 = aE_F \qquad \hat{U}^0 = \frac{2\pi e^2 e^{-qz_0}}{\kappa q + 2\pi e^2 \hat{T}^0}$$

$$\hat{T}^1 = aE_F + \frac{1}{2}a\frac{\frac{1}{(2\pi)^2}\int d^2q'\ \hat{U}^0(q')\hat{U}^0(|\vec{q}-\vec{q}'|)}{\hat{U}^0(q)} \qquad \hat{U}^1 = \frac{2\pi e^2 e^{-qz_0}}{\kappa q + 2\pi e^2 \hat{T}^1}$$

$$\vdots$$

$$\vdots$$

$\hat{T}^i$ and $\hat{U}^i$ stands for i-th iteration. $U(r)$ and $\hat{U}(q)$ are plotted in Fig. 2.14 after the calculation convergence reached (e.g. $\frac{|\hat{T}^{i+1}-\hat{T}^i|}{|\hat{T}^i|}$ and $\frac{|\hat{U}^{i+1}-\hat{U}^i|}{|\hat{U}^i|}$ become smaller than 0.1%). $U(r)$ can be solved using the inverse Fourier transform and simplified with Eq. 2.56a.

$$U(r) = \frac{1}{2\pi}\int_0^\infty dq\; q\hat{U}(q)J_0(qr) \tag{2.85}$$

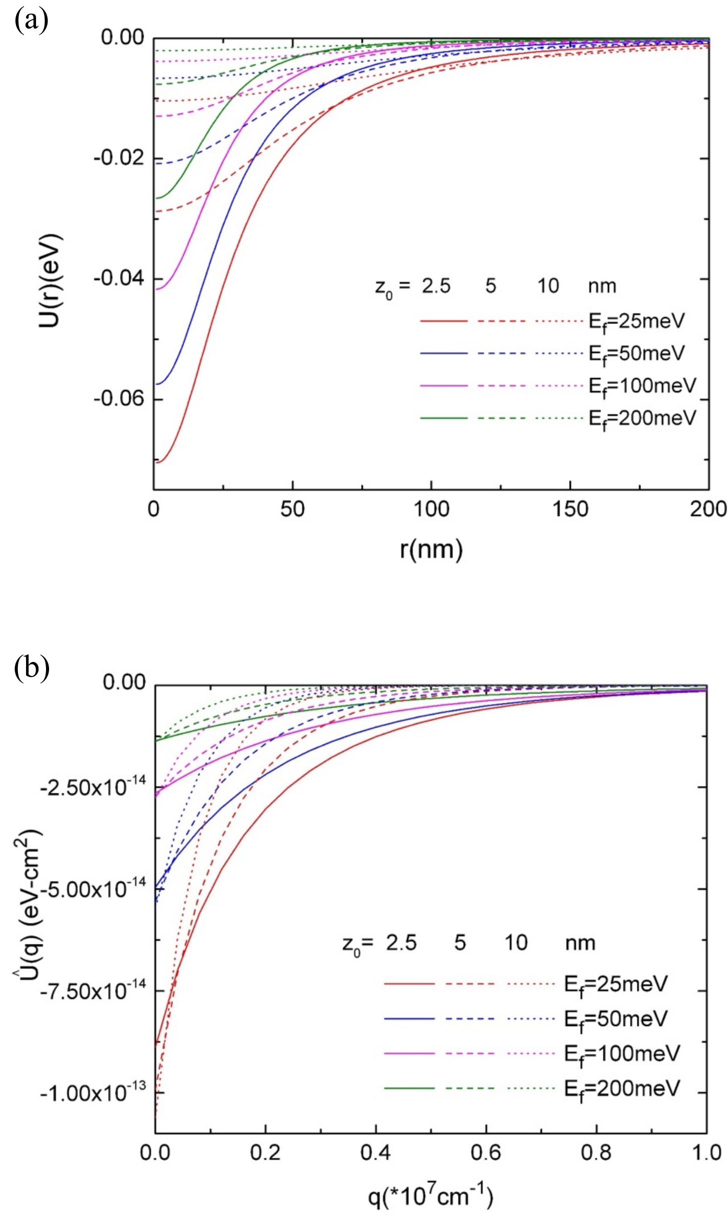

Fig. 2.14. Potential energy calculation using non-linear linear screening model. (a) $U(r)$ in real space. (b) $\widehat{U}(q)$ in Fourier space.

Four different Fermi energies are used: $25meV$, $50meV$, $100meV$, and $200meV$; corresponding to electron sheet densities n of $4.59\times10^{10}cm^{-2}$, $1.84\times10^{11}cm^{-2}$, $7.35\times10^{11}cm^{-2}$ and $2.94\times10^{12}cm^{-2}$. As a comparison to linear screening discussed in last

session, we can plot the potential energy as a function of q using Eq. 2.58 in Fig. 2.15, for the same E_F and z_0 values.

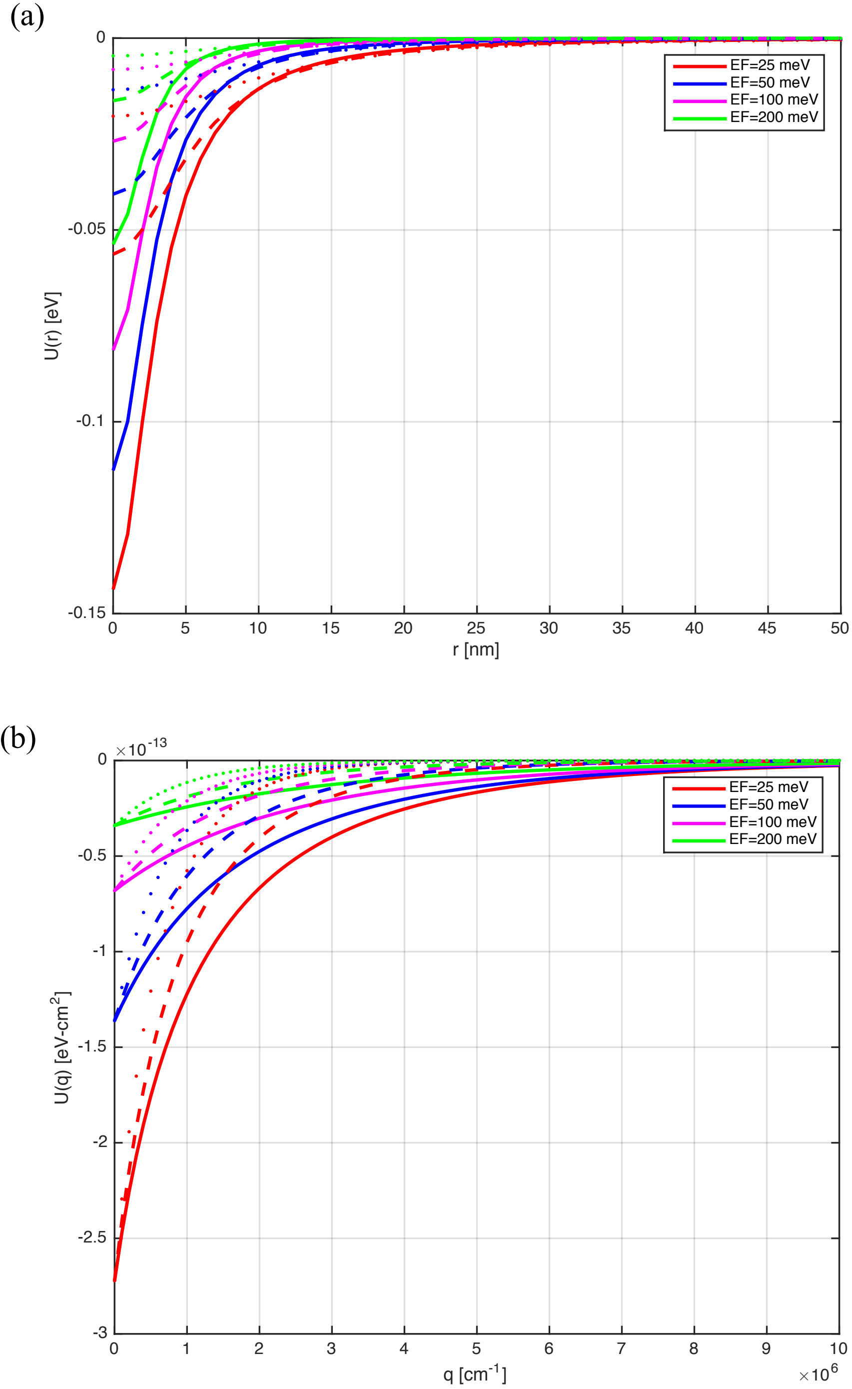

Fig. 2.15. Potential energy calculation using linear screening model. (a) $U(r)$ in real space. (b) $\widehat{U}(q)$ in Fourier space. Impurity distances are $z_0 = 2.5nm$ for solid lines, $z_0 = 5nm$ for dashed lines and $z_0 = 10nm$ for dash-dotted lines.

Please note Fig. 2.15 (b) and Fig. 2.11 are showing $\widehat{U}$ from different perspectives. In Fig. 2.11, $\widehat{U}$ depends on both k and θ. Since $q = 2ksin\frac{\theta}{2}$, $\widehat{U}$ only has one dependence q in Fig. 2.15 (b). Moreover, E_F is kept constant in Fig. 2.11, while there are four E_F values in Fig. 2.15 (b). The non-linear results in Fig. 2.14 are smaller compared to Fig. 2.15. Though the detailed data varies from point to point, we can see the non-linear effect (second term in 2.83) makes a large difference in potential energy calculation. In linear screening, $U(r)$ still varies rapidly for $z_0 = 2.5nm$ when $r \to 0$; while in non-linear screening, the slope of $U(r)$ become flat, i.e. $\frac{dU(r)}{dr} \to 0$. In linear screening, $U(r)$ reduce to zero much faster as r increasing. Another major difference is, $\widehat{U}(q)$ is independent of z_0 for $q = 0$ in linear screening (share same value); while non-linear model distinguish the different impurity distances for $q = 0$. In Chapter 3, the non-linear screening will be adopted for spin effect in graphene.

In Chapter 2, we reviewed basic electronic structure for graphene and paid special attention to its two transport phenomena: ballistic transport and diffusive transport. For diffusive transport, we study the Coulomb impurity scattering by deriving the momentum relaxation time directly and from the scattering cross section for linear Thomas Fermi screening. These two methods are demonstrated to be identical. We further considered the non-linear Thomas Fermi screening. Spin-orbit coupling in graphene will be covered in Chapter 3.

Chapter 3 Graphene Spintronics

3.1 Introduction to spintronics

In Chapter 2, we discussed that Dirac type carriers in graphene have pseudo-spin properties due to the A and B sublattices. Spin is an intrinsic form of angular momentum carried by elementary particles.[84] Spintronics, or spin electronics, study the electron spin behavior in solid state physics and utilize spin properties in addition to the charge degree of freedom to store and transfer information. Spin properties introduced and discussed in Chapter. 3 include spin transport, spin scattering and relaxation time, and spin injection and detection in graphene.

In recent years, spintronics has developed especially fast since the traditional CMOS technology has nearly reached the physical limits of silicon in the sub-10nm region. In addition, hard disk drive (HDD) companies are looking for alternative high density storage solutions. Spin phenomena have been demonstrated to be promising in both academic research and industrial products, for both storage and logic device applications. For example, the giant magnetoresistive (GMR) effect, recognized by the 2007 Nobel Prize in Physics, has been used widely in HDD read heads and biosensors. GMR devices consist of alternating ferromagnetic and nonmagnetic metal layers. Depending on the relative orientation of magnetization in the magnetic layers, the device resistance changes from small (parallel (P) magnetization) to large (antiparallel (AP) magnetization). This magnetoresistance (MR) enables detection of changes in the magnetic fields.[90][91] Components utilizing the GMR or tunneling magnetoresistive (TMR) effect are also called spin valve devices, which are the building blocks for spintronics and will be discussed in this Chapter.

It is also possible to perform logic operations using pure spin current, i.e. all spin logic (ASL), where magnetization is switched by spin current that exerts torque on the

magnet.[92] This phenomenon is also known as spin-transfer torque (STT), as shown in Fig. 3.1.

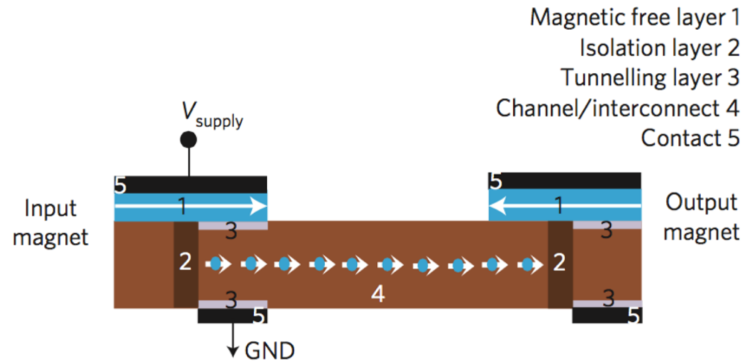

Fig. 3.1. The input logic bit controls the state of the corresponding output logic bit with the energy coming from an independent source, V_{supply}. In the ASL device, information is stored in the bistable states of magnets. Corresponding inputs and outputs communicate with each other via spin currents through a spin-coherent channel, and the state of the magnets is determined by the spin–torque phenomenon. [93]

Spin logics technology has the potential to achieve low power and high performance beyond CMOS due to its nonvolatility, which offers near zero static power and instant turning ON-OFF features.[92][94] The power consumption between spintronic and electronic devices can be compared in Table 3.1.

	Electronic switch	Spintronic switch
Barrier energy E_b	~20 k_BT	~60 k_BT
Mechanism	Individual	Collective
Switching energy (assuming 200 electrons)	~4000 k_BT $E = q\Delta V N_e \approx 4000 k_B T$	~60 – 80 k_BT $E = \frac{1}{2}\mu_0 \mu_B N_S H_K \approx 60 k_B T$
	Leakage determined by barrier	Leakage not related to barrier

Table 3.1. Power consumption for electronic and spintronic switch[95]

We note that the leakage in spintronic devices is not related to the barrier. ASL also use fewer gates compared to CMOS, i.e. higher density. The nonvolatility also make spintronics a good candidate for memory applications. Spin-transfer torque random-access memory (STT-RAM) has been investigated and may lead to, potential alternatives to

existing floating gates (FG) or Flash nonvolatile memory technologies in the future. STT-RAM uses spin-polarized currents, enabling smaller and less energy-consuming bits. [96][97][98]The cell structure of STT-RAM is shown in Fig. 3.2.

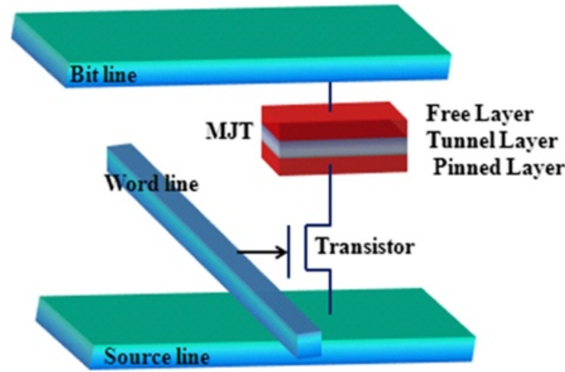

Fig. 3.2. Basic STT-RAM cell structure.[98]

A major challenge is developing a spin channel material whose properties can be tuned by electrostatic gates at room temperature with long spin lifetime and long-distance spin propagation. Graphene, as we discussed in Chapter 2, a monolayer carbon in 2D honeycomb structure, is a promising spin channel material for the following reasons. (1) Gate tunable spin transport at room temperatures. (2) Possible long spin diffusion length and spin relaxation time due to weak intrinsic spin-orbit and hyperfine interactions. (3) Dirac massless band structure leads to high carrier mobility. (4) Predictions of unusual gate-dependent magnetic and superconducting behavior in doped graphene. (5) Extreme surface sensitivity, which could be exploited for novel functionality including spin manipulation. (6) Compatible with silicon CMOS technology as well as a less expensive process after several years of intensive development in graphene manufacturing.[99] In this Chapter, we study topics of graphene spintronics as follows. In Section 3.2, intrinsic and extrinsic spin-orbit coupling are introduced. Rashba effect is studied in detail as an important extrinsic spin-orbit coupling mechanism for graphene.[100] The ionized impurity scattering explored in Chapter 2 needs to be adjusted since the Rashba effect lifts the spin degeneracy and the graphene Hamiltonian is no longer a simple 2x2 matrix. The spin relaxation time due to Rashba interaction is investigated in Section 3.2, also. Nonlinear screening model developed in Chapter 2.4 is adopted in calculations. Section 3.3 and 3.4 focus on spin injection into graphene, spin valve device modeling and magnetoresistance.

A local structure is introduced in Section 3.3 and non-local structure in Section 3.4. The local structure directly measures the standard two terminal resistance across two FM electrodes. Spin-polarized electrons are injected from one electrode, transported across the graphene, and detected by the second electrode. The difference in the resistance between the parallel and antiparallel magnetization alignments of the two electrodes is the local MR, which is the signal of spin transport.[99][101] Non-local spin transport in graphene at room temperature was first demonstrated in 2007.[16] It also arises from spin accumulation and is closely related to local structure. However, the non-local geometry benefits from higher signal-to-noise ratio, owing to the absence of net charge flow between injector and detector, as seen in Section 3.4.

3.2 Rashba spin interaction in graphene

The graphene linear energy dispersion $E_{\pm}(k) = \pm\hbar v_F k$ in Eq. 2.14 needs to be updated when relativistic effects such as spin-orbit coupling are included. For intrinsic spin-orbit coupling, i.e. the Dresselhaus term, λ_D, is very small since Carbon is a light atom. The intrinsic spin-orbit coupling Hamiltonian at K point can be written as

$$H_D = \frac{\lambda_D}{2}\sigma_z s_z \tag{3.1}$$

$\vec{\sigma}$ are Pauli matrixes for pseudo-spin discussed in Section 2.1. $\vec{s}$ are Pauli matrixes corresponding to the real spin. The new graphene Hamiltonian taking intrinsic spin-orbit coupling into account can be written as,

$$H = -i\hbar v_F \vec{\sigma}\cdot\nabla + \frac{\lambda_D}{2}\sigma_z s_z$$

$$= \begin{bmatrix} 0 & \hbar v_F(k_x - ik_y) & 0 & 0 \\ \hbar v_F(k_x + ik_y) & -\lambda_D & 0 & 0 \\ 0 & 0 & -\lambda_D & \hbar v_F(k_x - ik_y) \\ 0 & 0 & \hbar v_F(k_x + ik_y) & 0 \end{bmatrix} \tag{3.2}$$

Though Eq. 3.2 has a form of 4x4 Hamiltonian, it is equivalent to the solution of the following 2x2 Hamiltonian due to the symmetry,

$$H = \begin{bmatrix} 0 & \hbar v_F(k_x - ik_y) \\ \hbar v_F(k_x + ik_y) & -\lambda_D \end{bmatrix} \tag{3.3}$$

Diagonalizing the new Hamiltonian in Eq. 3.3 and the energy dispersion with intrinsic spin-orbit coupling can be written as

$$E_\pm(k) = -\frac{\lambda_D}{2} \pm \sqrt{\left(\frac{\lambda_D}{2}\right)^2 + (\hbar v_F k)^2} \tag{3.4}$$

As a result of $E_{gap} = E_+ - E_- = \lambda_D$, an energy band gap will be opened as shown in Fig. 3.3.

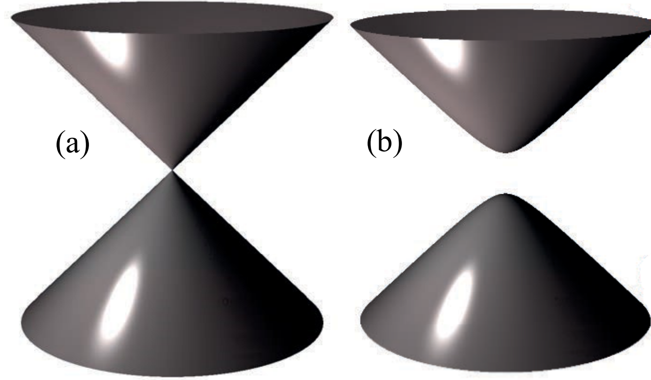

Fig. 3.3. Schematic for energy gap [99] (a) closes without, or (b) opens with, intrinsic spin-orbit coupling.

The mirror symmetry is still preserved when intrinsic spin-orbit coupling exists in graphene. In other words, only Dirac cones separate with finite gap, but the spin degeneracy is still preserved, which is a result of the 4x4 Hamiltonian in Eq. 3.2 simplified to Eq. 3.3.

However, for external spin-orbit interaction, the space symmetry of monolayer graphene is broken. For example, Rashba coupling will be induced in the presence of an electric field $\vec{\xi}$ perpendicular to the graphene plane. The Rashba spin-orbit interaction at K point can be shown to have the following Hamiltonian.

$$H_R = \frac{R}{2}(\vec{\sigma}\times\vec{s})_z = \frac{R}{2}\left(\sigma_x s_y - \sigma_y s_x\right) \tag{3.5}$$

In the model of Fig. 2.9, we need to consider the following two electric fields. First, out-of-plane point charges have a non-zero electric field component in the z-direction in the

graphene plane. This field is called $\xi_{imp}(r)$ and can cause a spatially varying Rashba spin-orbit interaction, $R_{imp}(r)$. In addition to the out-of-plane impurities, the uniform distribution of mobile charge carriers in the graphene also causes a perpendicular constant electric field, ξ_0, which induces a constant Rashba term R_0 as shown in Fig. 3.4. In some previous work[88][102] we did not consider R_0.

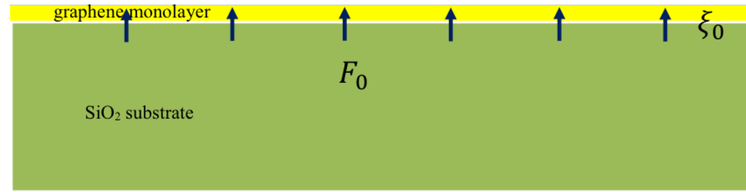

Fig. 3.4. Perpendicular electric field ξ_0 caused by the electron sheet in monolayer graphene. A constant Rashba term R_0 is raised due to ξ_0.

The R_0 and R_{imp} are calculated using the following expressions[103]

$$R_0 = \frac{LS}{3(sp\sigma)} e\xi_0 \tag{3.6a}$$

$$R_{imp}(r) = \frac{LS}{3(sp\sigma)} e\xi_{imp}(r) \tag{3.6b}$$

L is the length comparable to the size of the carbon atom, S is the strength of spin-orbit interaction and $sp\sigma$ are tight-binding model parameters. Following H. Min et.al.[103], we use $S = 0.06eV$, $sp\sigma = 5.58eV$ and $L = 1.86\times10^{-8}cm$. Similar to calculation in Chapter 2, we assume non-zero mobile equilibrium electron density in the graphene. Considering both H_D and H_R, the graphene Hamiltonian close to the K point becomes a 4x4 matrix and can be written as

$$H = -i\hbar v_F \vec{\sigma} \cdot \nabla + \frac{\lambda_D}{2} \sigma_z s_z + \frac{R_0}{2} (\vec{\sigma} \times \vec{s})_z$$

$$= \begin{bmatrix} 0 & \hbar v_F(k_x + ik_y) & 0 & 0 \\ \hbar v_F(k_x - ik_y) & -\lambda_D & -iR_0 & 0 \\ 0 & iR_0 & -\lambda_D & \hbar v_F(k_x + ik_y) \\ 0 & 0 & \hbar v_F(k_x - ik_y) & 0 \end{bmatrix} \quad (3.7)$$

The following four energy eigenvalues can be obtained by diagonalizing Eq. 3.7

$$E_{c\pm} = \left(\pm\frac{R_0}{2} - \frac{\lambda_D}{2}\right) + \sqrt{\left(\frac{R_0}{2} \mp \frac{\lambda_D}{2}\right)^2 + (\hbar v_F k)^2} \quad (3.8a)$$

$$E_{v\pm} = \left(\pm\frac{R_0}{2} - \frac{\lambda_D}{2}\right) - \sqrt{\left(\frac{\lambda_D}{2} \mp \frac{R_0}{2}\right)^2 + (\hbar v_F k)^2} \quad (3.8b)$$

$c \pm / v \pm$ correspond to two non-degenerate conduction/valence bands. According to Eq. 3.6, Rashba effect is proportional to the perpendicular electrical field. As the perpendicular electric field increases, the comparison of intrinsic and Rashba spin-orbit coupling are plotted in Fig. 3.5.

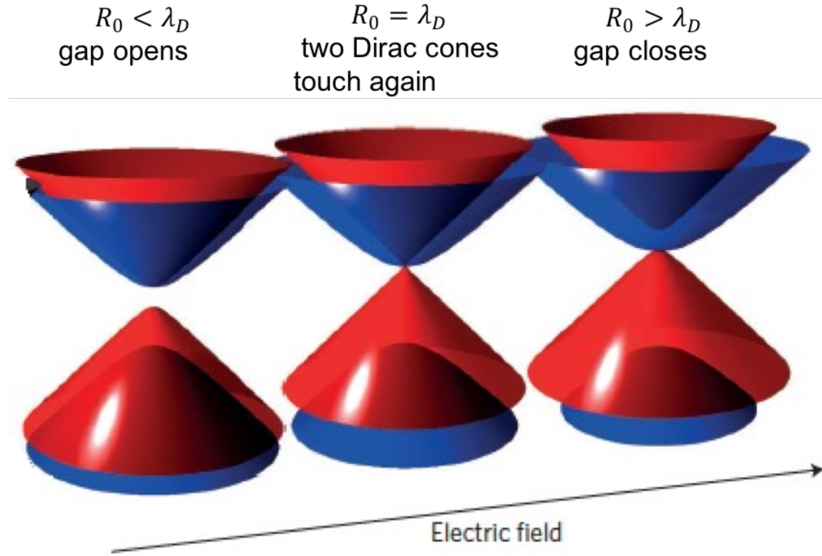

Fig.3.5. Band gap due to of intrinsic and Rashba spin-orbit coupling for different perpendicular electric field strength.[99]

Initially perpendicular electric field is very small, $R_0 < \lambda_D$, the Dirac cones open. As electric field increases, the Rashba effect becomes larger. When $R_0 = \lambda_D$, the Dirac cones touch again. The energy gap closes if the perpendicular electric field continues to increase

and $R_0 > \lambda_D$. Since the intrinsic spin-orbit coupling is very small, our calculation lies well in the $R_0 > \lambda_D$ region. Ignoring the small Dresselhaus term λ_D, Eq. 3.8 can be simplified along with the corresponding eigenstate wave functions shown in Eq. 3.9

$$E_{c\pm} = \pm\frac{R_0}{2} + \sqrt{\left(\frac{R_0}{2}\right)^2 + (\hbar v_F k)^2}, \langle\vec{r}|c\pm,\vec{k}\rangle = \begin{pmatrix} 1 \\ b_{c\pm}e^{i\theta_{\vec{k}}} \\ \pm i b_{c\pm}e^{i\theta_{\vec{k}}} \\ \pm i e^{2i\theta_{\vec{k}}} \end{pmatrix} \frac{e^{i\vec{k}\cdot\vec{r}}}{\sqrt{2}\cdot\sqrt{1+{b_{c\pm}}^2}} \quad (3.9a)$$

$$E_{v\pm} = \pm\frac{R_0}{2} - \sqrt{\left(\frac{R_0}{2}\right)^2 + (\hbar v_F k)^2}, \langle\vec{r}|v\pm,\vec{k}\rangle = \begin{pmatrix} 1 \\ b_{v\pm}e^{i\theta_{\vec{k}}} \\ \pm i b_{v\pm}e^{i\theta_{\vec{k}}} \\ \pm i e^{2i\theta_{\vec{k}}} \end{pmatrix} \frac{e^{i\vec{k}\cdot\vec{r}}}{\sqrt{2}\cdot\sqrt{1+{b_{v\pm}}^2}} \quad (3.9b)$$

$b_{c\pm} = \frac{E_{c\pm}}{\hbar v_F k}$ and $b_{v\pm} = \frac{E_{v\pm}}{\hbar v_F k}$. Due to the existence of R_0, the spin degeneracy is lifted. The Rashba interaction couples the graphene pseudo-spin $\vec{\sigma}$ and the true spin $\vec{s}$ of the electrons (or holes). Hence, the relevant charge carrier states are not spin-eigenstates.[104][105] The schematic for the four bands are plotted in Fig. 3.6, which corresponds to $R_0 > \lambda_D$ case in Fig. 3.5.

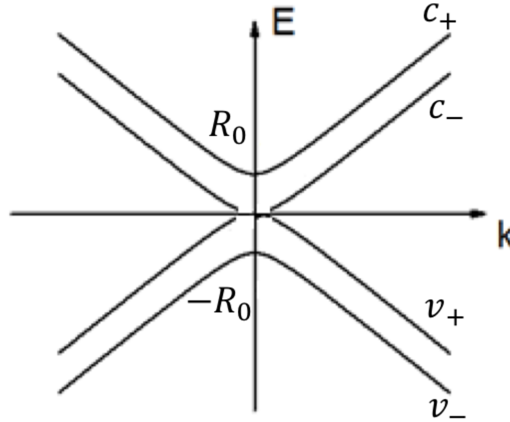

Fig. 3.6. Band diagram for Eq. 3.9. As result of Rashba effect, bands are split without a gap.

Again assuming the graphene is n-type and charge carriers are electrons, there are the two non-degenerate conduction bands due to the external Rashba spin-orbit coupling. Hence, the scattering process discussed in Chapter 2 needs to be modified. For ionized impurity scattering due to the screened Coulomb potential, now the scattering is elastic but no longer

limited to one band with one differential cross-section $\frac{d\sigma}{d\theta}$. In another word, both intra-band (c$\pm$ to c$\pm$) and inter-band (c$\pm$ to c$\mp$) scattering processes should be taken into consideration as a result of Rashba effect induced band splitting. The schematics for intra-band and inter-band scattering processes are plotted in the following Fig. 3.7.

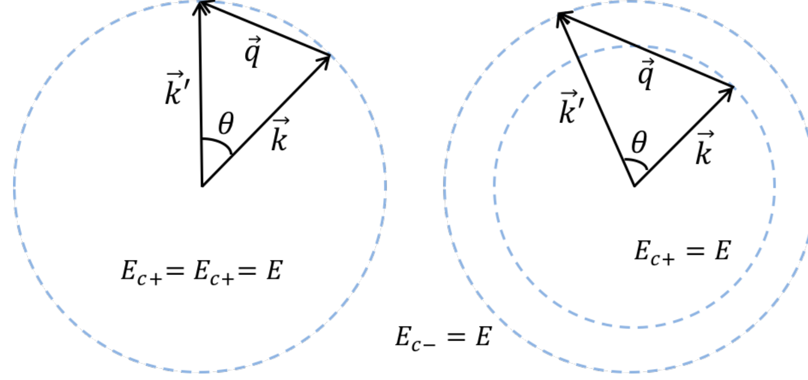

Fig. 3.7. Scattering process for intra-band scattering (c+ to c+, left) and inter-band scattering (c+ to c−, right). The scattering occurs at constant energy surface E, i.e. elastic scattering.

In addition to the intra-band and inter-band scattering process within ionized impurity scattering due to the Coulomb potential, there is another scattering mechanism called Rashba spin scattering. We will discuss the Rashba spin scattering later in this section.

Same as the parameters used in Section 2.4, four different Fermi energies are being considered: $25meV, 50meV, 100meV$, and $200meV$, corresponding to electron sheet densities of $4.59\times10^{10}cm^{-2}$, $1.84\times10^{11}cm^{-2}, 7.35\times10^{11}cm^{-2}$ and $2.94\times10^{12}cm^{-2}$. Similar to the one band differential scattering cross-section in Eq. 2.64, the intra-band (denoted as $\frac{d\sigma_{Ua}}{d\theta}$) and inter-band (denoted as $\frac{d\sigma_{Ub}}{d\theta}$) differential scattering cross-section can be written as

$$\frac{d\sigma_{Ua}}{d\theta}(\theta, E) = \frac{1}{2\pi}\frac{E}{\hbar^3 v_F{}^3}\frac{\hat{U}^2(q)}{\left(1 + b_{c+}{}^2\right)^2} \tag{3.10a}$$

$$\times\left[cos^4\frac{\theta}{2}\left(1 + b_{c+}{}^2\right)^2 - \frac{1}{2}sin^2\theta\left(1 - b_{c+}{}^4\right) + sin^4\frac{\theta}{2}\left(1 - b_{c+}{}^2\right)^2\right]$$

$$\frac{d\sigma_{Ub}}{d\theta}(\theta, E) = \frac{1}{2\pi}\frac{E}{\hbar^3 v_F{}^3}\frac{\hat{U}^2(q)}{\left(1 + b_{c-}{}^2\right)\left(1 + b_{c+}{}^2\right)}sin^2\theta \tag{3.10b}$$

The detailed derivation through the scattering matrix can be found in Appendix. B. It can be shown that Eq. 3.10 reduces to Eq. 2.64 without Rashba term R_0. It is worth mentioning that our discussion of scattering uses an intra/inter band language instead of spin up/down, because pure spin states are not eigenstates of the Hamiltonian in Eq. 3.9. Scattering cross-sections are still calculated for $E = E_F$, wave vector $\vec{k}$, $\vec{k}'$ and transfer vector $\vec{q}$ are adjusted as follows for the new inter-band scattering processes in Fig. 3.7. For intra-band scattering (c+ to c+), $k = k' = \frac{\sqrt{E^2 - ER_0}}{\hbar v_F}$, $q = 2ksin\left(\frac{\theta}{2}\right)$ still holds, while for inter-band scattering, $k = \frac{\sqrt{E^2 - ER_0}}{\hbar v_F}$, $k' = \frac{\sqrt{E^2 + ER_0}}{\hbar v_F}$, $q = \sqrt{k^2 + k'^2 - 2kk'cos\theta}$ can be found using the law of cosines. $\widehat{U}(q)$ is the screened potential energy in Fourier space. Applying the $\widehat{U}(q)$ calculated using nonlinear screening from Section. 2.4 into Eq. 3.10, the differential cross-sections $\frac{d\sigma_{Ua}}{d\theta}$ and $\frac{d\sigma_{Ub}}{d\theta}$ are plotted in Fig. 3.8.

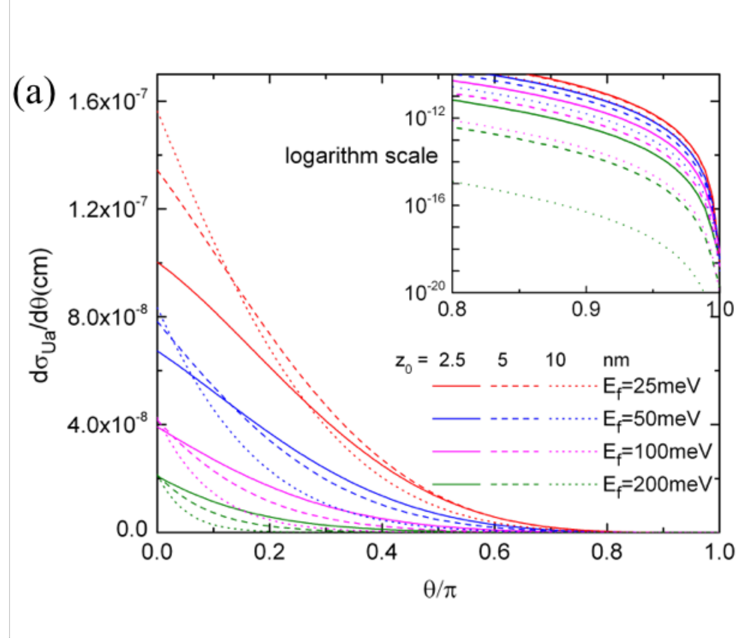

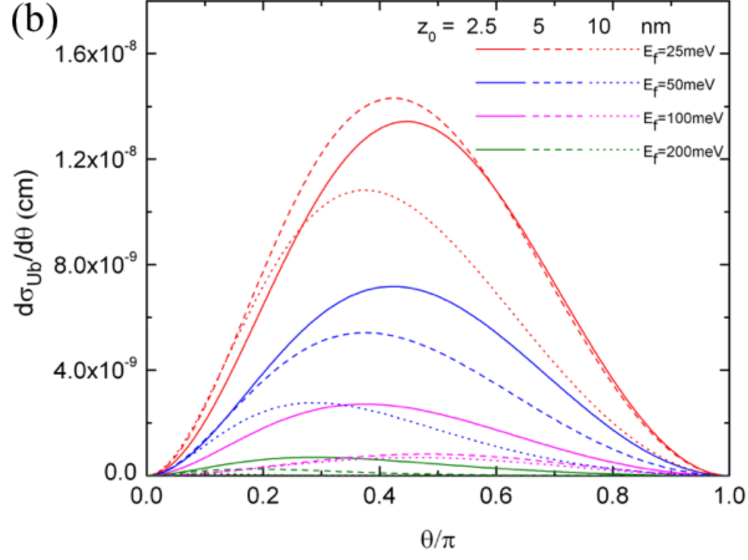

Fig. 3.8. Differential scattering cross-section for (a) intra-band and (b) inter-band ionized impurity scattering. The electron energy is equal to the Fermi energy, and impurity distance are $z_0 = 2.5nm$ (solid), $z_0 = 5nm$ (dashed) and $z_0 = 10nm$ (dotted).

For the same E_F and z_0, on average $\frac{d\sigma_{Ub}}{d\theta}$ is about one order of magnitude smaller than $\frac{d\sigma_{Ua}}{d\theta}$. Inter-band forward scattering ($\theta = 0$) and back scattering ($\theta = \pi$) are both strictly suppressed. Intra-band back scattering is not strictly forbidden, but it is small. The initial and final states for intra-band back scattering are not orthogonal, as shown in the following

$$\langle c+, \vec{k} | c+, -\vec{k} \rangle = \begin{pmatrix} 1 & \frac{E_{c+}}{\hbar v_F k} e^{-i\theta_{\vec{k}}} & -i\frac{E_{c+}}{\hbar v_F k} e^{-i\theta_{\vec{k}}} & -ie^{-2i\theta_{\vec{k}}} \end{pmatrix} \begin{pmatrix} 1 \\ -\frac{E_{c+}}{\hbar v_F k} e^{i\theta_{\vec{k}}} \\ -i\frac{E_{c+}}{\hbar v_F k} e^{i\theta_{\vec{k}}} \\ ie^{2i\theta_{\vec{k}}} \end{pmatrix}$$

$$= 2 - 2\left(\frac{E_{c+}}{\hbar v_F k}\right) \neq 0 \tag{3.11}$$

For back scattering, the final state $\vec{k}' = -\vec{k}$ in Eq. 3.11. If Rashba term $R_0 = 0$, i.e. no Rashba effect, $\langle c+, \vec{k} | c+, -\vec{k} \rangle = 0$, and back scattering for intra-band scattering process would be strictly suppressed. However, using Eq. 3.6a,

$$R_0 = \frac{l\xi}{3(sp\sigma)}\left[\frac{4\pi e^2}{\kappa}\left(\frac{1}{2}aE_F{}^2\right)\right] \tag{3.12}$$

R_0 is in the range $7.1\times10^{-5}\ to\ 4.5\times10^{-3}\ meV$, depending on E_F (or electron density), i.e. nearly two orders of magnitude smaller than E_F. Hence, back scattering $\frac{d\sigma_{Ua}}{d\theta}(\theta = \pi)$ is nearly zero. $\frac{d\sigma_{Ua}}{d\theta}(\theta = \pi) \approx 10^{-11}\ \frac{d\sigma_{Ua}}{d\theta}(\theta = 0)$. Furthermore, we see that increased z_0 can result in larger differential scattering cross-sections for certain scattering angles. This is possible because $\left|\widehat{U}(q)\right|_{z_0=2.5nm} < \left|\widehat{U}(q)\right|_{z_0=5nm} < \left|\widehat{U}(q)\right|_{z_0=10nm}$ for small q, as seen in Fig. 2.14 (b) in Section 2.4. By integrating over scattering angle θ using Eq. 2.68, the total scattering cross-section for intra/inter band ionized impurity scattering can be plotted in Fig. 3.9.

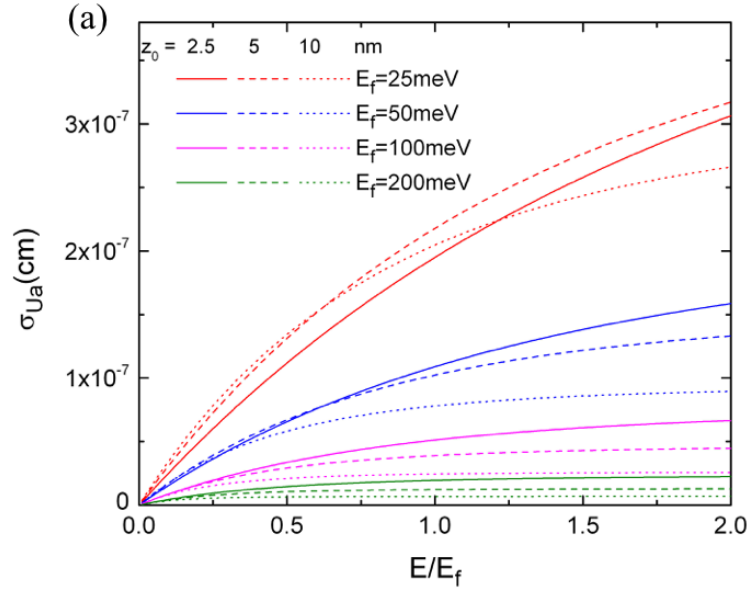

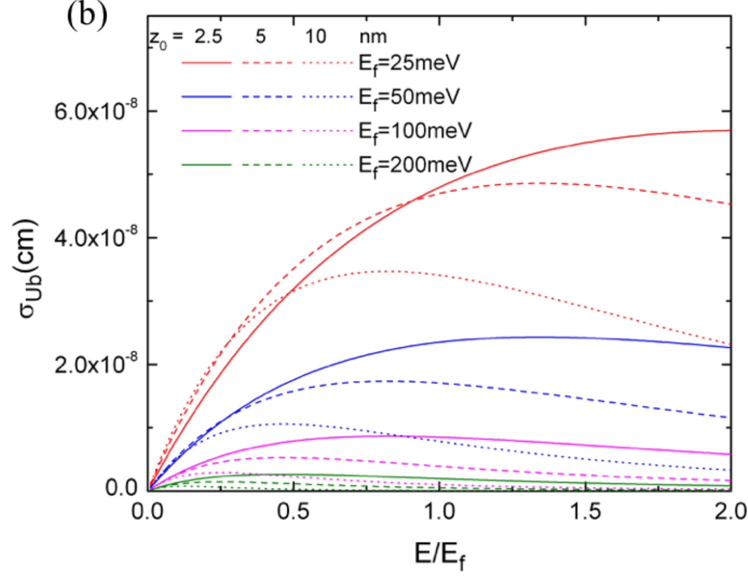

Fig. 3.9. Total ionized impurity scattering cross-section for (a) intra-band and (b) inter-band scattering. The electron energy varies from R_0 to E_F. Impurity distance are $z_0 = 2.5nm$ (solid), $z_0 = 5nm$ (dashed) and $z_0 = 10nm$ (dotted).

As our interest focuses primarily on electrons near the Fermi energy, the energy scale is normalized in Fig.3.9. Evidently, smaller electron density leads to larger scattering cross-sections because screening is weaker. The total scattering cross-section does not always vary monotonically. It may saturate or even decrease for energies greater than approximately $0.5 \sim 1.5E_F$. Revisiting Chapter 2.3, the momentum relaxation time τ_m and mobility μ can then be estimated using Eq. 2.67 and Eq. 2.70. Based on the same E_F and z_0 used above, ionized impurity scattering yields an average $\tau_m \approx 0.01ns$ and $\mu \approx 10^6 cm^2 s^{-1} V^{-1}$, which is large compared to the experimental mobilities measured at low temperature for graphene on SiO_2 substrates[7][106], but it is within range of what has been observed for graphene on other substrates or suspended layers.[107] The mobility does not change much compared to the calculation in Chapter.2, and one finds Rashba spin-orbit coupling is a weak effect.

In additional to the band splitting leading to intra-band and inter-band scattering processes for ionized impurity scattering, Rashba effect yields a second, independent scattering mechanism called Rashba spin scattering. It is spatially dependent and thus

written as $R_{imp}(r)$. Rashba spin scattering is a different scattering process than ionized impurity scattering. According to Eq. 3.6b, $R_{imp}(r)$ depends on the perpendicular component of the electric field $\xi_{imp}(r)$, which can be expressed as

$$e\xi_{imp}(r) = -\frac{e^2}{\kappa}\left[\frac{z_0}{(r^2 + {z_0}^2)^{\frac{3}{2}}}\right] \tag{3.13}$$

$\xi_{imp}(r)$ is solely the result of the impurity charge because the induced charge density in the graphene surface does not contribute to it. However, the induced charge density does contribute to the Coulomb potential, $U(r)$. Therefore, the expressions for ionized impurity scattering and Rashba spin scattering are quite different. Based on the scattering matrix $\langle c+, \vec{k}|\hat{R}_{imp}(q)|c+, \vec{k}'\rangle$ and $\langle c+, \vec{k}|\hat{R}_{imp}(q)|c-, \vec{k}'\rangle$, differential intra and inter-band scattering cross-sections for Rashba scattering are derived in Appendix B and given by,

$$\frac{d\sigma_{Ra}}{d\theta}(\theta, E) = \frac{1}{8\pi}\frac{E}{\hbar^3 {v_F}^3}\left[\frac{{b_{c+}}^2}{1 + {b_{c+}}^2}\hat{R}_{imp}(q)\right]^2 \tag{3.14a}$$

$$\frac{d\sigma_{Rb}}{d\theta}(\theta, E) = 0 \tag{3.14b}$$

$\frac{d\sigma_{Ra}}{d\theta}$ denotes intra-band (c+ to c+) scattering and there is no inter-band (c+ to c−) scattering, $\frac{d\sigma_{Rb}}{d\theta}$, for the Rashba scattering process. $\hat{R}_{imp}(q)$ is the two-dimensional Fourier transform of $R_{imp}(r)$. Because there is a simple analytic expression for the electric field in Eq. 3.13, we may write $\hat{R}_{imp}(q)$ as

$$\hat{R}_{imp}(q) = \frac{l\xi}{3(sp\sigma)}\left(-\frac{e^2}{\kappa}\right)\int d^2r e^{-i\vec{q}\cdot\vec{r}}\frac{z_0}{(r^2 + {z_0}^2)^{\frac{3}{2}}} = -\frac{2\pi e^2 l\xi}{3\kappa(sp\sigma)}e^{-qz_0} \tag{3.15}$$

This expression also indicates the normalization used for the Fourier transform and implies that the scattering cross-sections in this planar geometry are lengths. Inserting Eq. 3.15 into equation Eq. 3.14a, an analytic expression for $\frac{d\sigma_{Ra}}{d\theta}(\theta, E)$ can be obtained. Subsequently we can calculate and display $\frac{d\sigma_{Ra}}{d\theta}$ and σ_{Ra} in Fig. 3.10 for different Fermi energies and impurity distances.

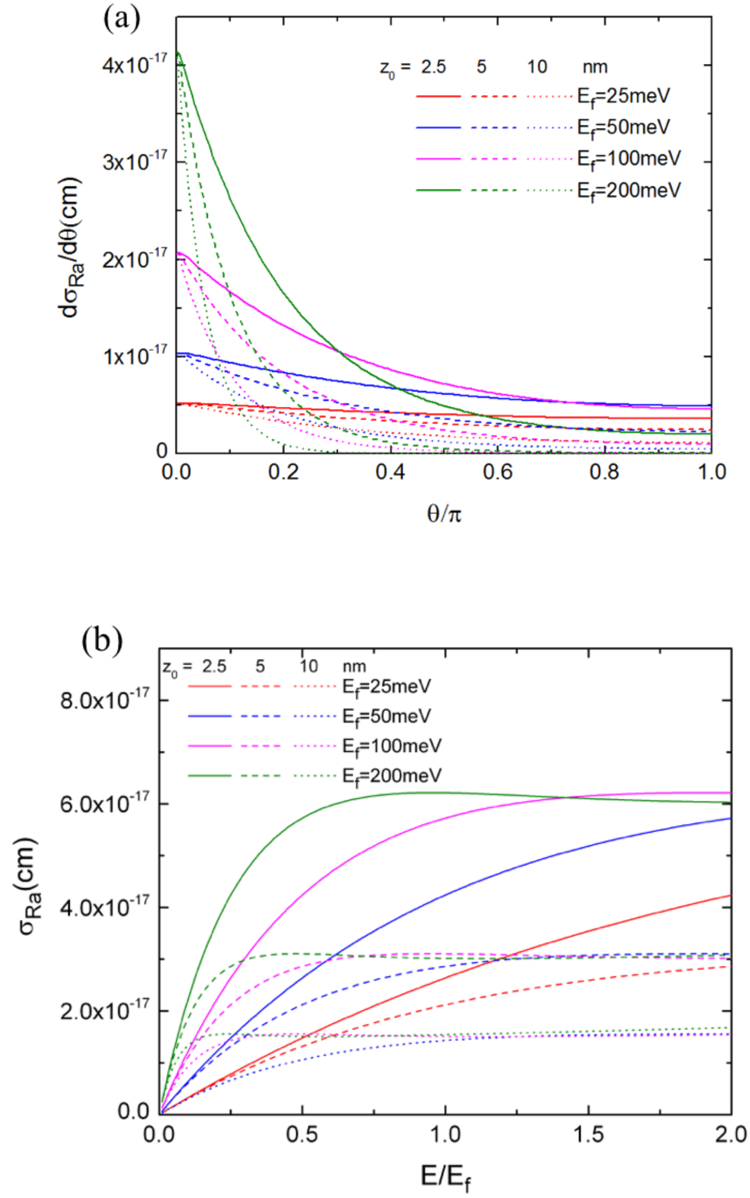

Fig. 3.10. (a) Differential and (b) Total scattering cross-section for intra-band Rashba spin scattering. Inter-band scattering does not exist.

Evidently, a larger electron density (larger E_F) yields a larger $\frac{d\sigma_{Ra}}{d\theta}$ at small θ for given z_0. Also, for a given E_F, $\frac{d\sigma_{Ra}}{d\theta}$ decreases monotonically with increasing z_0. These properties are different from those obtained for ionized impurity scattering. Furthermore, $\frac{d\sigma_{Ra}}{d\theta} \neq 0$

for $\theta = \pi$, i.e. back scattering is allowed for Rashba spin scattering. All $\frac{d\sigma_{Ra}}{d\theta}$ for the same E_F share the same value for $\theta = 0$, i.e. forward scattering is independent of z_0. For a given impurity charge and location, Rashba scattering is much weaker than ionized impurity scattering. As stated in Eq. 3.14b, the inter-band Rashba scattering $\frac{d\sigma_{Rb}}{d\theta}$ is always forbidden due to the symmetry of the states. The accuracy of the above calculations is examined with the aid of the optical theorem, as outlined in Appendix C.

Because even the unperturbed states of Eq. 3.9 are not spin eigenstates, all scattering processes also contribute to spin relaxation. It should be remarked, however, that due to the weakness of R_0, diagonalizing H in Eq. 3.7 and then treating the relatively strong impurity scattering as a perturbation is not likely to yield reliable results for spin relaxation. The Rashba interaction associated with a charged impurity is the most effective spin scattering mechanism considered here because it directly couples to the electron spin. Based only on the Rashba scattering process, a spin relaxation time,τ_s, of approximately $2ms$ can be estimated using Eq. 2.67 and the results above, assuming $n_{imp} = 10^{11}cm^{-2}$. This relaxation time is considerably larger than the reported experimental data, which is not surprising.[99][108] Other related mechanisms, particularly in the case of adatom impurities, may have a stronger impact on spin relaxation.[109] Examples such as Elliott–Yafet and Dyakonov–Perel spin relaxation mechanisms are shown in Fig. 3.11

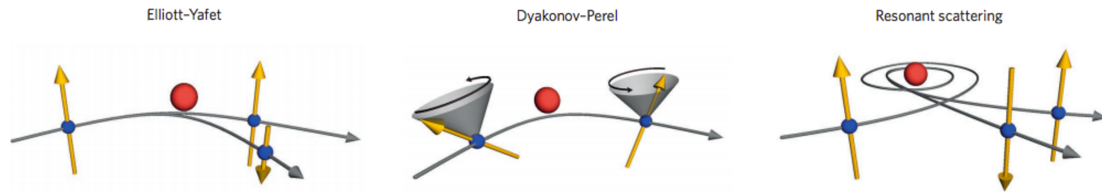

Fig. 3.11. Spin relaxation mechanisms in graphene.[99] An illustrative figure of three possible spin relaxation mechanisms for graphene: Elliott–Yafet, Dyakonov–Perel and resonant scattering by local magnetic moments. The blue dots indicate the electrons/holes with yellow arrows as their spin orientation. The red dots represent the scattering centers. Grey cones with circular arrows represent the spin precession.

After studying Rashba effect as one of spin-orbit coupling in graphene, next we focus on the modeling of spin injection into graphene and spin valve device modeling. To

calculate and characterize the spin injection into the spin channel material (graphene), "local" and "non-local" models are introduced in Section. 3.3 and Section 3.4.

3.3 Spin valve device, local model

So far we have learnt that graphene is a promising material due to high charge-carrier mobility and gate-tunable carrier density. Furthermore, as a result of the small intrinsic spin-orbit interaction and low hyperfine interaction, spin-polarized injected charge carriers are expected to maintain their polarization over relatively long times and combined with the high carrier velocities, over long distances. In the following Sections 3.3 and 3.4, we present a device model for graphene based spin valves. Applying a semi-classical drift-diffusion approach, a one-dimensional model that properly describes the electronic and the spintronic transport properties, including electrostatics (ESs), charge and spin injection, and spin-current profiles is developed. Spin relaxation, bias-dependent magnetoresistance (MR) will also be discussed. The goals for the following two sections are not only to explore the device physics, but also to provide a possible basis for modeling spintronic graphene circuit modules.[93][110]

A schematic cross section of a typical graphene spin valve is shown in Fig. 3.12.[101] A nonlocal four terminal structure has been widely employed for enhanced spin injection[16][111][112][113][114][115][116][117]. The four contacts 1, 2, 3, and 4 are all made of ferromagnetic (FM) metals. Below the contacts is a tunnel barrier layer (on the order of 1 nm) composed of an insulating material, such as Al_2O_3, to enable efficient spin injection.[118][119] The graphene layer is beneath the tunnel barrier, followed by SiO_2 and Si layer at the bottom providing gate control. A current source is applied between contacts 3 and 4, injecting and extracting both charge and spin carriers. The charge current conducts in one direction (3 to 4), while the spin current can flow in both directions (3 to 4 and 3 to

2). Detection of spin injection is realized by measuring the MR difference between terminals 1 and 2 in parallel (P) and antiparallel (AP) configurations.

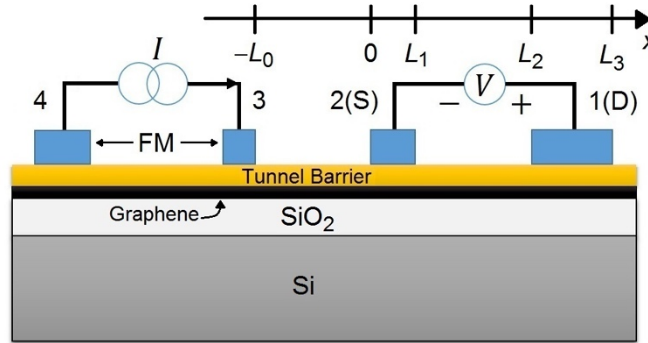

Fig. 3.12. Schematic cross-section of a typical graphene-based spin valve device.

In this section, we first consider a simple local structure, which involves only two contacts, 1 and 2, and the region between them ($0 \leq x \leq L_3$ in Fig. 3.12). The local structure is similar to a graphene FET in Fig. 2.5, except for the tunnel barrier between the graphene channel and the charge injection/collection contacts. It is therefore convenient to use the conventional transistor terminology by defining contact 2 as the source (S) and contact 1 as the drain (D). For simplicity, we assume that the same definition holds for both electron and hole cases. The Si contact at the bottom constitutes the gate (G) electrode, i.e. once again the back-gated structure. It is worth noting that the resistance changes in local and nonlocal geometries both arise from spin accumulation and are closely related fundamentally, but the non-local structure benefits from higher signal-to-noise ratio, owing to the absence of net charge flow between injector and detector. After a discussion of the local device, we introduce the nonlocal device as well as bias-dependent MR for both devices in Section 3.4.

A local device includes regions from $x = 0$ to $x = L_3$. We assume the device is homogeneous in the direction perpendicular to the cross section. Because of the potential drop in graphene, the quantum capacitance effect needs to be considered following previous discussion in Section 2.1.[120] Additionally, two more concepts related with the Fermi energy E_F need to be considered due to spin injection and transport : 1) the Galvani potential ES; 2) the electrochemical potential EC.[121] The ES potential in graphene is defined as the energy per electron at the Dirac point. The EC potential in graphene is

defined as the energy per electron at the Fermi level. Under different bias conditions, it may be above or below the Dirac point, and it may be spin dependent. We have E_F as the difference between EC and ES, i.e., $E_F = EC - ES$. For S, D, and G contacts, we assumed infinite DOSs and $EC = ES$. The voltage (EC per unit charge) difference between D and S is V_{DS}. The voltage difference between G and S (D) is V_{GS} (V_{GD}). When V_{GS} is positive (negative), the Fermi level in graphene beneath the contact S is above (below) the Dirac point and locally the channel is in the electron (hole) conduction regime.

Due to the low DOS near the Dirac point, the graphene layer may not completely screen the electric field induced by the charge at the gate. We introduce a screening efficiency α. For example, in the electron conduction regime, α is defined as

$$\alpha = \frac{en}{C_S\left(V_G - V_{gph}\right)} \tag{3.16}$$

Again e is the electron charge, n is the electron density in graphene. C_S is the capacitance of the SiO_2 dielectric per unit area, V_G is the EC or ES potential at the gate, and V_{gph} is the ES potential in graphene.

Under the contacts, when there is no current injection, the EC in graphene is the same as that in the FM contact (i.e., $E_F = eV_{gph}$, Eq. 3.16 then become similar to Eq. 2.23). Taking the S contact as an example, when positive charge accumulates at the SiO_2/Si interface, negative charge accumulates both in the graphene and at the FM contact/tunnel barrier interface. One-dimensional electrostatics then yields the following equation,

$$eV_{GS} = E_F\left(1 + \frac{C_T}{C_S}\right) + \frac{e^2 n}{C_S} \tag{3.17}$$

C_T is the capacitance of the tunnel barrier per unit area. The two terms on the right-hand side correspond to contributions of the two negative sheet charges. When E_F is much greater than the thermal energy $k_B T$, the electron density in graphene can be expressed using Eq. 2.21,[69]

$$n \approx a\left[\frac{1}{2}{E_F}^2 + \frac{1}{6}(\pi k_B T)^2\right] \tag{3.18}$$

Combing Eq. 3.16- 3.18, the screening efficiency α can be re-written as

$$\alpha = \left[1 + \frac{1}{AE_F}\frac{C_T}{C_S}\left(1 + \frac{1}{6{E_F}^2}(\pi k_B T)^2\right)^{-1}\right]^{-1} \tag{3.19}$$

With factor $A = \frac{ae^2}{2C_S}$, the Fermi energy E_F can thus be written as

$$E_F = \frac{1}{A}\left(1 + \frac{C_T}{C_S}\right)\left[\sqrt{\frac{1}{4} + \frac{AeV_{GS} - \frac{(A\pi k_B T)^2}{3}}{\left(1 + \frac{C_T}{C_S}\right)^2}} - \frac{1}{2}\right] \tag{3.20}$$

In a graphene spin valve, the thickness of the tunnel barrier is $\sim 1nm$, while the lateral dimension of the device along the x direction is on the order of micrometers. Therefore, it is a reasonable approximation to assume α to be constant within each region for S ($0 \le x \le L_1$), D ($L_2 \le x \le L_3$), and the channel ($L_1 \le x \le L_2$). In our calculation, we set $C_T = 8 \times 10^{-6} Fcm^{-2}$ and $C_S = 3.5 \times 10^{-8} Fcm^{-2}$, corresponding to a $1nm$ Al_2O_3 thin layer and a $100nm$ SiO_2 substrate. Then, the screening efficiency α is ~0.1 for both S and D regions. The channel region without a contact on the top corresponds to $C_T \to 0$ in Eq. 3.19 and Eq. 3.20, resulting in $\alpha \sim 1$. At $x = L_1$ and $x = L_2$, the transition of α from ~0.1 to ~ 1 takes place within the length scale of a few nanometers. Compared with the lateral dimension of the device, it is reasonable to assume an abrupt transition in the model. The conductivity of graphene at a high carrier density can be written as[43]

$$\sigma = \frac{1}{2} e^2 {v_F}^2 g(E_F) \tau_m(E_F) \tag{3.21}$$

Where again $g(E_F)$ is the DOS in graphene and $\tau_m(E_F)$ is the momentum relaxation time, both at the Fermi level. Assuming the device to be operating near zero temperature, impurity scattering is the dominant mechanism.

When S and D are FM contacts, spin-polarized carriers are injected into the graphene channel. The parameters E_F ,n, and the current J all have two components, labeled by the two spin states up, $\uparrow$, and down, $\downarrow$. For example, $n_\uparrow$ ($n_\downarrow$) stands for the electron density with spin up (down) and the total electron density $n = n_\uparrow + n_\downarrow$. The direction of the spin is normal to the cross section in Fig.3.12 (easy axis of the FM contacts). We assume low injection and electron conduction regime (quasi-equilibrium) so that the electron densities are not far from their equilibrium values. The electron-hole

recombination can be neglected in this unipolar case. In the framework of the gradual channel approximation, the spin dependent currents ($J_\uparrow, J_\downarrow$) and carrier densities ($n_\uparrow, n_\downarrow$) can be expressed as

$$J_{\uparrow,\downarrow} = -\kappa E_{F\uparrow,\downarrow}^{2} \frac{d}{dx}\left(E_{F\uparrow,\downarrow} - eV_{gph}\right) \tag{3.22a}$$

$$n_{\uparrow,\downarrow} = a\left[\frac{1}{4}E_{F\uparrow,\downarrow}^{2} + \frac{1}{12}(\pi k_B T)^2\right] \tag{3.22b}$$

where κ is a proportionality factor, for which we use $7.3\times10^{16} eV^{-2}V^{-1}s^{-1}$ in the calculation, which is equivalent to a field-effect mobility of $2000 cm^2V^{-1}s^{-1}$ for a carrier concentration $n = 4.3\times10^{12} cm^{-2}$. The total charge current and spin current are defined as

$$J = J_\uparrow + J_\downarrow \tag{3.23a}$$

$$J_S = J_\uparrow - J_\downarrow \tag{3.23b}$$

Eq. 3.16 can be rearranged as

$$V_G - V_{gph} = \frac{e(n_\uparrow + n_\downarrow)}{\alpha C_S} \tag{3.24}$$

Combining Eq. 3.22- Eq. 3.24, the current can be expressed as functions of $E_{F\uparrow,\downarrow}$. The negative sign in Eq. 3.22a indicates that the current is positive when it flows in the $-x$ direction ($V_{DS} > 0$). A spin relaxation process, which tends to reduce the net spin of the system, can occur in graphene. Physical mechanisms involve the spin–orbit interaction in combination with spatial fluctuations due to impurities, boundaries, or phonons.[87][103][122] For the device modeling, we characterize spin relaxation by a single parameter, again the spin relaxation time constant, τ_S. The spin relaxation terms are, therefore, written as $\frac{(n_\uparrow - n_\downarrow)}{\tau_S}$.[123][124] In a steady state, the continuity of each spin current component for graphene in the channel region requires

$$\frac{1}{e}\frac{dJ_{\uparrow,\downarrow}}{dx} - \frac{n_{\uparrow,\downarrow} - n_{\downarrow,\uparrow}}{\tau_S} = 0 \quad L_1 \le x \le L_2 \tag{3.25}$$

The tunneling current at the contact can be expressed, following the approach of Bardeen[125], Tersoff and Hamann[126]. As the voltage for spin detection is typically small (V_{DS} ~ 10 mV), a linear approximation is valid. The tunneling rate is then proportional to the EC difference across the barrier, and the DOS at the local (quasi-)Fermi level E_F of

graphene. (The DOS in the FM metal is much greater; hence, the tunneling is mostly limited by the DOS of the graphene.) The contact injection/extraction terms can be written as

$$G_{S\uparrow,\downarrow} = g_{S\uparrow,\downarrow}\left|E_{F\uparrow,\downarrow}\right|\left(eV_{GS} - E_{F\uparrow,\downarrow} - e^2\frac{n_\uparrow + n_\downarrow}{\alpha_S C_S}\right) \quad 0 \le x \le L_1 \qquad (3.26a)$$

$$G_{D\uparrow,\downarrow} = g_{D\uparrow,\downarrow}\left|E_{F\uparrow,\downarrow}\right|\left(eV_{GD} - E_{F\uparrow,\downarrow} - e^2\frac{n_\uparrow + n_\downarrow}{\alpha_D C_S}\right) \quad L_2 \le x \le L_3 \qquad (3.26b)$$

where g is a spin-dependent proportionality factor determined by the specific properties of the FM and the tunnel barrier. The current continuity equation for the contact regions can be written as

$$\frac{1}{e}\frac{dJ_{\uparrow,\downarrow}}{dx} - \frac{n_{\uparrow,\downarrow} - n_{\downarrow,\uparrow}}{\tau_S} + G_{S\uparrow,\downarrow} = 0 \quad 0 \le x \le L_1 \qquad (3.27a)$$

$$\frac{1}{e}\frac{dJ_{\uparrow,\downarrow}}{dx} - \frac{n_{\uparrow,\downarrow} - n_{\downarrow,\uparrow}}{\tau_S} + G_{D\uparrow,\downarrow} = 0 \quad L_2 \le x \le L_3 \qquad (3.27b)$$

Combining Eq. 3.22- Eq.3.26, a set of quadratic nonlinear differential equations for $E_{F\uparrow}$ and $E_{F\downarrow}$ is obtained. The boundary conditions at $x = L_1$ and $x = L_2$ are that both the EC and current for each spin component are continuous. For the local structure, the simplest scenario neglects spin currents at the outer edges of the device. Because charge currents also vanish at the outer edges, the boundary conditions at $x = 0$ and $x = L_3$ are that both spin-dependent current components are zero. The set of differential equations can then be solved numerically.

In the electron conduction regime, $E_F > 0$ and $V_G > 0$. Similar equations can be obtained for the hole conduction regime, where $E_F < 0$ and $V_G < 0$, by simply changing the sign of e. The spin detection generally requires a small V_{DS} on the order of millivolts and a large gate bias (magnitude), on the order of volts. When the gate bias is very small, the Fermi level is close to the Dirac point. In that case, quantum transport, which is not considered in this model, is dominant. In practice, the widths (along the x-direction) and hence the coercivities of the contacts are different, so that their magnetization can be tuned separately through an external magnetic field. However, in this calculation, we take both contacts to be $0.5\mu m$ wide for simplicity. The channel length between S and D is $2\mu m$. We take a spin relaxation time to be 0.5 ns. These parameter values are within the range of

relevant experimental results.[16][111] When the magnetization of the two contacts S and D is in the same direction, we define it as the P case, and set the spin-dependent tunneling parameters $g_{S\uparrow} = g_{D\uparrow} = 3g_{S\downarrow} = 3g_{D\downarrow}$; when S and D have opposite magnetization, we define it as the AP case, and set $g_{S\uparrow} = g_{D\downarrow} = 3g_{S\downarrow} = 3g_{D\uparrow}$. In the calculation, we take $g_{S\uparrow}$ to be $6\times10^{23} eV^{-2} cm^{-2} s^{-1}$. Typically, spin valves operate at low temperature; hence, we set $T = 1K$.

The calculated EC potential, ES potential, and charge and spin current density profiles for P and AP cases are shown in Fig. 3.13. The gate bias is $V_{GS} = 20V$ and the drain bias is $V_{DS} = 20mV$. The device is in the electron conduction regime. The discontinuity of the ES potential at the S and D boundaries are due to different screening efficiencies with and without a metal contact on top. The total current J in graphene is constant in the channel, and decreases to zero at $x = 0$ and $x = L_3$. The slight decrease of J_S in the center of the channel is due to spin relaxation. When the contacts are polarized in P, the spin-dependent EC potentials cross, while the spin-dependent currents do not cross; when the contacts are in AP configuration, these results are opposite.[127]

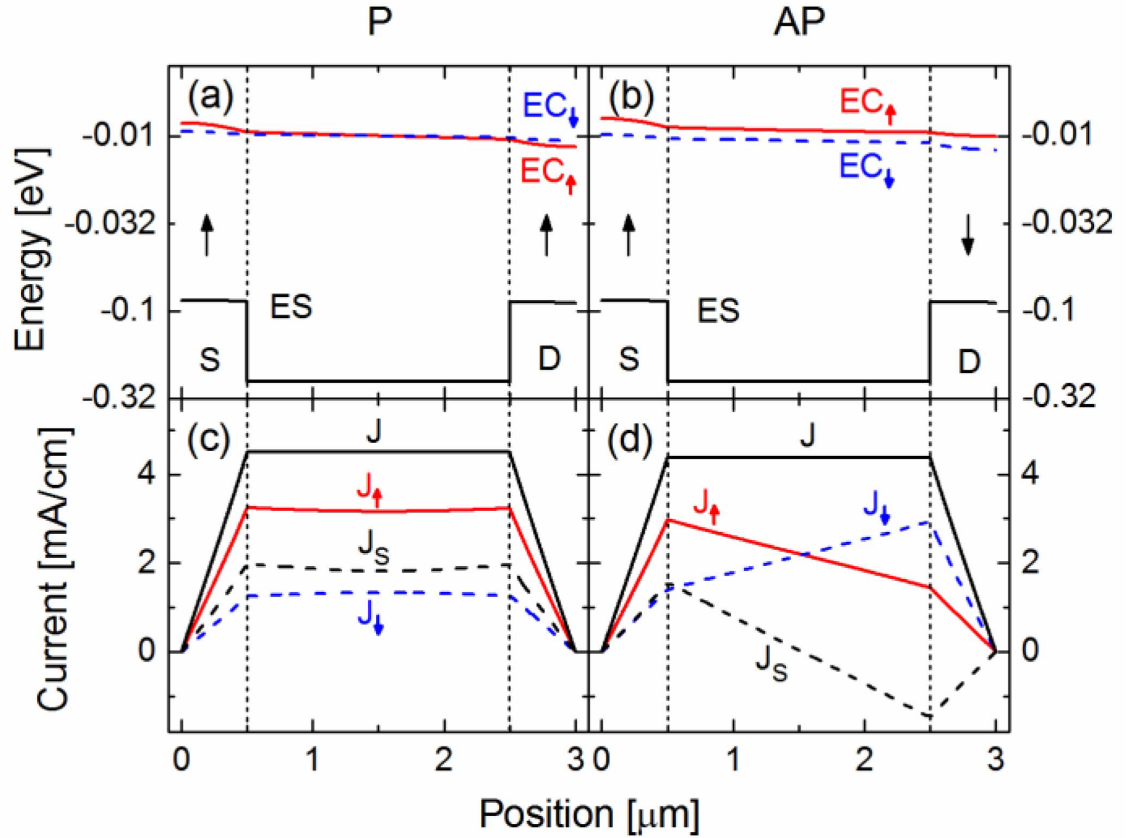

Fig. 3.13. (a) and (b) ES profiles for a local structure for P and AP configurations, respectively. (c) and (d) Current density profiles for a local structure for P and AP configurations, respectively. $V_{DS} = 20mV$, $V_{GS} = 20V$. $EC\uparrow$ and $EC\downarrow$ denote electrochemical potentials for spin up and spin down electrons. ES denotes the electrostatic potential. The current notations are defined in the text. P/AP: FM contacts with P/AP magnetization. Arrows: majority spin direction in the FM contacts. The electron density in the channel is ~$4.3\times10^{12}cm^{-2}$. The energy is shown in a logarithmic scale.

3.4 Spin valve device, nonlocal structure and magnetoresistance

For the local structure that we discuss in Section 3.3, spin and charge are injected and detected together. Hence, the measured MR is small.[16] The purpose of introducing a nonlocal structure is to separate the charge and spin flux, and thereby to enhance the

magnetoresistive effect. As shown in Fig. 3.12, a current source is applied between contacts 3 and 4, injecting both charge and spin into graphene. The charge current can only flow to the left, while the spin current flows in both directions. The ES potential on contacts 2 and 3 are set to be equal so that no charge flow occurs between them.

The nonlocal structure can be incorporated into the model by including the region $-L_0 \leq x \leq 0$ in Fig. 3.12. The differential equations are the same as those for $L_1 \leq x \leq L_2$, shown in Eq. 3.25. The nonlocal spin injection can be described by new boundary conditions. At $x = 0$, the new boundary condition is that both the spin-dependent EC, and current components are continuous. At $x = -L_0$, the new boundary conditions are

$$J = 0, \qquad E_{F\uparrow} - E_{F\downarrow} = \Delta E_F(-L_0) \tag{3.28}$$

In Fig. 3.14, the spin-dependent EC profiles are plotted for both P and AP cases, in order to understand how the nonlocal structure changes the device characteristics. The parameters are $L_0 = 2\mu m$ and $\Delta E_F(-L_0) = 1meV$. Other parameters are the same as those for the local structure. Fig. 3.14a and b shows a low-bias case ($V_{DS} = 2mV$), and Fig. 3.14c and d shows a high-bias case ($V_{DS} = 10mV$). $V_{GS} = 20V$ is used for both cases. The black bars with "×" at the ends show the position of the EC potential at the S and D contacts. It is observed that most of the applied bias V_{DS} drops across the tunneling contacts. For the nonlocal device, due to spin relaxation, $EC_\uparrow - EC_\downarrow$ decreases with spin flux from the left to the right. At low bias, the spintronic property of the device is determined by the extrinsic spin source, and the ECs do not cross for either P or AP cases; while at large bias, the spintronic property is dominated by intrinsic spin injection, and the ECs cross for the P case.

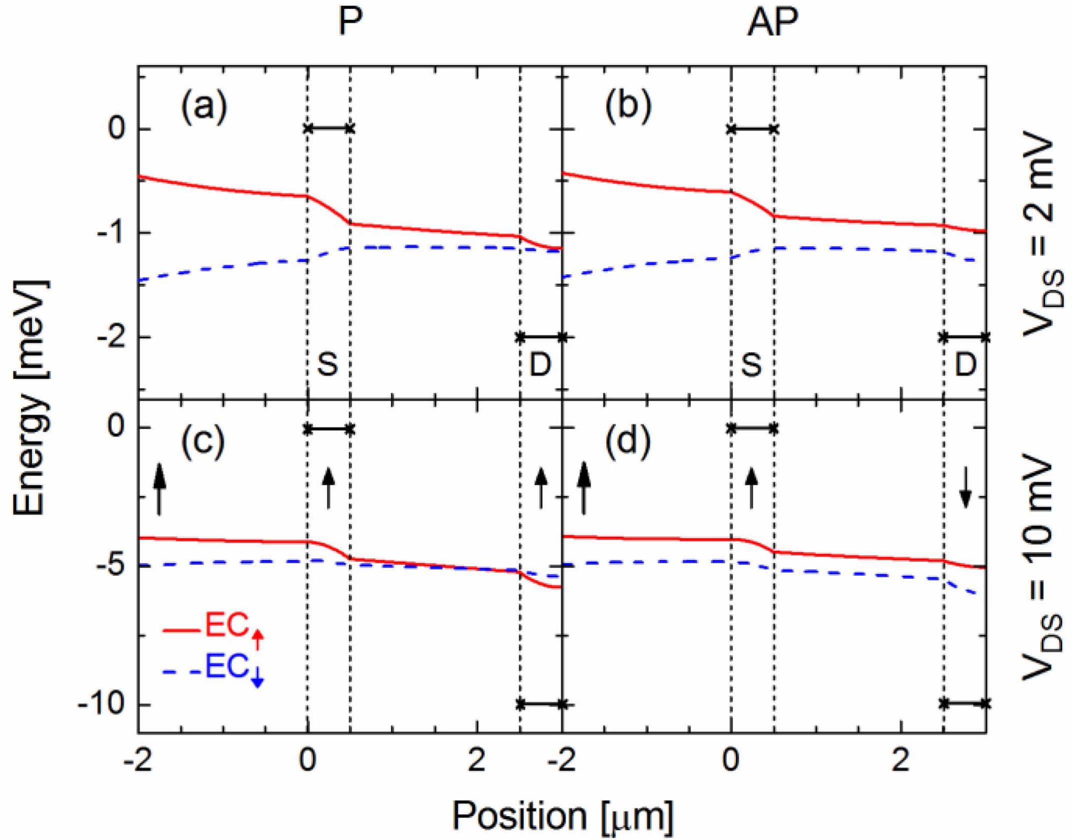

Fig. 3.14. Spin-dependent EC potential profiles for both P [(a) and (c)] and AP [(b) and (d)] configurations in nonlocal devices at low [(a) and (b), $V_{DS} = 2mV$] and high bias [(c) and (d), $V_{DS} = 10mV$]. The black bars with "×" at the ends denote the position of EC potential at the contacts. The large and the small arrows indicate nonlocal spin injection and majority spin direction in the FM contacts, respectively.

We are interested in understanding how $\Delta E_F(-L_0)$ changes with the gate bias V_G. The gate bias affects all four contacts simultaneously. Therefore, it is obvious that if the voltage at S is fixed and the gate bias changes, the spin source parameter $\Delta E_F(-L_0)$ will also depend on V_{GS} (more accurately, V_{G3}, but contacts 2(S) and 3 are held at the same potential). $\Delta E_F(-L_0)$ can be calculated numerically by applying the model described in Section 3.3 to contacts 3 and 4. In this model, we assume AP configuration for contacts 3 and 4, and the injecting contact 3 is ↑. Because the external current source is known and fixed, V_{43} varies at different values of V_{GS}. In Fig. 3.15, the numerically calculated $\Delta E_F(-L_0)$ and V_{43} are plotted as a function of V_{GS}, and the obtained $\Delta E_F(-L_0)$ is used in

following discussion as a V_{GS}-dependent boundary condition in Eq. 3.28. The current source between contacts 3 and 4 is $J = -1.8mAcm^{-1}$.

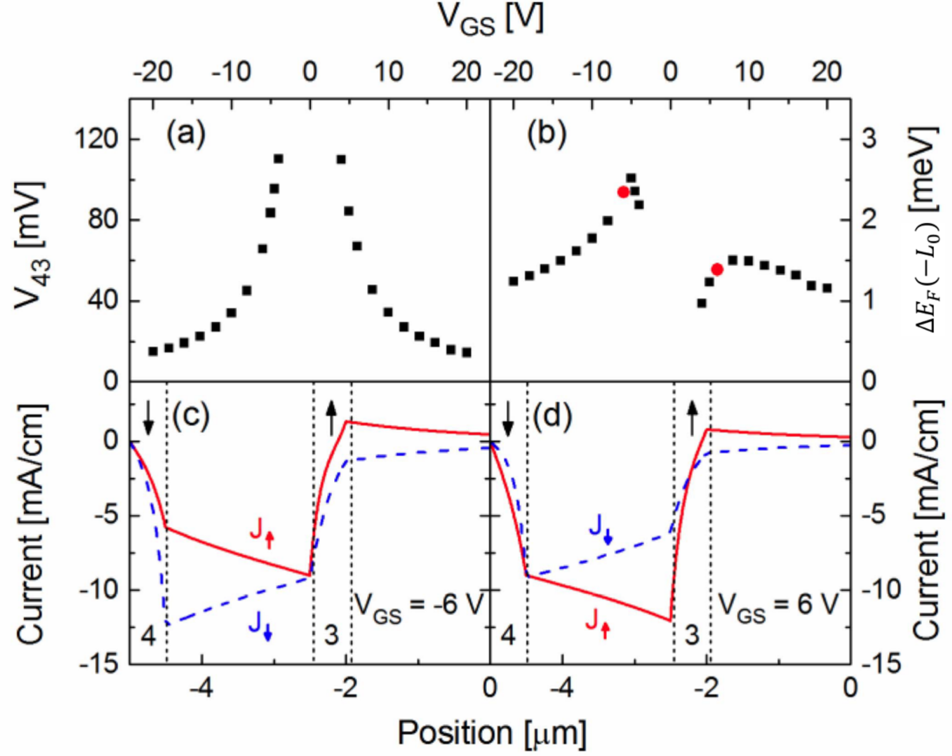

Fig. 3.15. (a) V_{43} and (b) ΔE_F at $x = -L_0$ and as a function of the gate bias, with a constant channel current $J = -1.8mAcm^{-1}$. (c) and (d) Spin-dependent current profile for V_{GS} = −6 and 6 V, respectively. Black arrows: majority spin direction in the FM contacts.

As $|V_{GS}|$ increases, the channel becomes more conducting, and a fixed current leads to a smaller V_{DS} in Fig. 3.15 (a). The value of $\Delta E_F(-L_0)$ shown in Fig. 3.15 (b) increases with $|V_{GS}|$ at small bias and decreases with $|V_{GS}|$ at large bias. When $|V_{GS}|$ is small, the decrease of V_{DS} is dominant, and therefore, the spin injection increases, which is typical in magnetic tunnel junctions.[128] When $|V_{GS}|$ is large, the increase of the carrier density in graphene is dominant, and therefore, the fraction of spin polarized carriers with V_{GS}, leading to a smaller $\Delta E_F(-L_0)$. It is also observed that $\Delta E_F(-L_0)$ is greater for hole conduction than electron conduction. When $V_{GS} > 0$, electron spins are injected into contact 3 and drift toward contact 4. When $V_{GS} < 0$, hole spins are injected into contact 4 and drift toward contact 3. Neglecting spin relaxation, there is more spin accumulation at

contact 3 for the hole conduction regime than for the electron conduction regime. In Fig. 3.15 (c) and (d), (a) negative current means it flows in the +x-direction from contact 4 to contact 3. When the spin-drift effect is insignificant, the crossing of $J_{\uparrow}$ and $J_{\downarrow}$ occurs around the middle of the channel (Fig. 3.13 (d)). When the spin-drift effect is dominant, the crossing of $J_{\uparrow}$ and $J_{\downarrow}$ occurs further downstream.

The spin flux in a spin valve is detected by applying a small bias between contacts 1 and 2. In practice, one can either fix the current between 1 and 2 and measure different values of V_{DS} for P and AP configurations or fix V_{DS} and measure different currents for the two cases. In this paper, we choose the latter option, and the MR can be defined as

$$MR = \frac{J_P}{J_{AP}} - 1 \tag{3.29}$$

where J_P and J_{AP} are the total current densities for parallel and antiparallel configurations. The MR and current as a function of V_{GS} for both local and nonlocal structures are shown in Fig. 3.16, with $V_{DS} = 1mV$. For the specific set of parameters used in the calculations, MR is improved by about four times when employing a nonlocal structure.

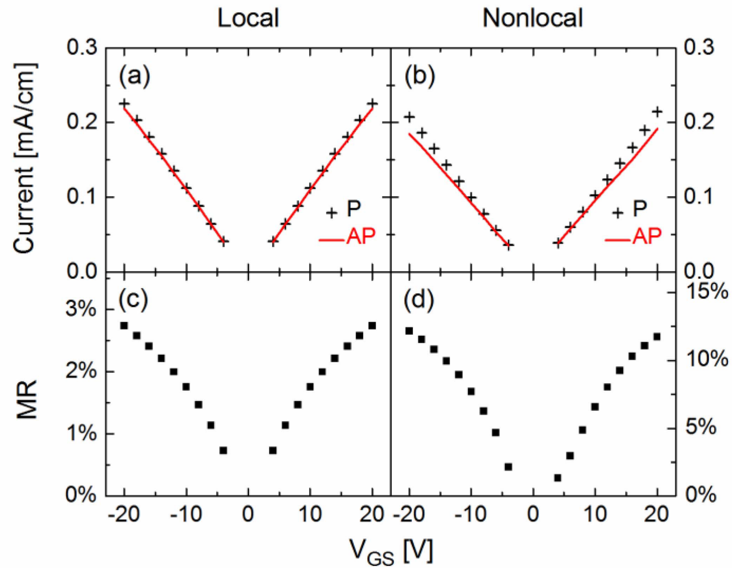

Fig. 3.16. (a) and (b) Current density as a function of V_{GS} for local and nonlocal structures, respectively. (c) and (d) MR as a function of V_{GS} for local and nonlocal structures, respectively. $V_{DS} = 1mV$.

The behavior of MR as a function of V_{GS} is consistent with the experimental results.[111][129] For both local and nonlocal devices, MR increases with V_{GS} at small bias. For nonlocal

devices, MR decreases with V_{GS} at large bias as shown in Fig. 3.17. When the magnitude of V_{GS} is small, the graphene channel is insulating; the charge and the local spin transport in the channel are not very efficient. As $|V_{GS}|$ increases, the channel becomes more conducting. The voltage drop across the contact barriers increases with $|V_{GS}|$, and therefore, the spin injection is more efficient (similar to the transparent contact cases[111][129], where the local effect dominates). When $|V_{GS}|$ continues to increase after most of the voltage has dropped across the contact barriers, the local spin injection saturates, and the decrease of the nonlocal spin injection shown in Fig. 3.17 (a) becomes dominant (similar to the tunnel contact case[111][129], where the nonlocal effect dominates).

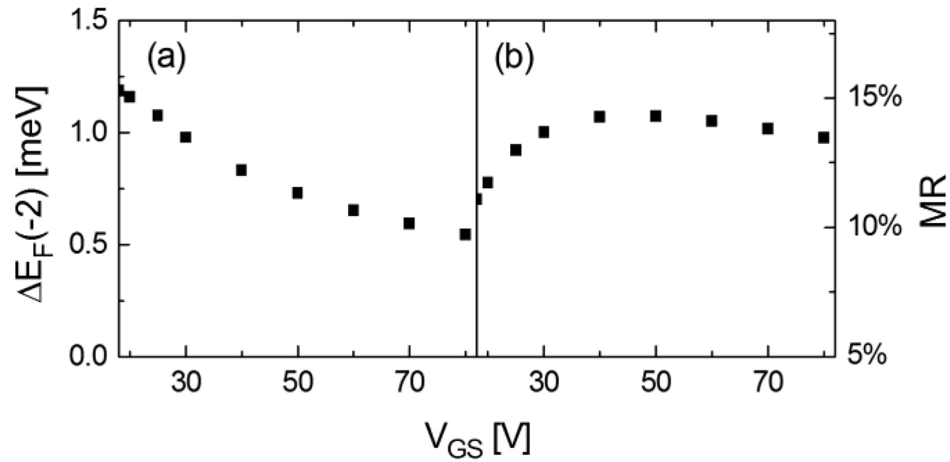

Fig. 3.17. (a) ΔE_F at $x = -L_0$ and (b) MR as a function of V_{GS} for nonlocal devices at large gate bias. $V_{DS} = 1mV$. For V_{GS} = 80 V, the electron density $n = 1.7\times10^{13} cm^{-2}$.

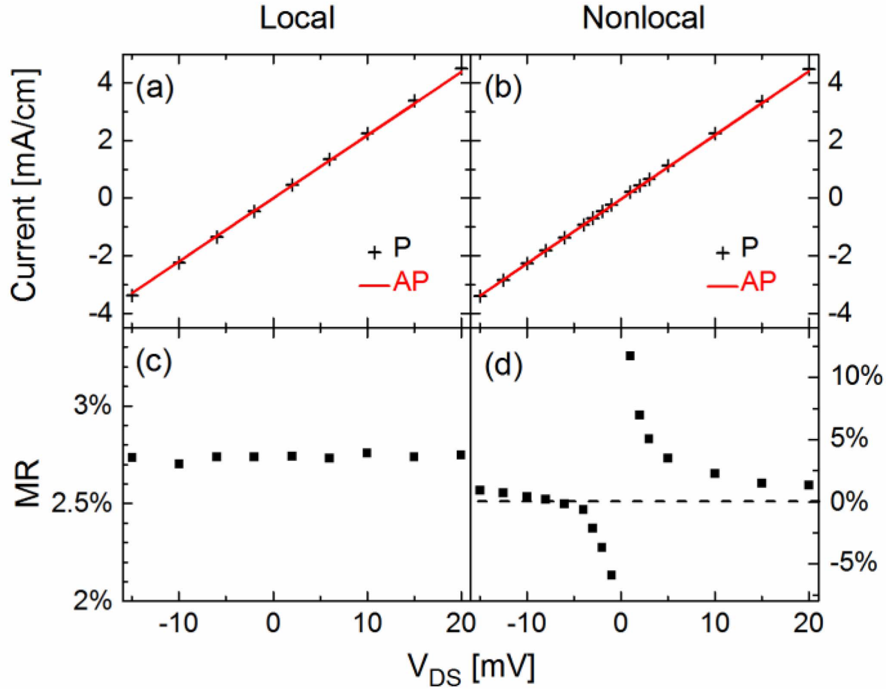

Fig. 3.18. (a) and (b) Current density as a function of V_{DS} for local and nonlocal structures, respectively. (c) and (d) MR as a function of V_{DS} for local and nonlocal structures, respectively. V_{GS} = 20 V.

The MR and current as a function of V_{DS} for both local and nonlocal structures are shown in Fig. 3.18, with $V_{GS} = 20V$. For the local structure, the MR is almost independent of V_{DS}. For the nonlocal structure, the magnitude of MR decreases with applied bias, which is typical in tunnel MR and similar to many results from other types of devices[128][130][131][132]. It is interesting that the nonlocal MR changes sign when V_{DS} changes direction. This result could be anticipated from the quasi-Fermi level profiles shown in Fig. 3.14. When the extrinsic spin accumulation ↑ dominates the whole device, for the injecting contact, it is easier to tunnel into the ↓ subband, which is at a lower energy. Hence, the spin-dependent contact resistance at injection is lower when the contact magnetization is ↓; the spin-dependent contact resistance at collection is lower when the contact magnetization is ↑. For the P case, the overall resistance is comparable for both directions of V_{DS}, while for the AP case, the overall resistance is large when $V_{DS} > 0$ and small when $V_{DS} < 0$, resulting in a sign change of MR.

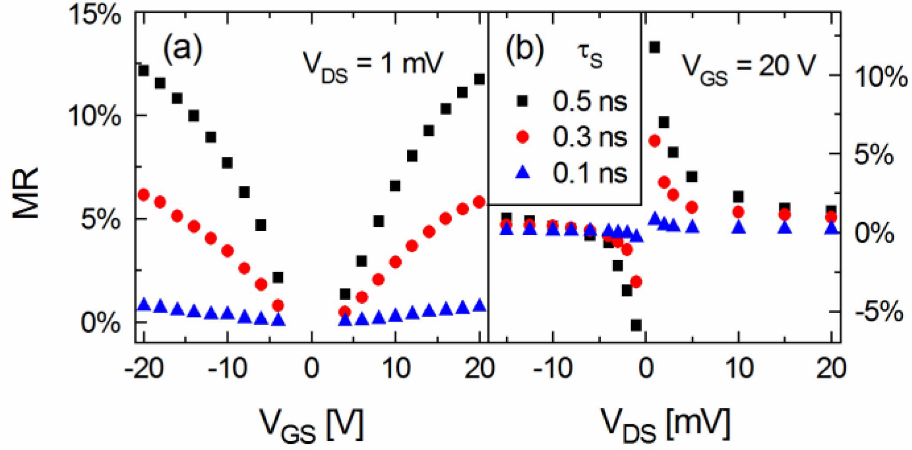

Fig. 3.19. (a) V_{GS} and (b) V_{DS} dependent MR for different spin relaxation times for nonlocal devices.

Fig. 3.19 shows the V_{GS} and V_{DS} dependent MR at different spin relaxation times, $\tau_S = 0.5$, 0.3, and $0.1ns$, for nonlocal devices. The $\tau_S = 0.5ns$ curve is the same as those in Fig. 3.16 and Fig. 3.18. As expected, when spin scattering in graphene is strong, the spin relaxation time is short and the magnetoresistive effect becomes weak.

In experiments, a nonlocal resistance, R_{NL}, is often used, which is defined in the literature[16][111][112],

$$R_{NL} = \frac{V_{DS,P}^{OC} - V_{DS,AP}^{OC}}{J} \tag{3.30}$$

where $V_{DS,P}^{OC}$ and $V_{DS,AP}^{OC}$ are V_{DS} under open-circuit conditions (when the current between S and D is 0) for both P and AP cases, respectively. J is the current between contacts 3 and 4. The calculated open-circuit voltage and nonlocal resistance are shown in Fig. 2.20. When the current source is fixed and the gate bias increases, both V_{DS}^{OC} and R_{NL} initially increase and subsequently decrease. The results are consistent with those in Fig. 3.16 and Fig. 3.17. When the gate bias is fixed and the current varies, V_{DS}^{OC} changes linearly and R_{NL} is almost constant. When the channel conductance is fixed, R_{NL} is determined by the intrinsic properties of the device, such as spin diffusion length and spin injection/detection efficiency. [16][111][112]

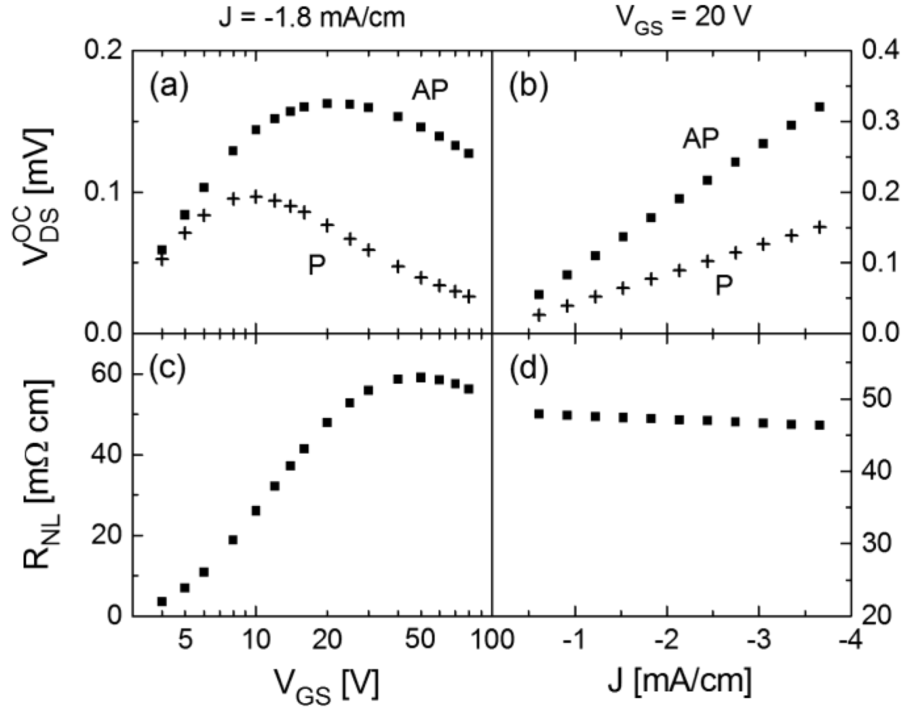

Fig. 3.20. V_{DS}^{OC} ($I_{DS} = 0$) for both P and AP cases, as a function of (a) V_{GS} and (b) current J between contacts 3 and 4. Nonlocal resistance R_{NL} as a function of (c) V_{GS} and (d) current J .

We start introduction of graphene spintronic in Section 3.1 with potential spintronic device applications such as ASL and STT-RAM. The advantage of using graphene as spin channeling material is also explained. In Section 3.2, we explore in detail an extrinsic spin-orbit interaction, Rashba effect. Ionized impurity scattering and Rashba spin scattering due to Rashba effect are calculated. Then we focus on the spin injection and transport in a graphene spin valve structure. A local and non-local model is studied in Section 3.3 and 3.4. We here conclude the study on graphene, which is an isotropic material with Dirac type carriers. Another 2D material that has received much attention recently, black phosphorus (BP), is investigated in Chapter 4. BP has a parabolic conduction band structure as a 2DEG, but its in-plane anisotropy makes it unique compared to other finite band gap 2D materials such as MoS_2.

Chapter 4 Modeling of Anisotropic Transport in Black Phosphorus

4.1 Introduction for 2D materials beyond graphene

Since the discovery of graphene, 2D materials have gained the interest of researchers from physics, chemistry, material science and engineering. Though graphene has shown high mobility up to $10^6 cm^2V^{-1}s^{-1}$, other 2D semiconductors are being explored now because of the lack of band gap in intrinsic graphene. A lot of progress has been made with the transition metal dichalcogenides (TMDs) like MX_2, where M stands for transition metal such as Mo or W, and X can be a chalcogen such as S or Se. For example, MoS_2 is a promising material for electron device applications due to its finite band gap, thermal stability and compatibility with CMOS processes. The atomically thin layer meets the ultra thin body (UTB) concept for most advanced sub-10nm device scaling including FinFET and UTB-SOI, as previously discussed in Chapter 1.

In addition to TMDs a new 2D semiconductor, black phosphorus (BP, or phosphorene), is emerging as a promising semiconductor in the 2D materials family. Black phosphorus is one of most stable allotropes of phosphorus element. It can be isolated using micromechanical exfoliation into monolayer or multilayer forms. BP has a direct band gap that spans 0.3-1.5eV, depending on the number of layers, making it an excellent candidate for infrared optoelectronics. BP has a mobility of $10^3{\sim}10^4 cm^2V^{-1}s^{-1}$, On/Off ratios of ~10000 have been achieved, bridging the application range between graphene and TMDs (See Fig.4.1). The good electrical transport properties, with the highest carrier mobility after graphene, and a moderate energy gap larger than k_BT at room temperature makes BP a promising candidate for nanoelectronics beyond silicon. Each BP layer has a puckered structure with sp^3 hybridization, leading to a 2D material with high in-plane anisotropy. The anisotropic electrical and optical properties include anisotropic charge carrier mobility,

high Seebeck coefficient for thermoelectric applications, and linear optical dichroism[133][134][135].

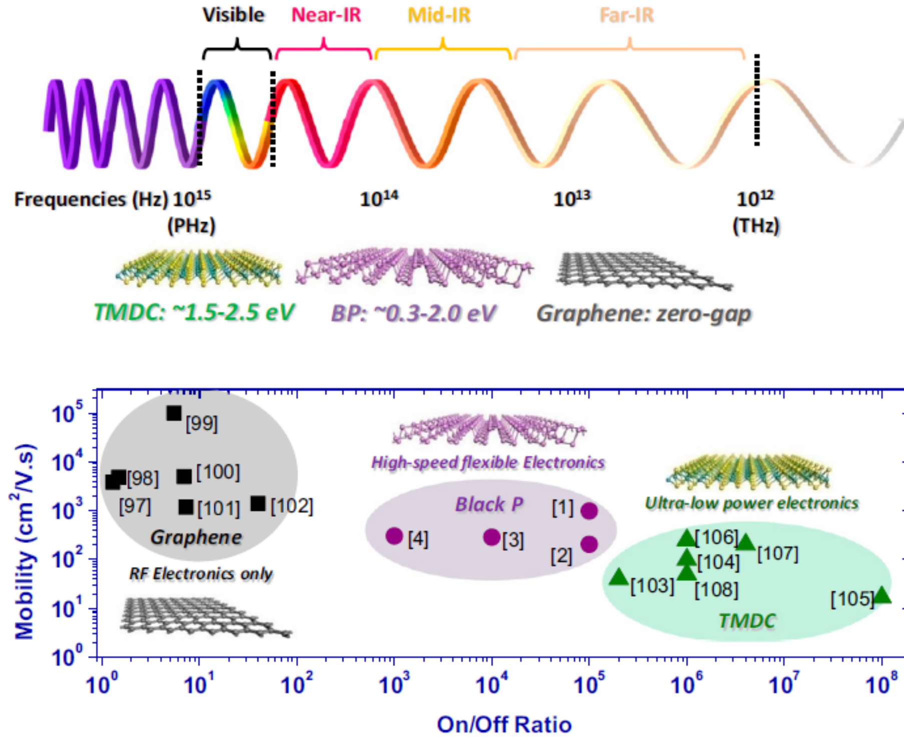

Fig. 4.1. Wave spectrum, band gap rages, mobility and on/off ratio of 2D materials. The dots correspond to data from references in Ling et.al[25].

The BP puckered crystal structure leads to highly anisotropic energy bands with an order of magnitude difference for in-plane effective masses between armchair ($\hat{x}$) and zigzag ($\hat{y}$) directions. For example, the effective masses in bulk BP were measured with cyclotron resonance techniques to be $m_{xx}^{e} = m_{xx}^{h} = 0.08m_0$ and $m_{yy}^{e} = 0.7m_0$, $m_{yy}^{h} = 1.0m_0$.[136] For monolayer BP, these masses were predicted to be $m_{xx}^{e} = m_{xx}^{h} = 0.15m_0$, with m_{yy}^{e} and m_{yy}^{h} being same as in bulk BP.[133][137] There have been several theoretical studies of the anisotropic transport properties of BP, but the anisotropy was not treated explicitly. This is because the momentum relaxation time evaluated with the Boltzmann transport equation, does not have a closed form solution for an anisotropic material.[138] The problem has been avoided so far by deviating approximate solutions that are not entirely suitable due to high anisotropy of the BP electronic system. In later Sessions of

Chapter 4, the methodology of solving for the anisotropic mobility of BP within the Boltzmann transport equation in relaxation time approximation is studied.

Specifically, Chapter 4 is devoted to the investigation of anisotropic electronic transport properties in BP, including momentum relaxation time, carrier mobility and anisotropy ratio. An ionized impurity is considered as scattering center in BP for the calculation. The approach can be extended to other mechanisms, such as electron-phonon scattering. In Section 4.1, a brief overview of development of 2D materials from graphene to TMDs and BP was presented. Electronic properties are discussed with a focus on anisotropy. In Section 4.2, our approaches to tackle BP anisotropy are introduced starting with the Boltzmann transport equation. A matrix method is used to obtain the momentum relaxation time from an implicit integral equation. The difference in treatment of isotropic material (e.g. graphene) and anisotropic material (e.g. BP) are discussed by comparing Section 2.3 in Chapter 2 and Section 4.2 in Chapter 4. In Section 4.3, we numerically calculate the momentum relaxation time and anisotropic mobility for the zero temperature case, with dependence on electric field direction, impurity distance and charge carrier density. In Section 4.4, the calculation of relaxation time and mobility is extended to finite temperature. For finite temperature, scattering is no longer limited to Fermi surface. Screening effects also vary with temperature. There are two competing mechanisms, screening and thermal excitation. Screening dominates the temperature dependence for $T < 100K$, which is the temperature region for ionized impurity scattering. Due to the screening dominating effect, mobility decreases as T increasing.

4.2 Method and approach to evaluate 2D anisotropic Boltzmann transport

Within linear response, we again use the Boltzmann transport equation (BTE) to investigate electronic transport properties.

$$\frac{\partial f}{\partial t} + \vec{v} \cdot \nabla_{\vec{r}} f - \frac{e\vec{\xi}}{\hbar} \cdot \nabla_{\vec{k}} f = \left(\frac{\partial f}{\partial t}\right)_{scatter} \tag{4.1}$$

In contrast to the graphene momentum relaxation time in Eq. 2.50, the relaxation time for BP depends both on the wave vector of the incoming state and the direction of the electric field, i.e. $\tau_m(\hat{\xi}, \vec{k}_i)$ can be written as the following expression

$$\frac{1}{\tau_m(\hat{\xi}, \vec{k}_i)} = \frac{1}{(2\pi)^2} \int_{all\,\vec{k}_j} d^2k_j \, P_{\vec{k}_i,\vec{k}_j} \left\{1 - \frac{[\hat{\xi} \cdot \vec{v}(\vec{k}_j)]\tau_m(\hat{\xi}, \vec{k}_j)}{[\hat{\xi} \cdot \vec{v}(\vec{k}_i)]\tau_m(\hat{\xi}, \vec{k}_i)}\right\} \tag{4.2}$$

where $\hat{\xi}$ is the direction of applied electric field. More details about derivation of Eq. 4.2 can be found in Appendix A. The transition rate $P_{\vec{k}_i,\vec{k}_j}$ between incoming state $|\vec{k}_i\rangle$ and outgoing state $|\vec{k}_j\rangle$ can be expressed by Fermi's golden rule

$$P_{\vec{k}_i,\vec{k}_j} = \frac{2\pi}{\hbar} \left|\langle \vec{k}_j | H | \vec{k}_i \rangle\right|^2 n_{imp} \delta[E(\vec{k}_i) - E(\vec{k}_j)] \tag{4.3}$$

where H is the interaction Hamiltonian. For ionized impurity scattering, H represents the screened Coulomb interaction. By changing H, the approaches introduced here in Chapter 4 can be extended to other scattering mechanisms, such as electron-phonon interaction. A typical impurity density of $n_{imp} = 10^{12} cm^{-2}$ is used for our calculation unless otherwise stated.[133][139] Please note that n_{imp} can be different in real experimental measurements, so it is more or less a fitting parameter. By changing n_{imp}, mobility values varies proportionally. Thus mobility anisotropy ratio could be more desired under some circumstances since n_{imp} is eliminated from the ratio.

As introduced in Section 4.1, due to the difference in effective mass m_{xx} and m_{yy} for $\hat{x}$ (armchair) and $\hat{y}$ (zigzag) directions, the energy dispersion is ellipsoidal for monolayer BP

$$E(\vec{k}) = \frac{\hbar^2}{2}\left(\frac{1}{m_{xx}} {k_x}^2 + \frac{1}{m_{yy}} {k_y}^2\right) \tag{4.4}$$

The conduction band minimum at Γ is defined as $0\ eV$. $\vec{v}(\vec{k}) = \frac{1}{\hbar}\nabla_{\vec{k}} E(\vec{k})$ is the group velocity in Eq. 4.2. The model structure is illustrated in Fig. 4.2 (a), where a monolayer BP is placed on a SiO_2 insulating substrate. Charged impurities, distributed at some distance d from the interface, interact with carriers in BP through the screened Coulomb interaction.

The scattering transition from $|\vec{k}_i\rangle$ to $|\vec{k}_j\rangle$ is shown in Fig. 4.2 (b). The transfer vector is once again denoted by $\vec{q} = \vec{k}_j - \vec{k}_i$. For 2DEG, the density of states (DOS) $g_{2D} = \frac{m_d}{\pi\hbar^2}$ is a constant (The DOS for graphene in Eq. is not a constant since graphene has a linear dispersion). The DOS effective mass $m_d = \sqrt{m_{xx}m_{yy}}$.

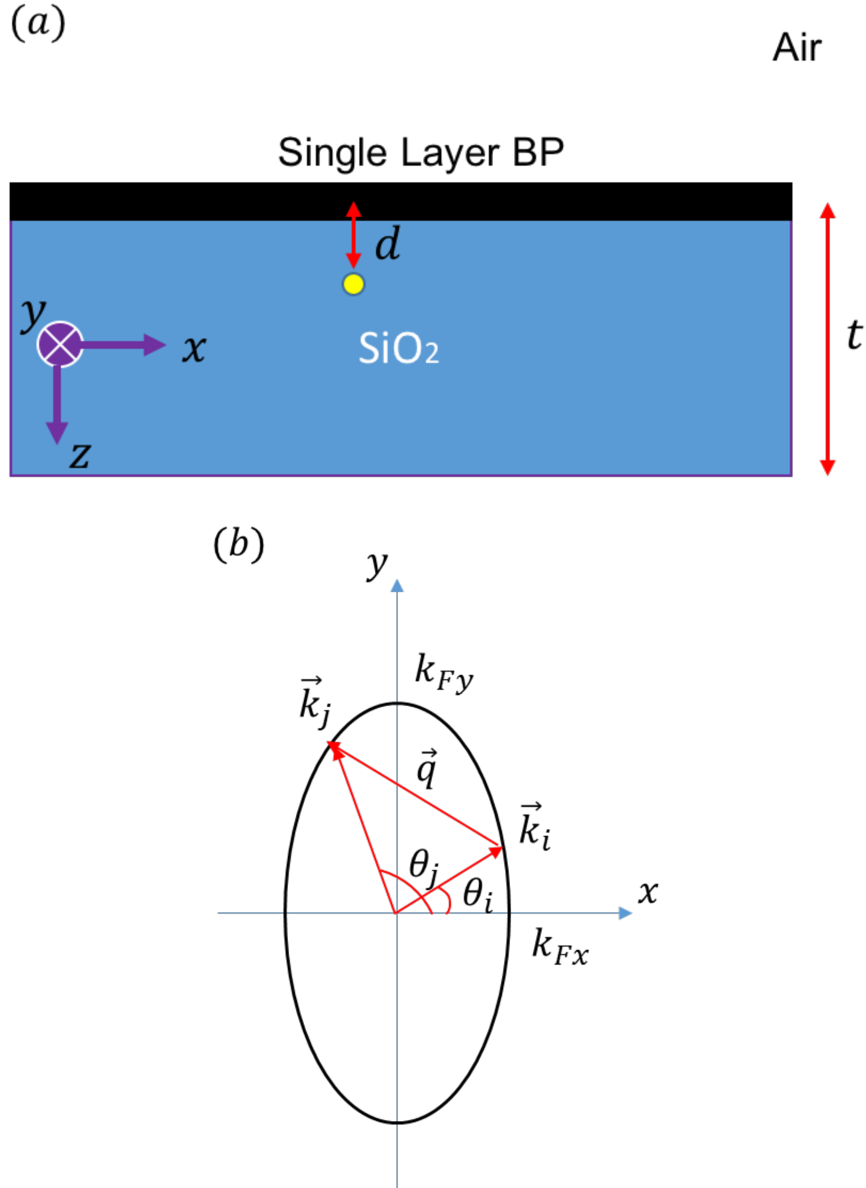

Fig. 4.2. Model structure schematic. (a) BP/SiO_2 as semiconductor/insulator layer structure, with a charged impurity represented by a yellow dot at distance d. (b) Charged impurity scattering occurs on an ellipsoidal phase space contour, with x and $y$being the armchair and zigzag directions of BP.

A linear, static polarization function $\Pi(\vec{q})$ to accommodate screening effect at zero temperature can be written as[38]

$$\Pi(\vec{q}) = g_{2D} Re\left[1 - \sqrt{1 - \frac{8E_F/\hbar^2}{q_x{}^2/m_{xx} + q_y{}^2/m_{yy}}}\right] = g_{2D} Re\left[1 - \sqrt{1 - \frac{4E_F}{E(\vec{q})}}\right] \quad (4.5)$$

, where $E_F = \frac{\hbar^2 \pi n}{m_d}$ is Fermi energy, and n is the charge carrier density. In general, $\Pi(\vec{q})$ depends on $\vec{q}$ and is anisotropic. However, it can be shown that $\Pi(\vec{q})$ is isotropic for $q \equiv |\vec{q}|$ constrained by $q \leq 2|\vec{k}_F \cdot \hat{q}|$, which corresponds to the transition space illustrated in Fig. 4.2 (b). since ionized impurity scattering is an elastic process and only occurs on the Fermi surface for $T = 0K$. Thus the polarizability simply reduces to $\Pi(\vec{q}) = g_{2D}$ in the zero temperature limit. For finite temperature, $\Pi(\vec{q})$ becomes anisotropic and will be discussed in detail in Section 4.4. Subsequently, the matrix element in Eq. 4.3 is written as,[3]

$$\left|\langle \vec{k}_j | H | \vec{k}_i \rangle\right| = \frac{2\pi e^2 e^{-q \cdot d}}{q\kappa + 2\pi e^2 \Pi(\vec{q})} \quad (4.6)$$

The effective dielectric constant is $\kappa \approx 2.5$ for the air and SiO_2 (substrate) half spaces. It is worth pointing out that the relaxation time τ_m of an anisotropic material depends both on the direction of the electric field, $\hat{\xi}$, and on the wave vector of the incoming state $|\vec{k}_i\rangle$. The magnitude of the electric field $|\vec{\xi}|$ is of course irrelevant in linear response.

The strongly anisotropic structure of BP $\left(\frac{m_{yy}}{m_{xx}} \approx 7\right)$ requires solving for the momentum relaxation time $\tau_m(\hat{\xi}, \vec{k}_i)$ from the implicit integral equation Eq. 4.2, rather than the simpler expression Eq. 2.50 for isotropic materials, such as graphene. The numerical procedure is shown as follows. Starting with the transition rate $P_{\vec{k}_i, \vec{k}_j}$ expression Eq. 4.3 and inserting it into Eq. 4.2,

$$\frac{1}{\tau_m(\hat{\xi}, \vec{k}_i)} = \frac{1}{(2\pi)^2} \int_0^{2\pi} d\theta_j \int_0^{\infty} k_j dk_j \, \frac{2\pi}{\hbar} \left|\langle \vec{k}_j | H | \vec{k}_i \rangle\right|^2 n_{imp} \delta[E(\vec{k}_i) - E(\vec{k}_j)] \left\{1 - \frac{[\hat{\xi} \cdot \vec{v}(\vec{k}_j)]\tau_m(\hat{\xi}, \vec{k}_j)}{[\hat{\xi} \cdot \vec{v}(\vec{k}_i)]\tau_m(\hat{\xi}, \vec{k}_i)}\right\} \quad (4.7)$$

Let $\beta(\vec{k}_i) = \sqrt{\frac{E(\vec{k}_i)}{\frac{\hbar^2 cos^2\theta_j}{2m_{xx}}+\frac{\hbar^2 sin^2\theta_j}{2m_{yy}}}} = k_j\sqrt{\frac{E(\vec{k}_i)}{E(\vec{k}_j)}}$, $\alpha(\vec{k}) = \hat{\xi}\cdot\vec{v}(\vec{k})$ to simplify notation, Eq. 4.7 becomes

$$\frac{1}{\tau_m(\hat{\xi},\vec{k}_i)} = \frac{1}{(2\pi)^2}\int_0^{2\pi} d\theta_j \int_0^{\infty} k_j dk_j \ \frac{2\pi}{\hbar}\left|\langle\vec{k}_j|H|\vec{k}_i\rangle\right|^2 n_{imp}\frac{\delta(\beta^2 - k_j{}^2)}{\frac{\hbar^2 cos^2\theta_j}{2m_{xx}}+\frac{\hbar^2 sin^2\theta_j}{2m_{yy}}}\left[1-\frac{\alpha(\vec{k}_j)\tau_m(\hat{\xi},\vec{k}_j)}{\alpha(\vec{k}_i)\tau_m(\hat{\xi},\vec{k}_i)}\right] \quad (4.8)$$

Using the delta function property

$$\delta(\beta^2 - k_j{}^2) = \frac{1}{2\beta}\left[\delta(k_j+\beta)+\delta(k_j-\beta)\right] \quad (4.9)$$

and have

$$M_{i,\,j} = \frac{2\pi}{\hbar}\left|\langle\vec{k}_j|H|\vec{k}_i\rangle\right|^2 n_{imp}\left(\frac{\hbar^2 cos^2\theta_j}{2m_{xx}}+\frac{\hbar^2 sin^2\theta_j}{2m_{yy}}\right)^{-1} \quad (4.10)$$

Then Eq. 4.8 can be simplified to

$$\frac{1}{\tau_m(\hat{\xi},\vec{k}_i)} = \frac{1}{(2\pi)^2}\int_0^{2\pi} d\theta_j\left\{M_{i,\,j}\frac{1}{2}\left[1-\frac{\alpha[\vec{k}_j=(\beta,\theta_j\,)]\tau_m[\hat{\xi},\vec{k}_j=(\beta,\theta_j\,)]}{\alpha(\vec{k}_i)\tau_m(\hat{\xi},\vec{k}_i)}\right]\right\} \quad (4.11)$$

One can further identify $W(\theta_j) = \left(\frac{\hbar^2 cos^2\theta_j}{2m_{xx}}+\frac{\hbar^2 sin^2\theta_j}{2m_{yy}}\right)^{-1}$, which can be viewed as a DOS along the energy contour. Discretizing leads to a series of linear equations

$$\frac{1}{\tau_i} = b\sum_j M_{i,\,j}\left(1-\frac{\alpha_j\tau_j}{\alpha_i\tau_i}\right) \quad (4.12)$$

where $b = \frac{1}{(2\pi)^2}\frac{\Delta\theta_j}{2}$, with $\Delta\theta_j = \frac{2\pi}{N-1}$, and $\alpha_i \equiv \alpha(\vec{k}_i)$. Index $i = 1,\ldots,N$ stands for ith discrete points of $|\vec{k}_i\rangle$ along the elliptical k-contour. Then the following expression can be found

$$-\alpha_1 + b\sum_j M_{1,\,j}\,\alpha_1\tau_1 = b(M_{1,1}\alpha_1 \quad M_{1,2}\alpha_2 \quad \cdots \quad M_{1,N}\alpha_N)\begin{pmatrix}\tau_1\\ \tau_2\\ \vdots\\ \tau_N\end{pmatrix}$$

$$-\alpha_2 + b\sum_j M_{2,\,j}\,\alpha_2\tau_2 = b(M_{2,1}\alpha_1 \quad M_{2,2}\alpha_2 \quad \cdots \quad M_{2,N}\alpha_N)\begin{pmatrix}\tau_1\\ \tau_2\\ \vdots\\ \tau_N\end{pmatrix}$$

$$\vdots$$

$$-\alpha_i + b\sum_j M_{i,j}\,\alpha_i\tau_i = b\begin{pmatrix} M_{i,1}\alpha_1 & M_{i,2}\alpha_2 & \cdots & M_{i,N}\alpha_N \end{pmatrix}\begin{pmatrix}\tau_1\\ \tau_2\\ \vdots\\ \tau_N\end{pmatrix}$$

Arranging the above expressions as a matrix equation $[T]|\tau_m\rangle = |\alpha\rangle$,

$$-\begin{pmatrix}\alpha_1\\ \alpha_2\\ \vdots\\ \alpha_N\end{pmatrix} + b\begin{bmatrix} \alpha_1\sum_{j=1}^{N} M_{1,j} & & \cdots & \\ & \alpha_2\sum_{j=1}^{N} M_{2,j} & \cdots & \\ & & \ddots & \vdots \\ \vdots & \vdots & \cdots & \alpha_N\sum_{j=1}^{N} M_{N,j} \end{bmatrix}\begin{pmatrix}\tau_1\\ \tau_2\\ \vdots\\ \tau_N\end{pmatrix}$$

$$= b\begin{bmatrix} M_{1,1}\alpha_1 & M_{1,2}\alpha_2 & \cdots & M_{1,N}\alpha_N \\ M_{2,1}\alpha_1 & M_{2,2}\alpha_2 & \cdots & M_{2,N}\alpha_N \\ \vdots & \vdots & \ddots & \vdots \\ M_{N,1}\alpha_1 & M_{N,2}\alpha_2 & \cdots & M_{N,N}\alpha_N \end{bmatrix}\begin{pmatrix}\tau_1\\ \tau_2\\ \vdots\\ \tau_N\end{pmatrix} \tag{4.13}$$

the array of τ_m is found by inverting $[T]$ iteratively. In our computation, we employed a total of $N = 1000$ points.

4.3 Zero temperature relaxation time and mobility calculation

Following the approaches described in last section, we first compute the anisotropic momentum relaxation times $\tau_m(\hat{x}, \vec{k}_i)$ and $\tau_m(\hat{y}, \vec{k}_i)$ for $T = 0K$. Hole effective masses of $m_{xx} = 0.15m_0$ and $m_{yy} = 1.0m_0$ are used unless otherwise stated since most BP devices currently made are P-MOSFET. For monolayer BP, the anisotropy ratio of the hole

effective mass is also larger than that of electron effective mass. Carrier density $n = 10^{13}cm^{-2}$ and impurity distance $d = 1nm$ are employed for the calculation. The results are plotted in Fig. 4.3.

(a)

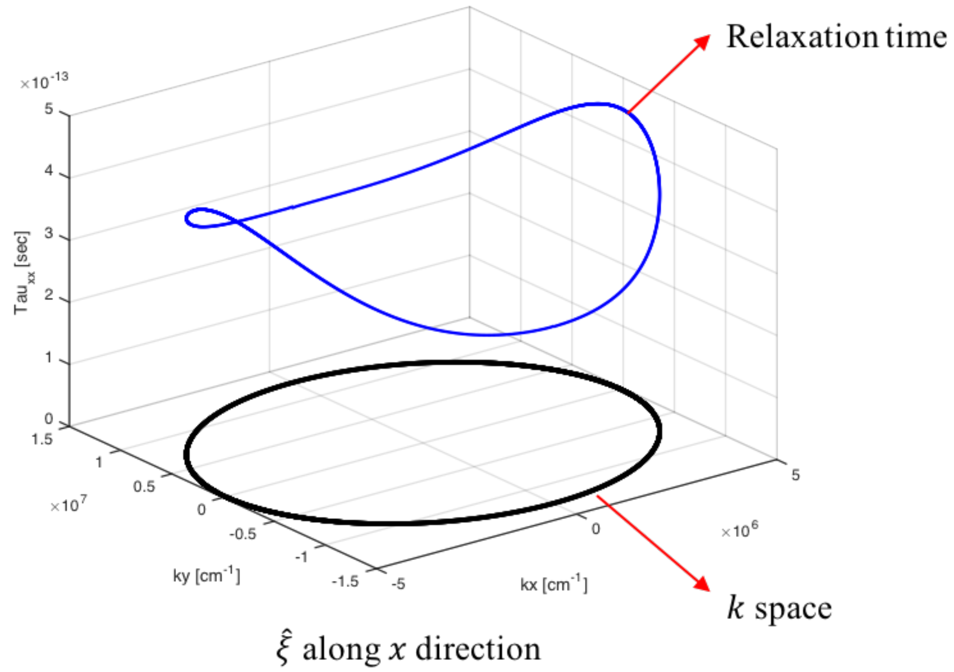

$\hat{\xi}$ along x direction

(b)

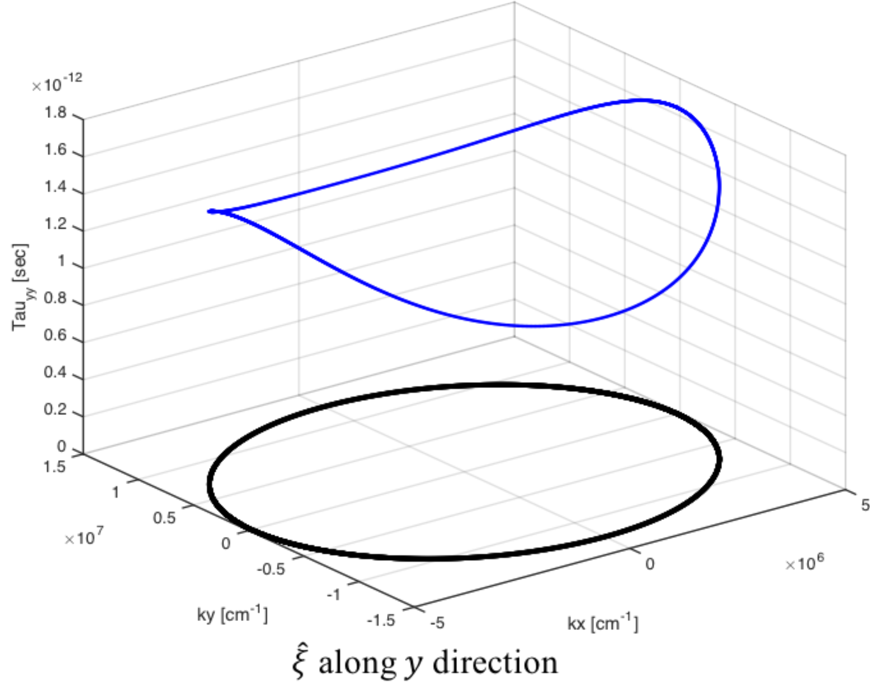

$\hat{\xi}$ along y direction

Fig. 4.3. Relaxation time for electric field along x and y directions. Carrier density $n = 10^{13}cm^{-2}$, impurity distance $d = 1nm$ and impurity density $n_{imp} = 10^{12}cm^{-2}$.

The calculated momentum relaxation time is on the order of picoseconds, which is reasonable for the assumed impurity concentration. There is only one curve in Fig. 4.3 (blue) for zero temperature; it will become a continuous surface for finite temperature cases. Fig. 4.3 can be also plotted in forms of τ_m as a function of incoming angle θ_i for different carrier density n in Fig. 4.4 (a), or $\langle\tau_m\rangle = \frac{1}{N}\sum_{\theta_i}\tau_m(\hat{\xi},\vec{k}_i)$ averaged over θ_i to show the carrier density dependence. One finds relaxation time is larger when the applied electric field is along the $\hat{y}$ direction, i.e. $\tau_m(\hat{y},\vec{k}_i) > \tau_m(\hat{x},\vec{k}_i)$, and a relaxation time anisotropy ratio of ≈ 5 is obtained. Momentum relaxation favors back-scattering against the direction of the electric field. This is apparent from the $1 - \frac{[\hat{\xi}\cdot\vec{v}(\vec{k}_j)]\tau_m(\hat{\xi},\vec{k}_j)}{[\hat{\xi}\cdot\vec{v}(\vec{k}_i)]\tau_m(\hat{\xi},\vec{k}_i)}$ term in Eq. 4.2, which in the isotropic case will reduce to $1 - cos\theta_{ij}$ in Eq. 2.50. Due to the band anisotropy, back-scattering requires a larger q when $\hat{\xi}$ is along $\hat{y}$. Since $M_{i,j}$ decreases

with increasing q, this leads to a larger momentum relaxation time, i.e. $\tau_m(\hat{y},\vec{k}_i) > \tau_m(\hat{x},\vec{k}_i)$.

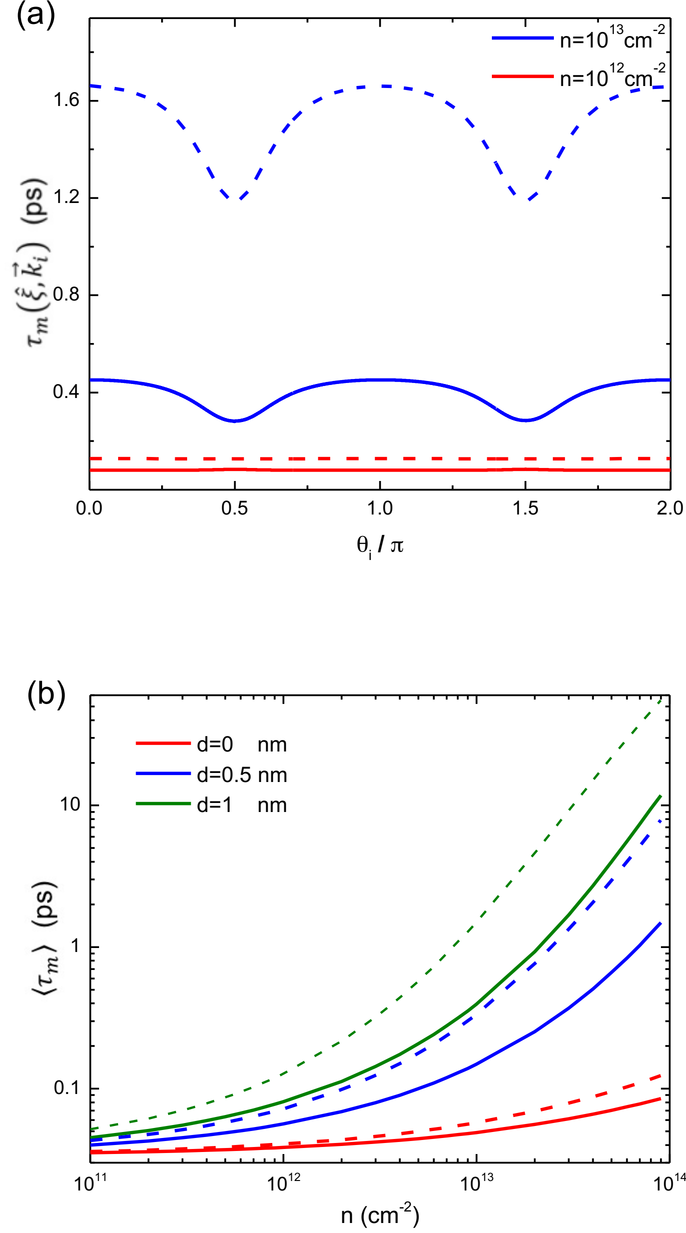

Fig. 4.4. Calculated momentum relaxation time, τ_m, and its dependence on impurity distance, d, carrier density, n, and electric field direction, $\hat{\xi}$. Solid and dashed lines are for $\hat{\xi}$ along x and y directions, respectively. (a) τ_m varies with the initial wave vector, $\vec{k}_i$, for $d = 1nm$, $\tau_m(\hat{x},\vec{k}_i) < \tau_m(\hat{y},\vec{k}_i)$. (b) Average $\langle\tau_m\rangle$ dependence on n, for different d.

In addition to its dependence on the direction of the electric field, τ_m also depends on the incoming state wave vector $\vec{k}_i$ as can be seen from Fig. 4.3 and Fig. 4.4 (a). We consider the simpler case of $d = 0$. In this limit, the scattering matrix element $M_{i,j}$ will be independent of the initial state $\vec{k}_i$ if $q \ll \frac{2\pi e^2}{\kappa} g_{2D}$. Since q increases with the Fermi energy, one can identify a carrier density at which τ_m changes from being independent of $\vec{k}_i$ to being $\vec{k}_i$-dependent. Fig. 4.4 (a) reflects this behavior. When the carrier density is small enough, such that q is negligible compared to the effective screening term, $\frac{2\pi e^2}{\kappa} g_{2D}$, τ_m is independent of $\vec{k}_i$ (red curves in Fig. 4.4 (a)). Whereas for large n, we observe that τ_m has minima when $\theta_i = \frac{\pi}{2}$ and $\frac{3\pi}{2}$. The scattering matrix element $M_{i,j}$ in Eq. 4.10 depends on an effective angular DOS, $W(\theta_j)$. In the limit of extreme anisotropy, i.e. $m_{yy} \gg m_{xx}$, the maxima of $W(\theta_j)$ occur near $\theta_j = \frac{\pi}{2}$ and $\frac{3\pi}{2}$. It can be seen from Fig. 4.2 (b) that q is zero in that limit when $\theta_i = \frac{\pi}{2}$, and the $M_{i,j}$ reaches maximum. As a result, τ_m has a minimum at $\theta_i = \frac{\pi}{2}$ for high carrier densities. Increasing carrier density n increases the effective q involved in scattering. Therefore increasing d and/or n lead to smaller $M_{i,j}$ and larger $\langle\tau_m\rangle$, as shown in Fig. 4.4 (b).

With relaxation time $\tau_m(\hat{\xi}, \vec{k}_i)$ computed, the effective mobility μ or conductivity σ at $T = 0K$ can be investigated. For $\hat{\xi}$ along the x direction we define the relevant mobility as,[138][140]

$$\mu_{xx} = \frac{g_s e}{(2\pi)^2 n} \int d^2\vec{k}\, {v_x}^2(\vec{k}) \tau_m(\hat{x}, \vec{k}) \left(-\frac{\partial f}{\partial E}\right) \tag{4.14}$$

An analogous mobility can be defined for $\hat{\xi}$ along the $\hat{y}$ direction. μ_{xx} and μ_{yy} are non-zero elements of the mobility tensor, $v_x(\vec{k}) = \frac{\hbar k_x}{m_{xx}}$, $g_s = 2$ is the spin degeneracy, $-\frac{\partial f}{\partial E} = \frac{1}{k_B T} f(E)[1 - f(E)]$ is a delta function at zero temperature, $f(E)$ is the Fermi-Dirac distribution. As d or n increase, τ_m increases as previously discussed leading to increasing mobility as shown in Fig. 4.5 (a). Although $\tau_m(\hat{x}, \vec{k}_i) < \tau_m(\hat{y}, \vec{k}_i)$, we find $\mu_{xx} > \mu_{yy}$. The mobility depends on $(\hat{\xi} \cdot \vec{v})^2$, hence, the mobility anisotropy ratio is

$\frac{\mu_{xx}}{\mu_{yy}} \sim \left(\frac{m_{yy}}{m_{xx}}\right)^2 \frac{\langle \tau_m(\hat{x}, \vec{k}_i)\rangle}{\langle \tau_m(\hat{y}, \vec{k}_i)\rangle}$. In this case, $\left(\frac{m_{yy}}{m_{xx}}\right)^2$ is approximately 44. The smaller anisotropy ratio observed is due to the opposing trend of the momentum relaxation time. As illustrated by dashed lines in Fig. 4.5 (b), only when $d = 0$ does the anisotropy ratio decrease monotonically as a function of n in the range investigated. When $d \neq 0$, for each dashed $\frac{\mu_{xx}}{\mu_{yy}}$ curve, there is a minimum located around $n_{cut} = (2\pi d^2)^{-1}$, that originates from the scattering matrix element $M_{i,j}$ depending exponentially on $q \cdot d$. Therefore d defines an effective cutoff for q, and correspondingly a finite n_{cut}. Besides, all curves approximately share a similar minimum of ≈ 1.5. For larger d, the minimum at $\sim(2\pi d^2)^{-1}$ is found at smaller n. It is interesting to note that our calculated anisotropy ratio varies from 1.5 to 7 depending on the values of n and d.

To eliminate the effect of the impurity distance, d, we employ a uniform impurity distribution model. Using $n_0 = \frac{n_{imp}}{t}$, to replace n_{imp} in Eq. 2, where $t = 300nm$ is the total thickness of the SiO_2 layer, we replace the matrix element in Eq. 4.3 with $\left|\langle \vec{k}_j | H | \vec{k}_i \rangle\right| = \frac{2\pi e^2 e^{-q \cdot z}}{q\kappa + 2\pi e^2 \Pi(\vec{q})}$. Then the new momentum relaxation time with uniform impurity distribution can be modelled as

$$\frac{1}{\tau_m(\hat{\xi}, \vec{k}_i)} = \frac{1}{(2\pi)^2} \int_{all\ \vec{k}_j} d^2\vec{k}_j \int_0^t dz \frac{2\pi}{\hbar} \left[\frac{2\pi e^2 e^{-q\cdot z}}{q\kappa + 2\pi e^2 \Pi(\vec{q})}\right]^2 n_0 \delta\left[E(\vec{k}_i) - E(\vec{k}_j)\right] \left\{1 - \frac{[\hat{\xi} \cdot \vec{v}(\vec{k}_j)]\tau_m(\hat{\xi}, \vec{k}_j)}{[\hat{\xi} \cdot \vec{v}(\vec{k}_i)]\tau_m(\hat{\xi}, \vec{k}_i)}\right\} \tag{4.15}$$

The mobility and anisotropy ratio calculated using the uniform impurity distribution model are shown as black curves in Fig. 4.5 (a) and (b). As stated above, increasing distance leads to increasing mobility. The curve varies similarly to the $d = 0$ case and is now also monotonic as a function of n, which can be understood as that impurities nearest to BP have the largest influence. Uniform distribution of the impurities also reduces the sensitivity to n.

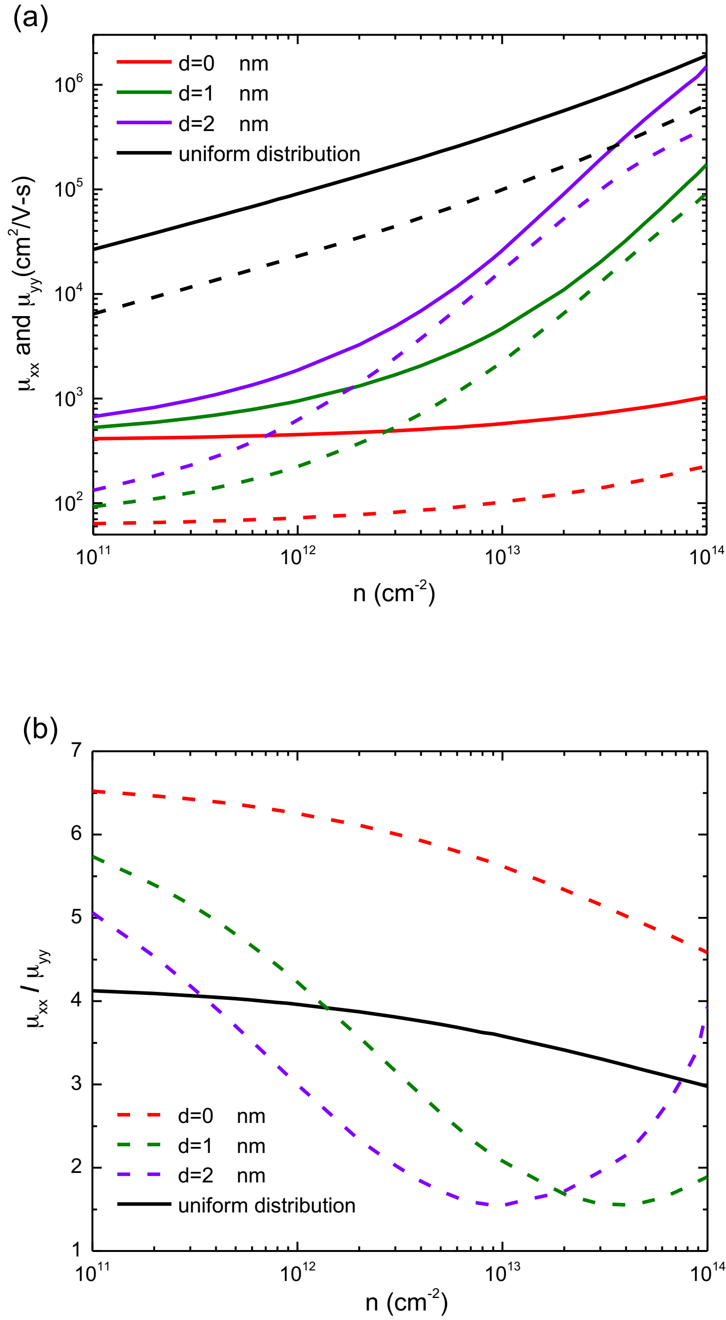

Fig. 4.5. Calculated mobility and anisotropy ratio, related to impurity distance, d, and carrier density, n. Impurity density,$n_{imp} = 10^{12}cm^{-2}$(a) mobility $\mu_{xx} < \mu_{yy}$. Solid and dashed lines represent μ_{xx} and μ_{yy}, respectively. (b) Anisotropy ratio, $\frac{\mu_{xx}}{\mu_{yy}}$, changing as a function of n. Solid and dashed lines represent uniform model and constant distance model, respectively.

To sum up, we find hole mobilities on the order of $10^3 - 10^4 cm^2/Vs$ for carrier densities $10^{12} - 10^{13} cm^{-2}$. On the experimental side, hole Hall mobility of order $10^3 cm^2/Vs$ at carrier density of about $6.7\times10^{12} cm^{-2}$ has been observed at low temperature.[37] [141] This would suggest that our assumed impurity concentration of $n_{imp} = 10^{12} cm^{-2}$ probably under-estimates the experimental situation or there could be other sources of scattering, e.g. neutral impurities, short-range trap states, and surface roughness. As previously suggested, a better quantity for comparison with experiment may be the anisotropy ratio, $\frac{\mu_{xx}}{\mu_{yy}}$, which does not depend on n_{imp}.

The mobility anisotropy ratios for holes are evaluated to be ~3.5-4, across the range of hole densities shown in Fig. 4.5 (b). Using $m_{xx}^e = 0.15m_0$ and $m_{yy}^e = 0.7m_0$, we calculate the electron mobility anisotropy ratio of $\sim$2.4-3.2, across the same range of carrier densities. These anisotropy ratios are larger than $\frac{\mu_{xx}}{\mu_{yy}} \approx 1.8$ obtained from Hall hole mobility measurements at $120K$,[37] and results obtained from nonlocal resistance measurements, which yielded $\frac{\mu_{xx}}{\mu_{yy}} \approx 1.66 \pm 1.1$ at 5-$50K$. On the other hand, angle-resolved field effect mobility measurements yield a ratio of ~2-4.[141] Our calculated anisotropy ratio is expected to be larger than experimental measurements since we are using zero temperature model in this section. Finite temperature calculation will be presented in Section 4.4. With that being said, one may identify two possible reasons for the discrepancy. First, few-layer BP samples with a thickness around 10nm were used in the experiments. Their multi-subbands electronic structures can lead to scattering between subbands. In addition, experimental measurements were conducted at finite temperature 10-120K, which might reduce the anisotropy. The mobility anisotropy observed in experiments so far are relatively insensitive to carrier concentration, more consistent with our case of uniform impurity distribution. This might suggest that charged impurities in experimental samples are probably due to bulk dopants, perhaps introduced as grown. With advancement in BP growth techniques, one may eventually approach situations where the mobility is limited by interfacial impurities like in the case of state-of-the-art semiconductor devices.

In this section, the ionized-impurity-scattering limited hole mobility of monolayer BP within a Boltzmann transport model is calculated for zero temperature, considering the full anisotropy of the transport and electronic structure explicitly. We explored the momentum relaxation time dependence on the electric field direction as well as on the incoming wave vector. Although $\tau_m(\hat{x}, \vec{k}_i) < \tau_m(\hat{y}, \vec{k}_i)$, we find $\mu_{xx} > \mu_{yy}$ with mobility anisotropy ratios ∼3.5-4. The influence of the effective mass difference is compensated by the opposing trend of the relaxation time. Based on methods introduced in Section 4.2 and 4.3, we will extend the calculation for finite temperature in the next section.

4.4 Finite temperature relaxation time and mobility calculation

In this section, we will investigate the ionized impurity scattering limited anisotropic relaxation time and mobility for finite temperature in monolayer BP. We will follow similar approaches introduced in Section 4.2 and 4.3 and discuss which quantities change due to the finite temperature. The calculation will be focused on the relatively low temperature region, up to $T \sim 120K$, where the electron-phonon interaction is weak and ionized impurity scattering is the dominating mechanism. The BP samples made by current fabrication techniques can be defective compared to the state of the art silicon devices or graphene, thus ionized impurity scattering can be very important. Additionally, we are motived by recent experimental measurements that BP mobility has a small temperature dependence weaker than $T^{-\frac{1}{2}}$ for $T < 100K$,[37][141] which may not be explained by electron-phonon interaction. In our previous calculation, we found the BP mobility anisotropy ratio is about 3-4 for zero temperature, which is somewhat larger than the ratio of 1.5-2 from experimental measurements done at 50-150K. We expect the calculated anisotropy ratio for finite temperature will be smaller and become better matched to the

experimental reports. The finite temperature not only affects the mobility difference along $\hat{x}$ (armchair or light effective mass direction) and $\hat{y}$ (zigzag or heavy effective mass direction), it also introduces variations such as temperature dependent screening effect and energy dependence for the momentum relaxation time, which are not observable in the zero temperature study of Section 4.3.

For finite temperature, the impurity scattering is still an elastic process but no longer limited to E_F. Instead, it occurs in the vicinity of E_F following a distribution or sampling function $\left(-\frac{\partial f}{\partial E}\right) = \frac{1}{k_B T} f(E) \cdot [1 - f(E)]$, where $f(E)$ is once again the Fermi-Dirac distribution. As expected, there is a higher probability that scattering occurs near the Fermi level and the probability is lower far from E_F. Thus, for finite temperature, we need to consider a continuous energy region rather than a single Fermi energy E_F, as represented in the schematic in Fig. 4.6. In the following discussion, we write the $\vec{k}_i$ dependence of the relaxation time as a function of energy E and incoming wave vector angle θ_i, i.e. $\tau_m(\hat{\xi}, E, \theta_i) = \tau_m(\hat{\xi}, \vec{k}_i)$.

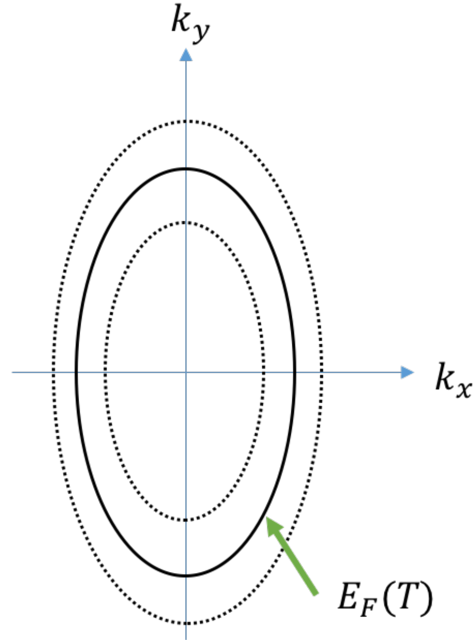

Fig. 4.6. Scattering is no longer limited to Fermi level, but occurs in the vicinity of E_F following $\left(-\frac{\partial f}{\partial E}\right)$. (The schematic is not to scale)

Additionally, the Fermi energy itself is also a function of temperature as $E_F(T) = k_B T ln\left[exp\left(\frac{n}{g_{2D}k_B T}\right) - 1\right]$ and plotted in Fig. 4.7 (a). In the following computations, we consider the energy region $E \in [E_F(T) - 5k_B T, E_F(T) + 5k_B T]$ for $E_F(T) - 5k_B T > 0$ and $E \in [0,10k_B T]$ for $E_F(T) - 5k_B T \leq 0$ since there are no available states for energy less than zero (below conduction band minimum). The total $10k_B T$ energy regions covers at least 97% of $f(E) \cdot [1 - f(E)]$, as plotted in Fig. 4.7 (b).

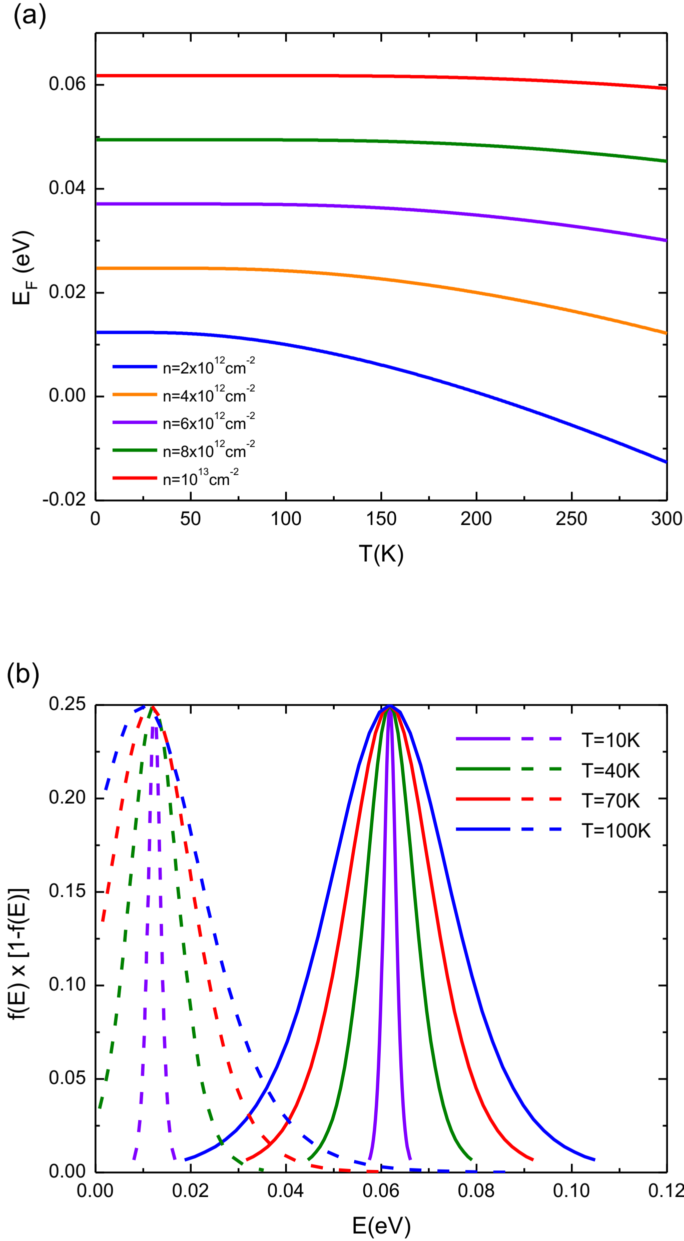

Fig. 4.7. Finite temperature effect on energy (a) $E_F(T)$ for different carrier density (b) sampling function $f(E) \cdot [1 - f(E)]$ for different temperatures and carrier densities. Solid lines $n = 10^{13} cm^{-2}$, $E \in [E_F(T) - 5k_B T, E_F(T) + 5k_B T]$ for all four temperatures; dashed lines $n = 2\times10^{12} cm^{-2}$, $E \in [0,10k_B T]$ except for $T = 10K$.

Another temperature dependent term embedded in $\tau_m(\hat{\xi}, E, \theta_i)$ is the screening or polarization effect, entering through the scattering matrix element $|\langle\vec{k}_j|H|\vec{k}_i\rangle|$.

$$\left|\langle\vec{k}_j|H|\vec{k}_i\rangle\right| = \frac{2\pi e^2 e^{-qd}}{q\kappa + 2\pi e^2 \Pi(\vec{q},T)} = \frac{2\pi e^2}{\kappa}\frac{e^{-qd}}{q + q_s(\vec{q})} \tag{4.16}$$

$\Pi(\vec{q},T)$ is the temperature dependent anisotropic polarizability for BP. As discussed in Section 4.2, the polarizability for $T = 0K$ has a closed form $\Pi(\vec{q},0) = g_{2D}Re\left[1 - \sqrt{1-\frac{4\mu}{E(\vec{q})}}\right]$, where $\mu = E_F(0) = \frac{\hbar^2\pi n}{m_d}$ is the zero temperature Fermi energy. Using the Maldague formula[142][143], the polariziablity for finite temperature can be written as

$$\Pi(\vec{q},T) = \int_0^\infty d\mu \frac{\Pi(\vec{q},0)}{4k_BT cosh^2\left(\frac{E_F(T)-\mu}{2k_BT}\right)} \tag{4.17}$$

A series of $\Pi(\vec{q},T)$ for different temperatures is shown in Fig. 4.8. We find that Eq. 4.17 reduces to Eq. 4.5 in the limit of zero temperature.

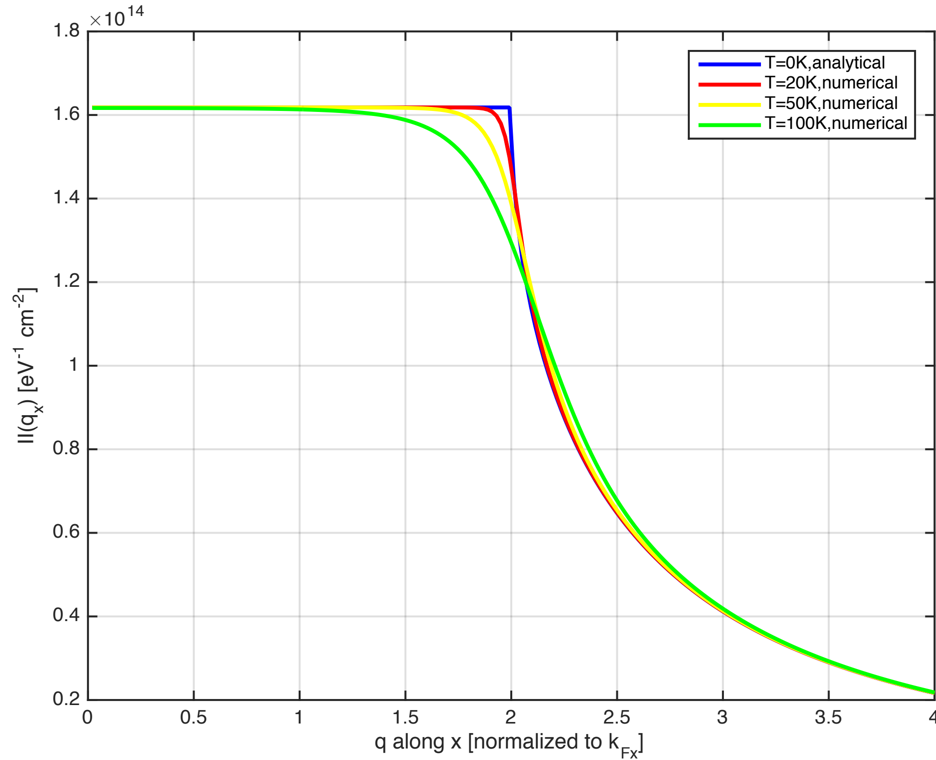

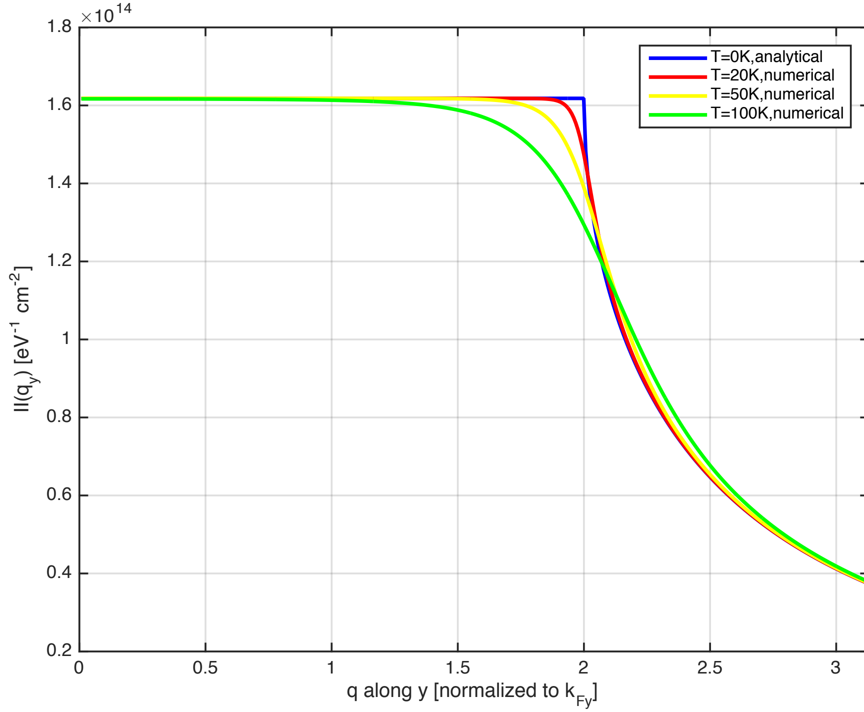

Fig. 4.8. $\Pi(q_x, T)$ and $\Pi(q_y, T)$ for different temperature. As $T \rightarrow 0$, the numerically calculated polarizability reduce to the zero temperature analytical result given by Eq. 4.5.

Analogous to the transferred wave vector $q = |\vec{q}|$ indicating scattering strength, the screening impact due to polarizability is represented by $q_s(\vec{q}) = \frac{2\pi e^2}{\kappa}\Pi(\vec{q}, T)$. For comparison, q_x and q_y axis, as well as screening term q_s are all normalized to the larger effective mass directional Fermi wave vector k_{Fy}, which is only determined by E_F. The plots are shown in Fig. 4.9, with dashed white curves corresponding to different energy regions ($[E_F(T) - 5k_BT, E_F(T) + 5k_BT]$ or $[0, 10k_BT]$). We find the screening effect becomes weaker as temperature increases, but also depends on carrier density [30]. For the same T, $q_s(\vec{q})$ is a function of q_x and q_y. For $T = 0K$, q_s is a constant since scattering occurs only on the Fermi surface (i.e. $\Pi(\vec{q}, 0) = g_{2D}$ for $q_x \leq 2k_{Fx}$, $q_y \leq 2k_{Fy}$). The corresponding energy regions reduce back to a single curve for zero temperature. For finite temperature, q_s decreases as q increases in the entire 2D q-plane. The corresponding energy regions can have both upper and lower bounds for Fig. 4.9 (e) and (f), or only have upper bounds for Fig. 4.9 (b) and (c) since these lower bounds correspond to zero energy.

Alternatively, observing $T = 40$ and $100K$ curves in Fig. 4.7 (b), the energy minimum is $E = 0eV$. There is one single white curve in four plots (Fig. 4.9 (a) and (d), (b) and (c)), however, the reasons are not the same. (For (a) and (d), the $\left(-\frac{\partial f}{\partial E}\right)$ reduces to a delta function at $T = 0K$; for (b) and (c), the energy region minimum is located at origin zero)

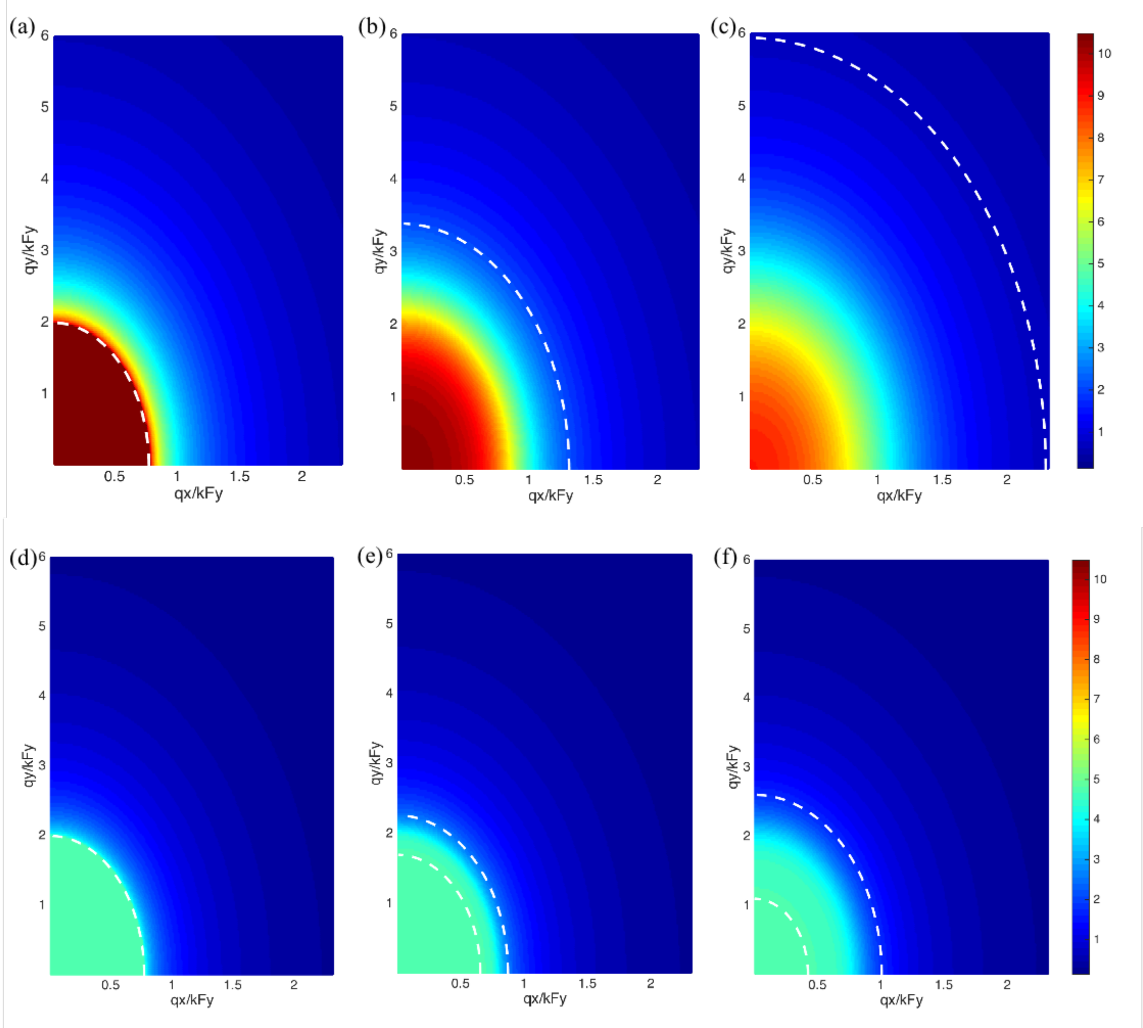

Fig. 4.9. Effective screening term q_s as a function of q_x and q_y (all normalized to k_{Fy}). Dashed white curves correspond to the energy regions for cases, which discussed in Section II. The screening is weaker and energy regions become wider as T increasing. q_s increases while q_s/k_{Fy} decreases as n increasing. (a)-(c) $n = 2\times10^{12}cm^{-2}$, with $T = 0, 40, 100K$, $E \in [0,10k_BT]$. (d)-(f) $n = 10^{13}cm^{-2}$, with $T = 0, 40, 100K$, $E \in [E_F(T) - 5k_BT, E_F(T) + 5k_BT]$

Comparing constant carrier density cases (Fig. 2(a)-(c) with $n = 2\times10^{12}cm^{-2}$ or (d)-(f) with $n = 10^{13}cm^{-2}$), the screening effect becomes less important as T increasing,

for two reasons. First, q_s itself become smaller (or more faded in the figures) as T increases [29, 30]. Second, the energy regions, limited by the sampling function $f(E) \cdot [1 - f(E)]$ as shown in Fig. 4.7 (b), become larger for higher temperature. When temperature is low, the energy region is small and mostly includes strong screening; while for high temperature, the energy region is large and includes a lot of weak screening.

Comparing same temperature cases (Fig. 2(a) and (d) with $T = 0K$, (b) and (e) with $T = 40K$ or (c) and (f) with $T = 100K$), it is worthwhile to mention that although the normalized q_s/k_{Fy} is associated with larger values for smaller n in Fig. 4.9, one finds the screening term q_s itself increases as n increases when $T > 0K$, because the more carriers, the stronger screening phenomena are (except when $T = 0K$, $q_s = \frac{2\pi e^2}{\kappa} g_{2D}$ is independent of n). Furthermore, q_s decreases faster as T increases for smaller carrier density, i.e. transport properties can be more affected by temperature for smaller n.

Two quantities are affected by finite temperature: scattering no longer only happens at the Fermi level and screening becomes temperature dependent. We can proceed to calculate the momentum relaxation time and mobility for $\hat{x}$ (armchair) and $\hat{y}$ (zigzag) directions. Following similar matrix approach as discussed in Section 4.2, τ_m can be calculated from Eq. 4.2 and plotted for different directions of electric field, different carrier densities and different temperatures (Fig. 4.10).

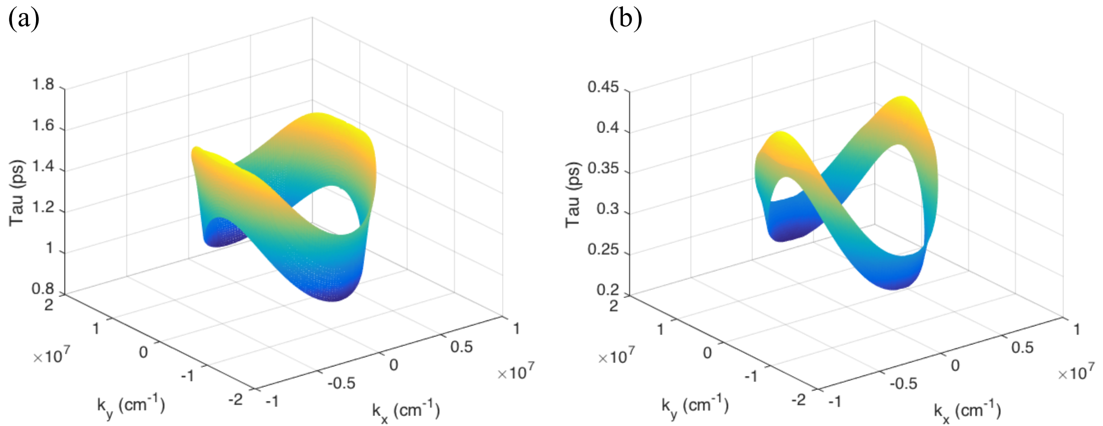

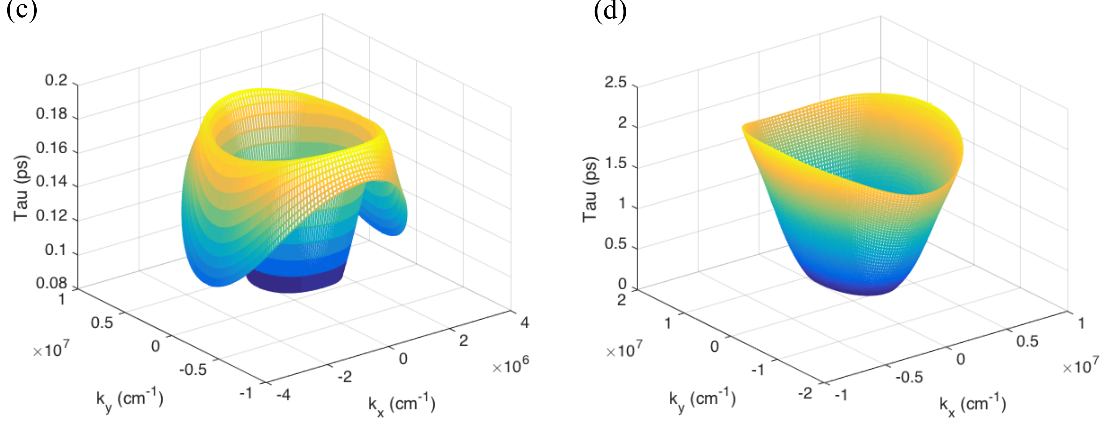

Fig. 4.10. Calculated momentum relaxation time $\tau_m(\hat{\xi}, E, \theta_i)$ in three-dimensional plots plotted for different directions of electric field, carrier densities and temperatures, and. (a) $\tau_m(\hat{y}, E, \theta_i)$ with $n = 10^{13} cm^{-2}$, $T = 20K$. (b) $\tau_m(\hat{x}, E, \theta_i)$ with $n = 10^{13} cm^{-2}$, $T = 20K$. (c) $\tau_m(\hat{y}, E, \theta_i)$ with $n = 2\times10^{12} cm^{-2}$, $T = 20K$. (d) $\tau_m(\hat{y}, E, \theta_i)$ with $n = 10^{13} cm^{-2}$, $T = 100K$.

For Fig. 4.10 (a) and (b), the difference is the direction of the electric field, $\hat{x}$ and $\hat{y}$. For Fig. 4.10 (a) and (c), the carrier density is not the same. Compared to Fig. 4.10 (a), parameters are all the same except that $T = 100K$ in Fig. 4.10 (d). Therefore, the momentum relaxation time can have various shapes subject to different conditions, and needs to be plotted in three-dimensional format with dependence on E and θ_i (or equivalently, k_x and k_y in Fig. 4.10). This is because of the anisotropic electronic structure of BP, which is taken into consideration through the implicit integral equation in Eq. 4.2. Without this consideration, τ_m would only depend on E like other isotropic 2D material such as graphene. Additionally, comparing to Fig. 4.3, plots in Fig. 4.10 are not single curves, but continuous surfaces since energy is not limited to Fermi surface.

It is very helpful to obtain a deeper understanding of $\tau_m(\hat{\xi}, E, \theta_i)$ since it has a significant impact on mobility, naively $\mu \sim \frac{e\tau_m}{m^*}$ from the well-known Drude model. In the numerical computation for finite temperature, $N_\theta = 400$ points are used for angle mesh and $N_E = 100$ points for energy mesh. The τ_m dependence on angle θ and carrier density n was investigated in the last section. Hence, we mainly focus on the dependence on energy and temperature, which may or may not be monotonic. We divide energy into three ranges in the following discussion, depending on different phenomena. To analyze the energy

dependence and eliminate the angle effect, a $\bar{\tau}_m(\hat{\xi}, E)$, which is momentum relaxation time averaged over angle, is calculated using Eq. 4.18 and plotted in Fig. 4.11 for different temperatures

$$\bar{\tau}_m(\hat{\xi}, E) = \frac{1}{2\pi}\int_0^{2\pi} d\theta_i \tau_m(\hat{\xi}, E, \theta_i) \tag{4.18}$$

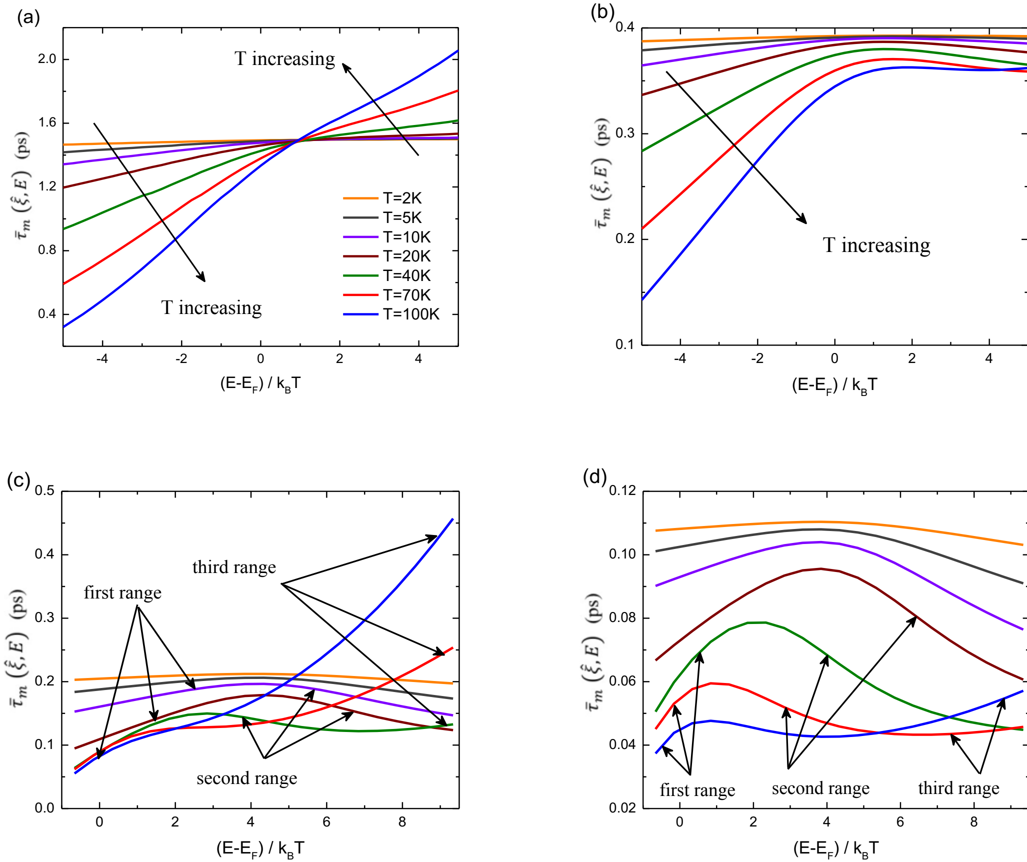

Fig. 4.11. Angle averaged $\bar{\tau}_m$ as a function of energy for different direction of electric field, carrier densities and temperatures. Those first, second and third ranges in figures varies with different curves. (a) $\bar{\tau}_m(\hat{y}, E)$ with $n = 10^{13} cm^{-2}$. (b) $\bar{\tau}_m(\hat{x}, E)$ with $n = 10^{13} cm^{-2}$. (c) $\bar{\tau}_m(\hat{y}, E)$ with $n = 2\times10^{12} cm^{-2}$. (d) $\bar{\tau}_m(\hat{x}, E)$ with $n = 2\times10^{12} cm^{-2}$.

For low temperatures (e.g. $T = 2, 5, 10K$), $\bar{\tau}_m$ has a very weak dependence on energy regardless of the directions of the electric field and the carrier densities. This is due to the energy regions in the sampling function $\left(-\frac{\partial f}{\partial E}\right)$ being very narrow as shown in Fig.

4.7. Specifically, one observes that $\bar{\tau}_m$ first slightly increases, then slightly decreases with E for low temperature. This is because for smaller energy region, effective screening term q_s in Fig. 4.9 is essentially constant. As energy increases, q increases and determines the denominator of $\frac{2\pi e^2}{\kappa}\frac{e^{-qd}}{q+q_s}$. Consequently, the scattering matrix element $\left|\langle\vec{k}_j\middle|H\middle|\vec{k}_i\rangle\right|$ decreases and $\bar{\tau}_m$ increases due to q increasing. And this is the first range for E. As E continue to increase and becomes larger than E_F, q_s decreases rapidly. Since $q_s > q$, the effect of q_s decreasing now dominates. Thus $\left|\langle\vec{k}_j\middle|H\middle|\vec{k}_i\rangle\right|$ increases and $\bar{\tau}_m$ decreases. This is the second range for E. Similar behaviors have been found in the scattering rate calculation of 2DEG inversion layer.[2]

For higher temperatures (e.g. T = 70-100K), the behavior of $\bar{\tau}_m$ is more complicated since it varies with $\hat{x}$, $\hat{y}$ directions and carrier densities. For medium temperature, $\hat{x}$ direction cases ($40-70K$ curves), $\bar{\tau}_m(\hat{x},E)$ dependence on E behaves more or less similar to the low temperature cases. That is, $\bar{\tau}_m(\hat{x},E)$ first increases, then decreases with E increases. For $\hat{y}$ direction or high temperature $\hat{x}$ direction cases, energy region is larger for the sampling function due to high temperature. Furthermore, as E becomes even larger, the screening term has decreased to be so small that q dominates again. Thus $\bar{\tau}_m$ once again increases as E increases, such as the $40K$ curve in Fig. 4.11 (c) or the $100K$ curve in Fig. 4.11 (d). This is the third region for E. Under certain circumstances, the q_s dominated second range is so small that it is masked by the first and third ranges, hence $\bar{\tau}_m$ seems to increase monotonically as E increases. For instance, high temperature curves in Fig. 4.11 (a) and (c), $\bar{\tau}_m$ increases with E monotonically, but it increases slower for moderate energy (corresponding to the second range). The difference between $\hat{x}$ and $\hat{y}$ is due to the magnitude of q_x and q_y in Fig. 4.9. Since q_y is relatively large, it is more likely that there could be a third range for the $\hat{y}$ direction, while for $\hat{x}$ direction, the third range may only exist at higher T. The trend for T increasing is noted in Fig. 4 (a) and (b), while the three ranges are demonstrated in Fig. 4 (c) and (d). Since the energy ranges covered by $f(E)\cdot[1-f(E)]$ are not the same for $n = 2\times10^{12}cm^{-2}$ and $n = 10^{13}cm^{-2}$, the x-axis lower/upper bound in Fig. 4.11 are different. The relaxation time dependence on T will be discussed together with mobility.

With the momentum relaxation time $\tau_m(\hat{\xi}, E, \theta_i)$ calculated in Fig. 4.10, we can proceed to calculate the temperature dependent anisotropic mobility with the following equation (taking $\hat{x}$ direction as an example)[138]

$$\mu_{xx} = \frac{g_s e}{(2\pi)^2 n\hbar^2} \int_0^{2\pi} d\theta_i \int_0^{\infty} dE \frac{k_i(E, \theta_i)}{\left|\frac{\partial E}{\partial k_i}\right|_{\vec{k}_i(E,\theta_i)}} \left(\frac{\partial E}{\partial k_{ix}}\right)^2 \tau_m(\hat{x}, E, \theta_i)\left(-\frac{\partial f}{\partial E}\right) \qquad (4.19)$$

where $g_s = 2$ is the spin degeneracy, $\left(-\frac{\partial f}{\partial E}\right)$ is the effective sampling function, $k_i = |\vec{k}_i|$, $k_{ix} = k_i sin\theta_i$. Equation for μ_{yy} can be obtained similarly. μ_{xx} and μ_{yy} as a function of T are plotted in Fig. 4.12.

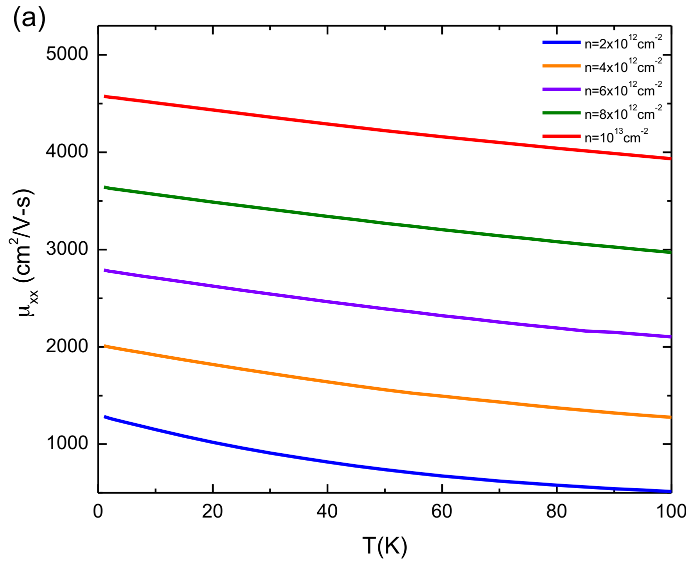

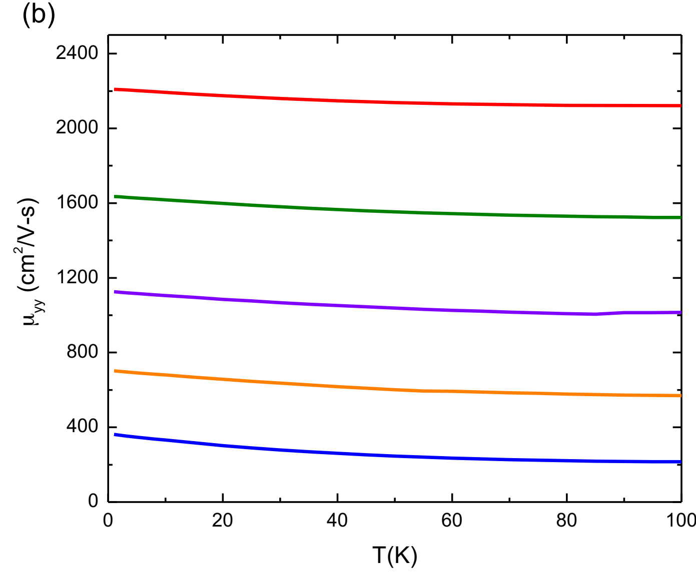

Fig. 4.12. Mobility as a function of temperature related with several carrier densities. The dependence on temperature is rather weak. Impurity density $n_{imp} = 10^{12}cm^{-2}$, impurity distance $d = 1nm$. (a) μ_{xx} (b) μ_{yy}.

Thanks to the double integral of energy E and incoming wave vector angle θ_i in Eq. 4.19, the mobility only depends on temperature and carrier density. There are two competing mechanisms for temperature dependent mobility. At low temperature ($T < T_C$), the screening dominates: as T increases, the screening term q_s becomes smaller (Fig. 4.9) and scattering matrix element $\left|\langle\vec{k}_j\middle|H\middle|\vec{k}_i\rangle\right|$ becomes larger, hence relaxation time and mobility decrease. At high temperature ($T > T_C$), thermal excitation dominates: carriers gain higher thermal velocity, mobility increases as T increases[144]. For anisotropic BP, the critical transition temperature T_C depends on parameters such as the carrier density and the direction of the electric field but is generally around 100-120K. Therefore, for ionized impurity scattering limited temperature region, mobility decreases with increasing temperature, due to the dominance of the effect of screening.

Alternatively, the relationship of mobility and temperature can be recovered from the calculated relaxation time in Fig. 4.11. In Drude model $\mu\sim\frac{e\tau_m}{m^*}$, the τ_m should be understood as the $\bar{\tau}_m(\hat{\xi}, E)$ once again averaged over energy, or noted as $\bar{\bar{\tau}}_m$. (i.e. $\bar{\tau}_m$

averaging over angle, $\bar{\bar{\tau}}_m$ averaging over angle and energy, similar to Eq. 4.18). For $\hat{x}$ direction in Fig. 4.11 (b) and (d), it is straightforward that $\bar{\bar{\tau}}_m$ decreases as T increases because $\bar{\tau}_m(\hat{x}, E)$ decreases as T increases for almost all E. Thus μ_{xx} decreases as T increases. For $\hat{y}$ direction in Fig. 4.11 (a) and (c), $\bar{\tau}_m(\hat{y}, E)$ dependence on T is similar to the $\hat{x}$ direction case when energy is small. For larger energy, $\bar{\tau}_m(\hat{y}, E)$ may increase as temperature increases due to thermal excitation. In these cases, screening effects do not dominate since $q > q_s$ in Eq. 4.16. However, considering the averaging over the energy region and using the full equation for mobility calculation (i.e. Eq. 4.19), one finds overall mobility μ_{yy} decreases as temperature increases. Based on the analysis of mobility dependence on $\hat{x}$ and $\hat{y}$ directions, it can be understood that μ_{xx} decreases faster than μ_{yy} as a function of temperature, since $\bar{\tau}_m$ increases as T increases for some energy regions when the electric field is along the $\hat{y}$ direction. Mobility decreasing rate slows as T continues to increase because the thermal excitation starts to compete with screening effect. By curve fitting, the relation $\mu \propto \frac{1}{n_{imp}}(T + T_0)^{-\alpha}$ can be found. Taking $n = 10^{13} cm^{-2}$ as an example, one gets $\alpha = 0.3$ for μ_{xx} and $\alpha = 0.02$ for μ_{yy}, which has same trend as experimental nonlocal resistance mobility measurements for $T < 100K$.[37][141] In addition to the low temperature region, the dependence is so weak that electron-phonon interaction cannot explain it. Therefore, ionized impurity scattering could be an important scattering process for this temperature region. For even higher temperature ($T > 140K$), the μ_{yy} for certain carrier density may start to increase as T continues to increase, but that temperature region is already beyond the scope of the ionized impurity scattering model.

As discussed in previous work, mobility increases as carrier density n increases. Mobility also has a relatively stronger dependence on T for smaller n because screening is more affected by temperature for lower carrier density as shown in Fig. 4.9, and it is screening that dominates the ionized impurity scattering. Overall the mobility has a weak dependence on temperature for $T < 100K$. The numbers for μ_{xx} and μ_{yy} in Fig. 4.12 are both considerably larger than the currently reported hole mobilities, once again indicating an impurity concentration larger than $10^{12} cm^{-2}$ may exist in real BP samples, which are fabricated as few-layer BP. To eliminate the effect of n_{imp}, the anisotropy ratio $\frac{\mu_{xx}}{\mu_{yy}}$ is a

better quantity for comparison and it is plotted in Fig. 4.13 (a) with its temperature dependence. Since μ_{xx} decreases faster than μ_{yy}, the anisotropy ratio decreases as T increases. An anisotropy ratio of 1.9-3.5 can be found using hole effective masses at $T \sim 50K$, which is smaller than previous zero temperature calculation and a better match to few-layer BP experimental data of 1.6-4, depending on different measurement methods. Moreover, as n increases, $\frac{\mu_{xx}}{\mu_{yy}}$ decreases, i.e. the mobility difference between $\hat{x}$ and $\hat{y}$ directions becomes smaller. Therefore, a BP electronic system at low temperature with small carrier density could have higher anisotrpy. The anisotropy ratio calculated with other parameters such as zero impurity distance, uniform impurity distribution model (averaging the d effect[145]) and electron effective mass ($m_{xx} = 0.15m_0$ and $m_{yy} = 0.7m_0$) are plotted in Fig. 4.13 (b). It can be understood that smaller effective mass ratio leads to a smaller $\frac{\mu_{xx}}{\mu_{yy}}$. The anisotropy ratio decreases as d increases (i.e. impurities located further away from BP plane), which also agrees with our zero temperature calculation.

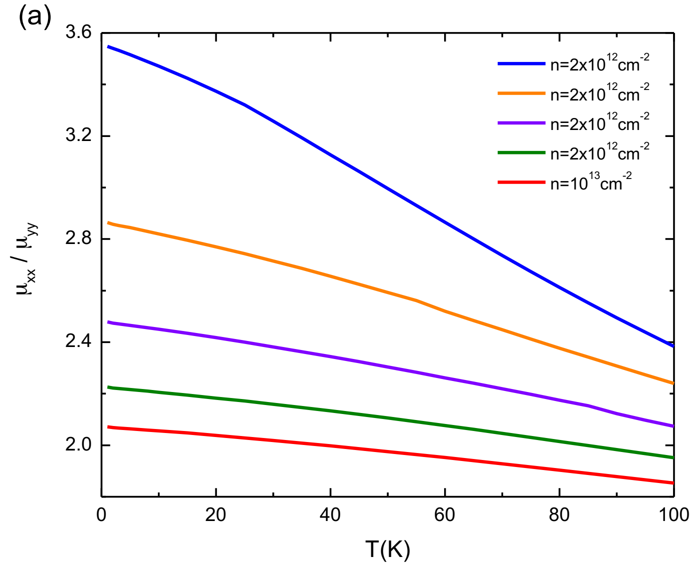

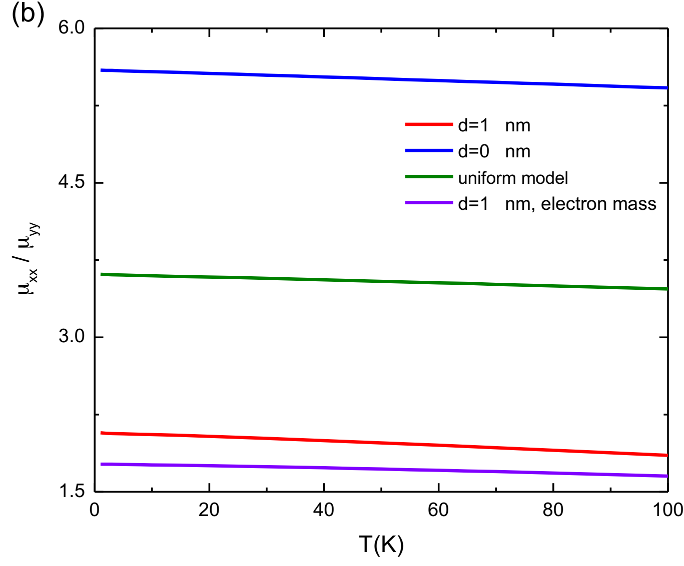

Fig. 4.13. Anisotropy ratio $\frac{\mu_{xx}}{\mu_{yy}}$ decrease as temperature increases (a) Hole effective mass, $d = 1nm$ for different carrier densities. (b) Carrier density $n = 10^{13} cm^{-2}$, calculated $\frac{\mu_{xx}}{\mu_{yy}}$ using other parameters : zero impurity distance, uniform impurity distribution and $d = 1nm$ electron effective mass.

To summarize, the ionized impurity scattering limited BP anisotropic transport properties are investigated in this section with finite temperature dependence. The anisotropic electronic structure not only appears in the mobility difference along $\hat{x}$ and $\hat{y}$ directions, but also leads to the momentum relaxation time and the polarizability being anisotropic with two-dimensional dependence on incoming or scattering wave vectors . In this chapter, screening effect, the momentum relaxation time and mobility, with dependence such as direction of electric field, carrier density, energy regions and temperature, are studied and analyzed in detail. For $T < 100K$, screening effect is found to be dominating though it becomes weaker as T increases. A larger energy region needs to be considered for higher temperature as a result of $f(E) \cdot [1 - f(E)]$ distribution. Depending on whether q or q_s is dominating, $\bar{\tau}_m(\hat{\xi}, E)$ changes as a function of energy can be divided into three ranges and may or may not be monotonic. Overall mobility decreases as temperature increases, but the dependence is weak. The calculated mobility dependence on temperature has the same trend as experimental reports for $T < 100K$, indicating

ionized impurity could be a reasonable scattering model rather than electron-phonon scattering in this temperature region. $\frac{\mu_{xx}}{\mu_{yy}}$ of 1.9-3.5 can be found for $T \sim 50K$ and stronger anisotropy is favored at lower temperature and carrier density. The approach outlined in this chapter can also be applied to other emerging anisotropic 2D materials, including the 1T phase of transition metal dichalcogenides[146][147][148], as well as the transition metal trichalcogenides [149][150][151].

Chapter 5 Summary and Suggestions for Future Work

5.1 Summary

In this thesis, we explore several models related to 2D materials. Basically following the development of 2D materials in past ten years, graphene transport and electronics, spin interaction in graphene, and emerging anisotropic monolayer BP are discussed in Chapter 2, 3 and 4 respectively.

Beginning with a tight binding model, the massless 2x2 Dirac Hamiltonian leads to an energy dispersion in graphene linearly depending on wave vector. Electronic properties such as the density of states (DOS), carrier density and some unique transport phenomena in graphene including quantum capacitance are reviewed to make the thesis complete and to serve as fundamentals for topics in later chapters. After a brief discussion on ballistic transport and universal conductivity in graphene, we study diffusive transport in graphene using the Boltzmann transport equation (BTE), first with linear Thomas Fermi screening, then with nonlinear Thomas Fermi screening. As an isotropic material, there is a relatively simple expression for the momentum relaxation time in graphene (compared to anisotropic materials). Due to the pseudo-spin characteristics of the Dirac Hamiltonian, the expression for the scattering matrix and thus the relaxation time in graphene is unique and special (compared to other 2DEG). In the linear Thomas Fermi section, the relaxation time expression can be either directly obtained from the BTE or using the differential scattering cross-section. Due to the rapid variation of the DOS near Dirac point, a self-consistent non-linear Thomas Fermi approach is used to model the screening effect more accurately. The potential energy for ionized impurity scattering is calculated in real space and Fourier space.

Topics on utilizing graphene as a potential spin channel material are discussed in Chapter 3. Intrinsic spin-orbit coupling (Dresselhaus term) and extrinsic Rashba spin-orbit coupling is now considered in the Dirac Hamiltonian, making it a 4x4 matrix. For intrinsic spin-orbit coupling, a band gap is opened and mirror symmetry (spin degeneracy) is still preserved. For Rashba spin-orbit interaction induced by a perpendicular electric field, the space symmetry is broken as a result of the pseudo-spin and real spin cross product, i.e. $(\vec{\sigma}\times\vec{s})_z$. Depending on the strength of the perpendicular electric field, Rashba interaction can be smaller, equivalent to, or larger than the intrinsic spin-orbit coupling, and hence the band gap (Dirac cone) can be opened or closed. When Rashba interaction dominates, ignoring the Dresselhaus term, the new eigenstate wave functions can be derived. Applying the non-linear Thomas Fermi screening, the ionized impurity scattering is calculated and discussed for both intra-band (c$\pm$ to c$\pm$) and inter-band (c$\pm$ to c$\mp$) scattering processes. For Rashba scattering, only intra-band scattering exists and an analytical expression is given. Back scattering is allowed for Rashba scattering. For a given impurity charge and location, Rashba scattering is much weaker than ionized impurity scattering. The spin injection, spin valve component and magnetoresistance are modeled using a 1D drift-diffusion device model. Spin current and MR for local and non-local transport models are discussed.

An emerging 2D material, black phosphorus (BP or phosphorene) is investigated in Chapter 4. In addition to promising electronic properties such as moderate direct band gap, high mobility of $10^3 \sim 10^4 cm^2 V^{-1} s^{-1}$ and good On/Off ratio for nanoelectronic applications, BP has high in-plane anisotropy due to its puckered crystal structure making it special among all emerging 2D materials. One of the initial motivations is to study the difference between effective mass anisotropy ratio (~7) and experimentally measured mobility anisotropy ratio (~1.6-4). Starting with a zero temperature case, we again adopt ionized impurity scattering as the scattering mechanism for the calculation. Since BP is a highly anisotropic material, we calculate the momentum relaxation time with an implicit integral equation derived from the BTE accounting for the full anisotropy of BP. The relaxation time in the integral equation can be explicitly written down through a matrix approach. Momentum relaxation time, mobility and anisotropy ratio are calculated and

discussed with dependence on carrier density, impurity distance and applied field direction. We find the numerically calculated anisotropy ratio (~3-4) is larger than experimental data. One of the reasons could be the experiments are done at finite temperatures, which leads to our later finite temperature calculation. The anisotropic electronic structure not only appears in the mobility difference along $\hat{x}$ and $\hat{y}$ directions for $T > 0$, but also leads to the momentum relaxation time and the polarizability being anisotropic with two-dimensional dependence on either incoming or scattering wave vectors. For finite temperature, scattering is no longer limited to the Fermi surface and polarizability/screening terms are temperature dependent. Competing with thermal excitation effect, screening is found to be dominating for $T < 100K$. As a result, mobility slowly decreases as temperature increases. The weak mobility dependence on temperature and anisotropy ratio of $1.9 - 3.5$, both match experimental measurements, indicating that ionized impurity scattering could be a significant mechanism in black phosphorus, at least in the low temperature region. Black phosphorus displays higher mobility anisotropy for smaller carrier density and lower temperature. The difference between isotropic and anisotropic transport phenomena can be understood by comparing Chapter 2 for graphene and Chapter 4 for black phosphorus. The calculation approaches developed in Chapter 4 can be employed to study other emerging anisotropic 2D materials.

5.2 Suggestions for future work

Up to now, 2D materials and "beyond silicon" solutions (spintronics, flexible electronics) are still under extensive research investigation in the nanotechnology community. Here we provide some suggestions for possible future research.

Our calculated graphene spin relaxation time $\sim 2ms$ is comparable to other theoretical predication, but to the best of our knowledge, all these calculations on spin life time are at least two orders of magnitude larger than experimental measurements. This

inconsistency still remains an open question. To explain such discrepancy of graphene spintronics, one may model the Hanle spin precession, where both electric and magnetic field are present.

For the electronic transport study on BP, we would like to include other scattering mechanism such as electron-phonon interaction, which can be an important scattering mechanism specially for high temperature (e.g. room temperature). To accommodate the electron-phonon interaction, the scattering matrix elements need to be rewritten, but the expression for the momentum relaxation time in Eq.4.2 considering the full anisotropy in BP remain the same. It would be easier (or sufficient) to start with the acoustic phonon interaction. One may also refer to other recent work on electron-phonon scattering limited BP transport.[152][153] In addition, utilizing the ultra thin body concept, 2D materials have been recently used a channel material for ultimate scaling beyond 7nm FinFET technology. Thus compact device modeling and simulation of 2D materials (based on first principles calculation) could be a desirable topic in the future.

Bibliography

[1] D. A. Dahl and L. J. Sham, *Phys. Rev. B* **16**, 651 (1977)

[2] F. Stern, *Phys. Rev. Lett*. **44**, 1469 (1980).

[3] T. Ando, A. B. Fowler, and F. Stern, *Rev. Mod. Phys*. **54**, 437 (1982).

[4] K. S. Novoselov, A. K. Geim, S. V. Morozov, D. Jiang, Y. Zhang, S. V. Dubonos, I. V. Grigorieva, and A. A. Firsov, *Science* **306**, 666 (2004).

[5] A. K. Geim, and K. S. Novoselov, *Nat. Mater*. **6**, 183 (2007).

[6] K. S. Novoselov, D. Jiang, F. Schedin, T. J. Booth, V. V. Khotkevich, S. V. Morozov, and A. K. Geim, Proc. Natl. Acad. Sci. U.S.A. 102, 10 451 (2005)

[7] A. H. Castro Neto, F. Guinea, N. M. R. Peres, K. S. Novoselov, and A. K. Geim, *Rev. Mod. Phys*. **81**, 109 (2009).

[8] R. Mas-Balleste, C. Gomez-Navarro, J. Gomez-Herrero, and F. Zamora, *Nanoscale* **3**, 20 (2011).

[9] S. Bae, H. Kim, Y. Lee, X. Xu, J.-S. Park, et al. *Nat. Nanotechnol*. **5**, 574 (2010).

[10] H. Jang, Y. J. Park, X. Chen, T. Das, M.-S. Kim, and J.-H. Ahn, *Adv. Mater*. **28**, 4184 (2016).

[11] C.-C. Lu, Y.-C. Lin, C.-H. Yeh, J.-C. Huang, and P.-W. Chiu, *ACS Nano* **6**, 4469 (2012).

[12] S. J. Kim, K. Choi, B. Lee, Y. Kim, and B. H. Hong, *Annu. Rev. Mater. Res*. **45**, 63 (2015).

[13] S. Datta, and B. Das, *Appl. Phys. Lett*. **56**, 665 (1990)

[14] I. Zutic, J. Fabian, and S. Das Sarma, *Rev. Mod. Phys*. **76**, 323 (2004)

[15] H. Dery, H. Wu, B. Ciftcioglu, M. Huang, Y. Song, R. Kwakami, J. Shi, I. Krivorotov, I. Zutic, and L. J. Sham, *IEEE Trans. Electron Dev*. **59**, 259 (2012)

[16] N. Tombros, C. Jozsa, M. Popinciuc, H. T. Jonkman, and B.J. van Wees, *Nature*, **448**, 571 (2007)

[17] T.-Y. Yang, J. Balakrishnan, F. Volmer, A. Avsar, M. Jaiswal, J. Samm, S. R. Ali, A. Pachoud, M. Zeng, M. Popinciuc, G. Güntherodt, B. Beschoten, and B. Özyilmaz, *Phys. Rev. Lett*. **107**, 047206 (2011)

[18] W. Han, J.-R. Chen, D. Wang, K. M. McCreary, H. Wen, A. G. Swartz, J. Shi, and R. K. Kawakami, *Nano Lett*. **12**, 3443 (2012).

[19] M. V. Kamalakar, C. Groenveld, A. Dankert, and S. P. Dash, *Nat. Commun*. **6**, 6766 (2015).

[20] K. F. Mak, C. Lee, J. Hone, J. Shan, and T. F. Heinz, *Phys. Rev. Lett*. **105**, 136805 (2010).

[21] J. N. Coleman, M. Lotya, A. O'Neill, S. D. Bergin, P. J. King, U. Khan, K. Young, A. Gaucher, S. De, R. J. Smith, I. V. Shvets, S. K. Arora, G. Stanton, H. Y. Kim, K. Lee, G. T. Kim, G. S. Duesberg, T. Hallam, J. J. Boland, J. J. Wang, J. F. Donegan, J. C. Grunlan, G. Moriarty, A. Shmeliov, R. J. Nicholls, J. M. Perkins, E. M. Grieveson, K. Theuwissen, D. W. McComb, P. D. Nellist and V. Nicolosi, *Science* **331**, 568 (2011).

[22] B. Radisavljevic, A. Radenovic, J. Brivio, V. Giacometti and A. Kis, *Nat. Nanotechnol*. **6**, 147 (2011).

[23] H. Liu, A. T. Neal, Z. Zhu, D. Tomanek, and P. D. Ye, *ACS Nano* **8**, 4033 (2014).

[24] L. Li, Y. Yu, G. J. Ye, Q. Ge, X. Ou, H. Wu, D. Feng, X. H. Chen, and Y. Zhang, *Nat. Nanotechnol.* **9**, 372 (2014).

[25] X. Ling, H. Wang, S. Huang, F. Xia, and M. S. Dresselhaus, *Proc. Natl. Acad. Sci. U.S.A.* **112**, 4523 (2015).

[26] A. Splendiani, L. Sun, Y. Zhang, T. Li, J. Kim, C. Y. Chim, G. Galli and F. Wang, *Nano Lett*. **10**, 1271 (2010).

[27] K. F. Mak, K. He, J. Shan and T. F. Heinz, *Nat. Nanotechnol*. **7**, 494 (2010).

[28] D. Xiao, G. B. Liu, W. X. Feng, X. D. Xu and W. Yao, *Phys. Rev. Lett*. **108**, 196802 (2012).

[29] H. Fang, S. Chuang, T. C. Chang, K. Takei, T. Takahashi, A. Javey, *Nano Lett*. 12, 3788 (2012).

[30] W. Cao, J. Kang, D. Sarkar, W. Liu, and K. Banerjee, *IEEE Trans. Electron Dev*. **62**, 345 (2015)

[31] Y. S. Chauhan, D. D. Lu, V. Sriramkumar, S. Khandelwal, J. P. Duarte, N. Payvadosi, A. Niknejad, and C. Hu, *FinFET Modeling for IC Simulation and Design: Using the BSIM-CMG Standard*, Elsevier (2015).
[32] Intel's FinFET Transistors Increase Microprocessor Speed, *New York Time*, May 4 2011
[33] Samsung and GLOBALFOUNDRIES Forge Strategic Collaboration to Deliver Multi-Sourced Offering of 14nm FinFET Semiconductor Technology, (http://www.globalfoundries.com/newsroom/press-releases/2014/04/17/samsung-and-globalfoundries-forge-strategic-collaboration-to-deliver-multi-sourced-offering-of-14nm-finfet-semiconductor-technology)
[34] M.-C. Chen, K.-S. Li, L.-J. Li, A.-Y. Lu , M.-Y. Li, Y.-H. Chang, C.-H. Lin, A. B. Sachid, T. Wang, F. -L. Yang, C. Hu, *IEEE International Electron Devices Meeting (IEDM)*, 32.2.1, (2015).
[35] S. B. Desai, S. R. Madhvapathy, A. b. Sachid, J. P. Llinas, Q. Wang, G. H. Ahn, G. Pitner, M. J. Kim, J. Bokor, C. Hu, H.-S. P. Wong, and A. Javey, *Science*, **354**, 99 (2016)
[36] R. J. Wu, M. Topsakal, T. Low, M. C. Robbins, N. Haratipour, J. S. Jeong, R. M. Wentzcovitch, S. J. Koester, and K. A. Mkhoyan, *J. Vac. Sci. Technol. A,* **33**, 060604 (2015).
[37] F. Xia, H. Wang, and Y. Jia, *Nat. Commun* **5**, 4458 (2014).
[38] T. Low, R. Roldan, H. Wang, F. Xia, P. Avouris, L. M.Moreno and F. Guinea, *Phys. Rev. Lett.* **113**, 106802(2014).
[39] R. Fei, A. Faghaninia, R. Soklaski, J.-A. Yan, C. Lo, and L. Yang, *Nano Lett*. **14**, 6393 (2014).
[40] B. Liao, J. Zhou, B. Qiu, M. S. Dresselhaus, and G. Chen, *Phys. Rev. B* **91**, 235419 (2015).
[41] J.-W. Jiang, and H. S. Park, *Nat. Commun*. **6**, 4727 (2014).
[42] Y. Du, J. Maassen, W. Wu, Z. Luo, X. Xu, and P. D. Ye, *Nano Lett*. **16**, 6701 (2016).
[43] S. Das Sarma, S. Adam, E. H. Hwang, and E. Rossi, *Rev. Mod. Phys*. **83**, 407 (2011).

[44] A. Goswami, *Master Thesis: Electron Spin-flip Scattering in Graphene due to Substrate Impuirty*, University of Minnesota (2013).

[45] H.-S. P. Wong, and D. Akinwande, *Carbon Nanotube and Graphene Device Physics*, Cambridge University Press (2011).

[46] M. I. Katsnelson, *Graphene: Carbon in Two Dimensions*, Cambridge University Press (2012).

[47] T. Ando, *NPG Asia Mater*., **1**, 17 (2009).

[48] M. I. Katsnelson, K. S. Novoselov, and A. K. Geim, *Nature Phys*. **2**, 620 (2006).

[49] T. Low and J. Appenzeller, *Phys. Rev. B* **80**, 155406 (2009).

[50] E. Rossi, J. H. Bardarson, P. W. Brouwer, and S. Das Sarma, *Phys. Rev. B* **81**, 121408(R) (2010).

[51] A. V. Shytov, M. S. Rudner, and L. S. Levitov, *Phys. Rev. Lett*. **101**, 156804 (2008).

[52] E. B. Sonin, *Phys. Rev. B*. **79**, 195438 (2009).

[53] N. Stander, B. Huard, and D. Goldhaber-Gordon, *Phys. Rev. Lett*. **102**, 026807 (2009).

[54] A. F. Young and P. Kim, *Nature Phys*. **5**, 222 (2009).

[55] S. Adam, E. H. Hwang, V. M. Galitski, and S. Das Sarma, *Proc. Natl. Acad. Sci. U.S.A*. **104**, 18 392 (2007).

[56] K. Nomura and A. H. MacDonald, *Phys. Rev. Lett*. **96**, 256602 (2006).

[57] E. H. Hwang, S. Adam, and S. Das Sarma, *Phys. Rev. Lett*. **98**, 186806 (2007).

[58] J. Martin, N. Akerman, G. Ulbricht, T. Lohmann, J. H. Smet, K. von Klitzing, and A. Yacoby, *Nature Phys*. **4**, 144 (2008).

[59] Y. Zhang, Y.-W. Tan, H. L. Stormer, and P. Kim, *Nature* **438**, 201 (2005).

[60] K. S. Novoselov, Z. Jiang, Y. Zhang, S. V. Morozov, H. L. Störmer, U. Zeitler, J. C. Maan, G. S. Boebinger, P. Kim, and A. K. Geim, *Science* **315**, 1379 (2007).

[61] B. Özyilmaz, P. Jarillo-Herrero, D. Efetov, D. A. Abanin, L. S. Levitov, and P. Kim, *Phys. Rev. Lett*. **99**, 166804 (2007).

[62] L. Sheng, D. N. Sheng, F. D. M. Haldane, and L. Balents, *Phys. Rev. Lett*. **99**, 196802 (2007).

[63] K. I. Bolotin, F. Ghahari, M. D. Shulman, H. L. Stormer, and P. Kim, *Nature* **462**, 196 (2009).

[64] J. R. Williams, L. DiCarlo, and C. M. Marcus, *Science* **317**, 638 (2007).

[65] C. Beenakker, *Rev. Mod. Phys*. **80**, 1337 (2008).

[66] M. O. Goerbig, *Rev. Mod. Phys*. **83**, 1193 (2011).

[67] V. N. Kotov, B. Uchoa, V. M. Pereira, A. H. C. Neto, and F. Guinea, *Rev. Mod. Phys*. **84**, 1067 (2012).

[68] X. Wang, Y. Ouyang, X. Li, H. Wang, J. Guo, and H. Dai, *Phys. Rev. Lett*. **100**, 206803 (2008).

[69] T. Fang, A. Konar, H. L. Xing, and D. Jena, *Appl. Phys. Lett*. **91**, 092109 (2007).

[70] J. L. Xia, F. Chen, J. H. Li, and N. J. Tao, *Nature Nanotech*. **4**, 505 (2009).

[71] L. Ponomarenko, R. Yang, R. V. Gorbachev, P. Blake, A. S. Mayorov, K. S. Novoselov, M. I. Katsnelson, and A. K. Geim, *Phys. Rev. Lett*. **105**, 136801 (2010).

[72] J. Tworzydlo, B. Trauzettel, M. Titov, A. Rycerz, and C. W. J. Beenakker, *Phys. Rev. Lett.* **96**, 246802 (2006).

[73] M. M. Fogler, F. Guinea, and M. I. Katsnelson, *Phys. Rev. Lett*. **101**, 226804 (2008).

[74] M. Müller, M. Bräuninger, and B. Trauzettel, *Phys. Rev. Lett*. **103**, 196801 (2009).

[75] A. Schuessler, P. M. Ostrovsky, I. V. Gornyi, and A. D. Mirlin, *Phys. Rev. B* **79**, 075405 (2009).

[76] L. M. Zhang and M. M. Fogler, *Phys. Rev. Lett*. **100**, 116804 (2008).

[77] S. Ryu, C. Mudry, A. Furusaki, and A. W. W. Ludwig, *Phys. Rev. B* **75**, 205344 (2007).

[78] Mark Lundstrom, *Fundamentals of Carrier Transport 2nd Edition*, Cambridge University Press (2009).

[79] C. D. Cress, J. J. McMorrow, J. T. Robinson, B. J. Landi, S. M. Hubbard, and S. R. Messenger, *Electronics* 1, 23 (2012).

[80] F. Miao, S. Wijeratne, Y. Zhang, U. C. Coskun, W. Bao, and C. N. Lau, *Science* **317**, 1530 (2007).

[81] R. Danneau, F. Wu, M. F. Craciun, S. Russo, M. Y. Tomi, J. Salmilehto, A. F. Morpurgo, and P. J. Hakonen, *Phys. Rev. Lett*. **100**, 196802 (2008).

[82] C. Jacoboni, *Theory of Electron Transport in Semiconductors*, Springer (2010).
[83] D. J. Griffiths, *Introduction to Quantum Mechanics 2nd Edition*, Pearson Prentice Hall (2004).
[84] R. Shankar, *Principles of Quantum Mechanics 2nd Edition*, Plenum Press (1994).
[85] D. S. Novikov, *Phys. Rev. B* **76**, 245435 (2007).
[86] A. Messiah, *Quantum Mechanics*, Dover Publication (1962).
[87] Y. Liu, A. Goswami, F. Liu, D. L. Smith and P. P. Ruden, *J. Appl. Phys.* **116**, 234301 (2014).
[88] A. Goswami, Y. Liu, F. Liu, P. P. Ruden, and D. L. Smith, *MRS Proc*. **1505**, mrsf12-1505-w10-12 (2013).
[89] Minnesota Supercomputing Institute, https://www.msi.umn.edu
[90] S. S. P. Parkin, *Annu. Rev. Mater. Res*. **25**, 357 (1995).
[91] H. N. Bertram, *Theory of Magnetic Recording*, Cambridge University Press, (1994).
[92] J. Kim, A. Paul, P. Crowell, S. J. Koester, S. S. Sapatnekar, J.-P. Wang, and C. H. Kim, *Proc. IEEE* **103**, 106 (2015).
[93] B. Behin-Aein, D. Datta, S. Salahuddin, and S. Datta, *Nat. Nanotechnol*. **5**, 266 (2010).
[94] B. Behin-Aein, A. Sarkar, S. Srinivasan, and S. Datta, *Appl. Phys. Lett*. **98**, 123510 (2011).
[95] Y. Anugrah, Doctoral Dissertation, University of Minnesota (2016).
[96] K. L. Wang, J. G. Alzate, and P. K. Amiri, *J. Phys. D, Appl. Phys*. **46**, 074003 (2013).
[97] T. Kawahara, K. Ito, R. Takemura, and H. Ohno, *Microelectron. Reliab.* **52**, 613 (2012).
[98] J. S. Meena, S. M. Sze, U. Chand, and T. Y. Tseng, *Nanoscale Res. Lett*. **9**, 526 (2014).
[99] W. Han, R. K. Kawakami, M. Gmitra, and J. Fabian, *Nat. Nanotechnol*. **9**, 794 (2014).
[100] Y. A. Bychkov and E. I. Rashba, *JETP Lett*. **39**, 78 (1984).
[101] F. Liu, Y. Liu, D. L. Smith, and P. P. Ruden, *IEEE Trans. Electron Dev.* **62**, 3426 (2015).

[102] F. Liu, Y. Liu, J. Hu, D. L. Smith, and P. P. Ruden, *J. Appl. Phys.* **114**, 093708 (2013).

[103] H. Min, J. E. Hill, N. A. Sinitsyn, B. R. Sahu, L. Kleinman, and A. H. MacDonald, *Phys. Rev. B* **74**, 165310 (2006).

[104] D. Huertas-Hernando, F. Guinea, and A. Brataas, *Phys. Rev. Lett*. **103**, 146801 (2009).

[105] S. Konschuh, M. Gmitra, and J. Fabian, *Phys. Rev. B* **82**, 245412 (2010).

[106] E. V. Castro, H. Ochoa, M. I. Katsnelson, R. V. Gorbachev, D. C. Elias, K. S. Novoselov, A. K. Geim, and F. Guinea, *Phys. Rev. Lett*. **105**, 266601 (2010).

[107] E. Pallecchi, F. Lafont, V. Cavaliere, F. Schopfer, D. Mailly, W. Poirier, and A. Ouerghi, *Sci. Rep*. **4**, 4558 (2014).

[108] T. Maassen, J. J. van den Berg, N. IJbema, F. Fromm, T. Seyller, R. Yakimova, and B. J. van Wees, *Nano Lett*. **12**, 1498 (2012).

[109] A. H. Castro Neto and F. Guinea, *Phys. Rev. Lett*. **103**, 026804 (2009).

[110] G. A. Prinz, *Science*, **282**, 1660 (1998).

[111] W. Han, K. Pi, K. M. McCreary, Y. Li, Jared J. I. Wong, A. G. Swartz, and R. K. Kawakami, *Phys. Rev. Lett*. **105**, 167202 (2010).

[112] Y. Ji, A. Hoffmann, J. S. Jiang, J. E. Pearson, and S. D. Bader, *J. Phys. D, Appl. Phys.* **40**, 1280 (2007).

[113] C. Józsa, M. Popinciuc, N. Tombros, H. T. Jonkman, and B. J. van Wees, *Phys. Rev. Lett.*, **100**, 236603, (2008).

[114] F. J. Jedema, A. T. Filip, and B. J. van Wees, *Nature* **410**, 345 (2001).

[115] Y. Fukuma, L. Wang, H. Idzuchi, S. Takahashi, S. Maekawa, and Y. Otani, *Nature Mater.* **10**, 527 (2011).

[116] T. Kimura, Y. Otani, and J. Hamrle, *Phys. Rev. Lett.* **96**, 037201 (2006).

[117] F. Casanova, A. Sharoni, M. Erekhinsky, and I. K. Schuller, *Phys. Rev. B* **79**, 184415 (2009).

[118] E. I. Rashba, *Phys. Rev. B* **62**, R16267 (2000).

[119] D. L. Smith and R. N. Silver, *Phys. Rev. B* **64**, 045323 (2001).

[120] S. Luryi, *Appl. Phys. Lett.*, **52**, 501 (1988).

[121] V.S. Bagotsky, *Fundamentals of Electrochemistry*, Willey, (2006).

[122] W. Han and R. K. Kawakami, *Phys. Rev. Lett.*, **107**, 047207 (2011).

[123] Z. G. Yu and M. E. Flatté, *Phys. Rev. B*, **66**, 235302 (2002).

[124] M. Yunus, P. P. Ruden, and D. L. Smith, *J. Appl. Phys.*, **103**, 103714 (2008).

[125] J. Bardeen, *Phys. Rev. Lett.*, **6**, 57 (1961).

[126] J. Tersoff and D. R. Hamann, *Phys. Rev. B* **31**, 805 (1985).

[127] T. Valet and A. Fert, *Phys. Rev. B* **48**, 7099 (1993).

[128] M. Julliere, *Phys. Lett. A*, **54**, 225 (1975).

[129] S. Takahashi and S. Maekawa, *Phys. Rev. B* **67**, 052409 (2003).

[130] R. N. Mahato et al., *Science* **341**, 257 (2013).

[131] J. S. Moodera, L. R. Kinder, T. M. Wong, and R. Meservey, *Phys. Rev. Lett.*, **74**, 3273 (1995).

[132] C. Barraud et al, *Nature Phys.*, **6**, 615 (2010).

[133] T. Low, A. S. Rodin, A. Carvalho, Y. Jiang, H. Wang, F. Xia, and A. H. Castro Neto, *Phys. Rev. B* **90**, 075434 (2014).

[134] J. Qiao, X. Kong, Z.-X. Hu, F. Yang, and W. Ji, *Nat. Commun.* **5**, 4475 (2014).

[135] V. Tran, R. Soklaski, Y. Liang, and L. Yang, *Phys. Rev. B* **89**, 235319 (2014).

[136] S.-I. Narita, S.-I. Terada, S. Mori, K. Muro, Y. Akahama, and S. Endo, *J. Phys. Soc. Jpn.* **52**, 3544 (1983).

[137] A. S. Rodin, A. Carvalho, and A. H. Castro Neto, *Phys. Rev. Lett.* **112**, 176801 (2014).

[138] M. V. Fischetti, Z. Ren, P. M. Solomon, M. Yang, and K. Rim, *J. Appl. Phys.* **94**, 1079 (2003).

[139] H. Liu, Y. Du, Y.Deng, and P. D. Ye, *Chem. Soc. Rev*. **44**, 2732 (2015).

[140] M. V. Fischetti, *J. Appl. Phys*. **89**, 1232 (2001).

[141] A. Mishchenko,Y. Cao, G. L.Yu, C. R.Woods, R.V.Gorbachev, K. S. Novoselov, A. K. Geim, and L. S. Levitov, *Nano Lett*. **15**, 6991 (2015).

[142] P. F. Maldague, *Surf. Sci*. **73**, 296 (1978).

[143] Z. -Y. Ong, G. Zhang and Y. W. Zhang, *J. Appl. Phys*. **116**, 214505 (2014).

[144] R. F. Pierret, *Advanced Semiconductor Fundamentals 2nd Edition*, Pearson Education, (2002).

[145] Y. Liu, T. Low, and P. P. Ruden, *Phys. Rev. B* **93**, 165402 (2016).

[146] S. Tongay, H. Sahin, C. Ko, A. Luce, W. Fan, K. Liu, J. Zhou, Y.-S. Huang, C.-H. Ho, J. Yan, D. F. Ogletree,S. Aloni, J. Ji, S. Li, J. Li, F. M. Peeters, and J. Wu, *Nat. Commun.* **5**, 3252 (2014).

[147] S. Yang, C. Wang, H. Sahin, H. Chen, Y. Li, S.-S. Li, A. Suslu, F. M. Peeters, Q. Liu, J. Li, and S. Tongay, *Nano. Lett.* **15**, 1660 (2015).

[148] D. A. Chenet, O. B. Aslan, P. Y. Huang, C. Fan, A. M. van der Zande, T. F. Heinz, and J. C. Hone, *Nano Lett*. **15**, 5667 (2015).

[149] J. O. Island, M. Buscema, M. Barawi, J. M. Clamagirand, J. R. Ares, C. Snchez, I. J. Ferrer, G. A. Steele, H. S. J. van der Zant, and A. Castellanos-Gomez, *Adv. Opt. Mat.* **2**, 641 (2014).

[150] J. Dai and X. C. Zeng, *Angew. Chem.* **127**, 7682 (2015).

[151] J. Kang, H. Sahin, H. D. Ozaydin, R. T. Senger, and F. M. Peeters, *Phys. Rev. B* **92**, 075413 (2015).

[152] B. Liao, J. Zhou, B. Qiu, M. S. Dresselhaus, and G. Chen, *Phys. Rev. B* **91**, 235419 (2015).

[153] A. N. Rudenko, S. Brener, and M. I. Katsnelson, *Phys. Rev. Lett*. **116**, 246401 (2016).

Appendix

A Isotropic and anisotropic relaxation time derivation

Starting from the Boltzmann transport equation (BTE) for a general anisotropic material within relaxation time approximation,

$$\frac{\partial f}{\partial t}+\vec{v}\cdot\nabla_{\vec{r}}f-\frac{e\vec{\xi}}{\hbar}\cdot\nabla_{\vec{k}}f=\left(\frac{\partial f}{\partial t}\right)_{scatter}=-\frac{f(\vec{k})-f_0(\vec{k})}{\tau(\vec{k})} \qquad (A1)$$

In a stationary state and assuming no $\vec{r}$ dependence

$$-\frac{e\vec{\xi}}{\hbar}\cdot\nabla_{\vec{k}}f=-\frac{f(\vec{k})-f_0(\vec{k})}{\tau(\vec{k})} \qquad (A2)$$

$$f(\vec{k})=f_0(\vec{k})+\frac{e}{\hbar}[\vec{\xi}\cdot\nabla_{\vec{k}}f(\vec{k})]\tau(\vec{k}) \qquad (A3)$$

Restricting the calculation to linear response, $f(\vec{k})$ is replaced by $f_0(\vec{k})$ in the second term of Eq. A3

$$f(\vec{k})=f_0(\vec{k})+\frac{e}{\hbar}[\vec{\xi}\cdot\nabla_{\vec{k}}f_0(\vec{k})]\tau(\vec{k}) \qquad (A4)$$

Assuming the scattering is elastic, $P_{\vec{k},\vec{k}'}=P_{\vec{k}',\vec{k}}$, the detailed balance equation becomes

$$\left(\frac{\partial f}{\partial t}\right)_{scatter}=\frac{1}{A}\sum_{\vec{k}'}P_{\vec{k},\vec{k}'}\{[1-f(\vec{k})]P_{\vec{k},\vec{k}'}f(\vec{k}')-[1-f(\vec{k}')]P_{\vec{k}',\vec{k}}f(\vec{k})\}$$

$$=\frac{1}{A}\sum_{\vec{k}'}P_{\vec{k},\vec{k}'}[f(\vec{k}')-f(\vec{k})] \qquad (A5)$$

Substituting Eq. A5 with Eq. A1 and Eq. A2,

$$-\frac{e\vec{\xi}}{\hbar}\cdot\nabla_{\vec{k}}f_0(\vec{k})=\frac{1}{A}\sum_{\vec{k}'}P_{\vec{k},\vec{k}'}\left\{f_0(\vec{k}')+\frac{e}{\hbar}[\vec{\xi}\cdot\nabla_{\vec{k}}f_0(\vec{k}')]\tau(\vec{k}')-f_0(\vec{k})-\frac{e}{\hbar}[\vec{\xi}\cdot\nabla_{\vec{k}}f_0(\vec{k})]\tau(\vec{k})\right\}$$

$$=\frac{1}{A}\sum_{\vec{k}'}P_{\vec{k},\vec{k}'}\left\{\frac{e}{\hbar}[\vec{\xi}\cdot\nabla_{\vec{k}'}f_0(\vec{k}')]\tau(\vec{k}')-\frac{e}{\hbar}[\vec{\xi}\cdot\nabla_{\vec{k}}f_0(\vec{k})]\tau(\vec{k})\right\} \qquad (A6)$$

which is equivalent to,

$$-\frac{e\vec{\xi}}{\hbar}\cdot\nabla_{\vec{k}}f_0(\vec{k}) = \frac{e}{\hbar}\left[\vec{\xi}\cdot\nabla_{\vec{k}}f_0(\vec{k})\right]\tau(\vec{k})\frac{1}{A}\sum_{\vec{k}'}P_{\vec{k},\vec{k}'}\left[\frac{\frac{e}{\hbar}\left[\vec{\xi}\cdot\nabla_{\vec{k}'}f_0(\vec{k}')\right]\tau(\vec{k}')}{\frac{e}{\hbar}\left[\vec{\xi}\cdot\nabla_{\vec{k}}f_0(\vec{k})\right]\tau(\vec{k})}-1\right] \quad (A7)$$

or,

$$\frac{1}{\tau(\vec{k})} = \frac{1}{A}\sum_{\vec{k}'}P_{\vec{k},\vec{k}'}\left\{1-\frac{\left[\vec{\xi}\cdot\nabla_{\vec{k}'}E(\vec{k}')\frac{\partial f_0(\vec{k}')}{\partial E}\right]\tau(\vec{k}')}{\left[\vec{\xi}\cdot\nabla_{\vec{k}}E(\vec{k})\frac{\partial f_0(\vec{k})}{\partial E}\right]\tau(\vec{k})}\right\} \quad (A8)$$

with $\vec{v}(\vec{k}) = \frac{1}{\hbar}\nabla_{\vec{k}}E(\vec{k})$ and $\sum_{\vec{k}_j} = \frac{A}{(2\pi)^2}\int d^2\vec{k}_j$ for a 2DEG (factor A cancels out through $P_{\vec{k},\vec{k}'}$), we recover anisotropic relaxation time (i.e. Eq. 4.2) as

$$\frac{1}{\tau_m(\hat{\xi},\vec{k}_i)} = \frac{1}{(2\pi)^2}\int_{all\,\vec{k}_j} d^2\vec{k}_j\, P_{\vec{k}_i,\vec{k}_j}\left\{1-\frac{\left[\hat{\xi}\cdot\vec{v}(\vec{k}_j)\right]\tau_m(\hat{\xi},\vec{k}_j)}{\left[\hat{\xi}\cdot\vec{v}(\vec{k}_i)\right]\tau_m(\hat{\xi},\vec{k}_i)}\right\} \quad (A9)$$

For isotropic material, $m_{xx} = m_{yy}$, the two terms $\tau_m(\hat{\xi},\vec{k}_j)$ and $\tau_m(\hat{\xi},\vec{k}_i)$ inside the integral cancel. $1-\frac{\hat{\xi}\cdot\vec{v}(\vec{k}_j)}{\hat{\xi}\cdot\vec{v}(\vec{k}_i)}$ reduces to $1-cos\theta_{ij}$, Eq. A9 become following explicit integral

$$\frac{1}{\tau_{iso}} = \frac{1}{(2\pi)^2}\int_{all\,\vec{k}_j} d^2\vec{k}_j\, P_{\vec{k}_i,\vec{k}_j}\left(1-cos\theta_{ij}\right) \quad (A10)$$

we thus recover Eq. 2.50 used in graphene diffusive transport discussion. Please notice this Appendix A serves as reference for both graphene (Chapter 2) and BP (Chapter 4) diffusive transport. We start with anisotropic transport derivation from BTE, then the isotropic transport with relaxation time approximation can be simplified from general expression.

B Potential and Rashba scattering cross-sections

Without the spin-orbit interaction, the low-energy graphene Hamiltonian, H_0, can be written as

$$H_0 = \hbar v_F \begin{bmatrix} 0 & k_x + ik_y & 0 & 0 \\ k_x - ik_y & 0 & 0 & 0 \\ 0 & 0 & 0 & k_x + ik_y \\ 0 & 0 & k_x - ik_y & 0 \end{bmatrix} \qquad (B.1)$$

In this 4x4 matrix, rows/columns 1,2 refer to spin up and rows/columns 3,4 refer to spin down. Diagonalizing H_0, two degenerated states with energy eigenvalue $E_c(\vec{k}) = \hbar v_F |\vec{k}|$ can be written as:

$$\langle \vec{r} | c1, \vec{k} \rangle = \frac{1}{2} \begin{pmatrix} 1 \\ e^{i\theta_{\vec{k}}} \\ ie^{i\theta_{\vec{k}}} \\ ie^{2i\theta_{\vec{k}}} \end{pmatrix} e^{i\vec{k}\cdot\vec{r}}, \qquad \langle \vec{r} | c2, \vec{k} \rangle = \frac{1}{2} \begin{pmatrix} 1 \\ e^{i\theta_{\vec{k}}} \\ -ie^{i\theta_{\vec{k}}} \\ -ie^{2i\theta_{\vec{k}}} \end{pmatrix} e^{i\vec{k}\cdot\vec{r}} \qquad (\mathrm{B.2a})$$

The other two degenerated states with energy eigenvalue $E_v(\vec{k}) = -\hbar v_F |\vec{k}|$ for holes are:

$$\langle \vec{r} | v1, \vec{k} \rangle = \frac{1}{2} \begin{pmatrix} 1 \\ -e^{i\theta_{\vec{k}}} \\ -ie^{i\theta_{\vec{k}}} \\ ie^{2i\theta_{\vec{k}}} \end{pmatrix} e^{i\vec{k}\cdot\vec{r}}, \qquad \langle \vec{r} | v2, \vec{k} \rangle = \frac{1}{2} \begin{pmatrix} 1 \\ -e^{i\theta_{\vec{k}}} \\ ie^{i\theta_{\vec{k}}} \\ -ie^{2i\theta_{\vec{k}}} \end{pmatrix} e^{i\vec{k}\cdot\vec{r}} \qquad (\mathrm{B.2b})$$

Considering the Rashba interaction term R_0, the system symmetry is broken, and the total graphene Hamiltonian H and four eigenstates $|c\pm, \vec{k}\rangle$ and $|v\pm, \vec{k}\rangle$ are given in the Eq. 3.9a and 3.9b of the main text. These eigenstates are linear combinations of the eigenstates of H_0 : $|c1, \vec{k}\rangle$, $|c2, \vec{k}\rangle$, $|v1, \vec{k}\rangle$ and $|v2, \vec{k}\rangle$

$$|c+, \vec{k}\rangle = \frac{1}{\sqrt{2} \cdot \sqrt{1 + {b_{c+}}^2}} \left[(1 + b_{c+}) |c1, \vec{k}\rangle + (1 - b_{c+}) |v1, \vec{k}\rangle \right] \qquad (B.3a)$$

$$|c-, \vec{k}\rangle = \frac{1}{\sqrt{2} \cdot \sqrt{1 + {b_{c-}}^2}} \left[(1 + b_{c-}) |c2, \vec{k}\rangle + (1 - b_{c-}) |v2, \vec{k}\rangle \right] \qquad (B.3b)$$

$$|v+, \vec{k}\rangle = \frac{1}{\sqrt{2} \cdot \sqrt{1 + {b_{v+}}^2}} \left[(1 + b_{v+}) |c1, \vec{k}\rangle + (1 - b_{v+}) |v1, \vec{k}\rangle \right] \qquad (B.3c)$$

$$|v-, \vec{k}\rangle = \frac{1}{\sqrt{2} \cdot \sqrt{1 + {b_{v-}}^2}} \left[(1 + b_{v-}) |c2, \vec{k}\rangle + (1 - b_{v-}) |v2, \vec{k}\rangle \right] \qquad (B.3d)$$

$b_{c\pm}$ and $b_{v\pm}$ are defined in the Chapter 3.

For the states represented in Eq. B.2a and B.2b, the scattering matrices from $\vec{k}$ to $\vec{k}'$ under the action of the potential $U(r)$ are calculated as follows (taking $\langle c1,\vec{k}'|U(r)|c1,\vec{k}\rangle$ as an example)

$$\langle c1,\vec{k}'|U(r)|c1,\vec{k}\rangle = \frac{1}{4}\left\langle (1 \quad e^{-i\theta_{\vec{k}'}} \quad -ie^{-i\theta_{\vec{k}'}} \quad -ie^{-2i\theta_{\vec{k}'}})e^{-i\vec{k}'\cdot\vec{r}} \middle| U(r) \middle| \begin{pmatrix} 1 \\ e^{i\theta_{\vec{k}}} \\ ie^{i\theta_{\vec{k}}} \\ ie^{2i\theta_{\vec{k}}} \end{pmatrix} e^{i\vec{k}\cdot\vec{r}} \right\rangle$$

$$= \frac{1}{4}[\left\langle e^{-i\vec{k}'\cdot\vec{r}} \middle| U(r) \middle| e^{i\vec{k}\cdot\vec{r}} \right\rangle + \left\langle e^{-i\theta_{\vec{k}'}}\cdot e^{-i\vec{k}'\cdot\vec{r}} \middle| U(r) \middle| e^{i\theta_{\vec{k}}}\cdot e^{i\vec{k}\cdot\vec{r}} \right\rangle$$

$$+ \left\langle e^{-i\theta_{\vec{k}'}}\cdot e^{-i\vec{k}'\cdot\vec{r}} \middle| U(r) \middle| e^{i\theta_{\vec{k}}}\cdot e^{i\vec{k}\cdot\vec{r}} \right\rangle + \left\langle e^{-2i\theta_{\vec{k}'}}\cdot e^{-i\vec{k}'\cdot\vec{r}} \middle| U(r) \middle| e^{2i\theta_{\vec{k}}}\cdot e^{i\vec{k}\cdot\vec{r}} \right\rangle]$$

$$= \frac{1}{4}\left(1 + 2e^{-i\theta} + e^{-2i\theta}\right)\int d^2\vec{r}\, e^{-i\vec{q}\cdot\vec{r}}U(r) = \frac{1}{4}\left(1 + e^{-i\theta}\right)^2\widehat{U}(q) \qquad (B.9)$$

By a similar method, it can be shown that,

$$\langle v1,\vec{k}'|U(r)|v1,\vec{k}\rangle = \langle c1,\vec{k}'|U(r)|c1,\vec{k}\rangle = \frac{1}{4}\left(1 + e^{-i\theta}\right)^2\widehat{U}(q) \quad (B.10a)$$

$$\langle v1,\vec{k}'|U(r)|c1,\vec{k}\rangle = \langle c1,\vec{k}'|U(r)|v1,\vec{k}\rangle = \frac{1}{4}\left(1 - e^{-i\theta}\right)^2\widehat{U}(q) \quad (B.10b)$$

For eigenstates Eq. 3.9a and 3.9b of the main text, the scattering matrix elements with respect to potential $U(r)$ for intra-band scattering can be written as,

$$\langle c+,\vec{k}'|U(r)|c+,\vec{k}\rangle$$

$$= \frac{1}{2\left(1 + {b_{c+}}^2\right)}\left\langle (1 + b_{c+})\langle c1,\vec{k}'| + (1 - b_{c+})\langle v1,\vec{k}'| \middle| U(r) \middle| (1 + b_{c+})|c1,\vec{k}\rangle + (1 - b_{c+})|v1,\vec{k}\rangle \right\rangle$$

$$= \frac{1}{2\left(1 + {b_{c+}}^2\right)}[(1 + b_{c+})^2\langle c1,\vec{k}'|U(r)|c1,\vec{k}\rangle$$

$$+\left(1 - {b_{c+}}^2\right)\left(\langle c1,\vec{k}'|U(r)|v1,\vec{k}\rangle + \langle v1,\vec{k}'|U(r)|c1,\vec{k}\rangle\right) + (1 - b_{c+})^2\langle v1,\vec{k}|U(r)|v1,\vec{k}\rangle]$$

$$(B.11)$$

Using Eq. B.10a and B.10b,

$$\langle c+,\vec{k}'|U(r)|c+,\vec{k}\rangle$$

$$= \frac{\widehat{U}(q)}{4\left(1 + {b_{c+}}^2\right)}\left[\left(1 + e^{-i\theta}\right)^2\left(1 + {b_{c+}}^2\right) + \left(1 - e^{-i\theta}\right)^2\left(1 - {b_{c+}}^2\right)\right] \quad (B.12)$$

Similarly, for inter-band scattering:

$$\left\langle c-,\vec{k}'\left|U(r)\right|c+,\vec{k}\right\rangle = \frac{\widehat{U}(q)}{2\sqrt{\left(1+{b_{c-}}^2\right)\left(1+{b_{c+}}^2\right)}}\left(1-e^{-2i\theta}\right) \qquad (B.13)$$

This leads directly to Eq. 3.10a and 3.10b in the Chapter 3.

For impurity induced Rashba interaction $R_{imp}(r)$, scattering matrix elements such as $\left\langle c1,\vec{k}'\middle|R_{imp}(r)\middle|c1,\vec{k}\right\rangle$ can be calculated as follows,

$$\left\langle c1,\vec{k}'\middle|R_{imp}(r)\middle|c1,\vec{k}\right\rangle$$

$$= \frac{1}{4}\left\langle \begin{pmatrix}1 & e^{-i\theta_{\vec{k}'}} & -ie^{-i\theta_{\vec{k}'}} & -ie^{-2i\theta_{\vec{k}'}}\end{pmatrix} e^{-i\vec{k}'\cdot\vec{r}} \middle\| \begin{bmatrix}0 & 0 & 0 & 0\\ 0 & 0 & -iR_{imp}(r) & 0\\ 0 & iR_{imp}(r) & 0 & 0\\ 0 & 0 & 0 & 0\end{bmatrix} \middle\| \begin{pmatrix}1\\ e^{i\theta_{\vec{k}}}\\ ie^{i\theta_{\vec{k}}}\\ ie^{2i\theta_{\vec{k}}}\end{pmatrix} e^{i\vec{k}\cdot\vec{r}} \right\rangle$$

$$= \frac{1}{2}\hat{R}_{imp}(q)e^{-i\theta}$$

$$(B.14)$$

Consequently,

$$\left\langle c1,\vec{k}'\middle|R_{imp}(r)\middle|c1,\vec{k}\right\rangle = \left\langle v1,\vec{k}'\middle|R_{imp}(r)\middle|v1,\vec{k}\right\rangle = \frac{1}{2}\hat{R}_{imp}(q)e^{-i\theta} \qquad (B.15a)$$

$$\left\langle v1,\vec{k}'\middle|R_{imp}(r)\middle|c1,k\right\rangle = \left\langle c1,\vec{k}'\middle|R_{imp}(r)\middle|v1,k\right\rangle = -\frac{1}{2}\hat{R}_{imp}(q)e^{-i\theta} \qquad (B.15b)$$

Similarly, $\left\langle c+,\vec{k}'\middle|R_{imp}(r)\middle|c+,\vec{k}\right\rangle$ can be related to equation Eq. B.15 by

$$\left\langle c+,\vec{k}'\middle|R_{imp}(r)\middle|c+,\vec{k}\right\rangle$$

$$= \frac{1}{2\left(1+{b_{c+}}^2\right)}\left\langle (1+b_{c+})\langle c1,k'| + (1-b_{c+})\langle v1,k'| \middle| R_{imp}(r) \middle| (1+b_{c+})|c1,k\rangle + (1-b_{c+})|v1,k\rangle \right\rangle$$

$$= \frac{{b_{c+}}^2}{1+{b_{c+}}^2}\hat{R}_{imp}(q)e^{-i\theta}$$

$$(B.16)$$

For $\left\langle c-,\vec{k}'\middle|R_{imp}(r)\middle|c+,\vec{k}\right\rangle$ one obtains,

$$\left\langle c-,\vec{k}'\middle|R_{imp}(r)\middle|c+,\vec{k}\right\rangle$$

$$= \frac{1}{2\sqrt{\left(1+{b_{c-}}^2\right)\left(1+{b_{c+}}^2\right)}}\left\langle (1+b_{c-})\langle c2,k'| + (1-b_{c-})\langle v2,k'| \middle| R_{imp}(r) \middle| (1+b_{c+})|c1,k\rangle + (1-b_{c+})|v1,k\rangle \right\rangle$$

$$= 0$$

$$(B.17)$$

Hence the Rashba scattering cross-sections in Eq. 3.14a and 3.14b of the main text are obtained.

C Consideration of the optical theorem

Calculations of potential and Rashba scattering cross-sections are to lowest order Born approximation. It is useful to explore intra-band scattering (c+ to c+) on the basis of the optical theorem,

$$\sigma = \sqrt{\frac{8\pi}{k}} Im[f(0)] \qquad (C.1)$$

where $f(\theta)$ is the true scattering amplitude and σ is the total scattering cross section. In first order Born approximation, the forward scattering amplitude, $f_B(0)$, is real. However, σ may be calculated from the differential scattering cross section as presented in the Chapter 3. $Im[f(0)]$ can then be obtained. We may check the accuracy of of the Born approximation by calculating $Im[f(0)]/f_B(0)$.

$Im[f(0)]/f_B(0)$ for the intra band scattering processes is tabulated in Tables C.1 and C.2 for different Fermi energies and impurity distances.

	$E_F = 25meV$	$E_F = 50meV$	$E_F = 100meV$	$E_F = 200meV$
$z_0 = 2.5nm$	0.0722	0.0361	0.0317	0.0235
$z_0 = 5nm$	0.0723	0.0318	0.0235	0.0135
$z_0 = 10nm$	0.0635	0.0469	0.0290	0.0159

Table. C.1.$Im[f(0)]/f_B(0)$ for intra-band potential scattering.

	$E_F = 25meV$	$E_F = 50meV$	$E_F = 100meV$	$E_F = 200meV$
$z_0 = 2.5nm$	1.4265×10^{-6}	2.2883×10^{-6}	3.0960×10^{-6}	3.3557×10^{-6}
$z_0 = 5nm$	1.1455×10^{-6}	1.5480×10^{-6}	1.6779×10^{-6}	1.6313×10^{-6}
$z_0 = 10nm$	7.7519×10^{-7}	8.4034×10^{-7}	8.1301×10^{-7}	8.3333×10^{-7}

Table. C.2. $Im[f(0)]/f_B(0)$ for intra-band Rashba scattering.

$Im[f(0)]/f_B(0)$ is smaller than 0.1 for potential scattering and smaller than 10^{-5} for Rashba scattering, which serves as a sanity check of our calculation in Chapter 3.